DISS. ETH No. 26702

ROOM-TEMPERATURE SINTERING OF NANOVATERITE WITH WATER

A thesis submitted to attain the degree of
DOCTOR OF SCIENCES of ETH ZURICH
(Dr. Sc. ETH Zurich)

Presented by
MATTHIAS HAUG

MSc ETH Materials
born on 22. January 1990
citizen of Weiningen ZH

Accepted on the recommendation of

Prof. Dr. André R. Studart, examiner
Prof. Dr. Heli Jantunen, co-examiner
Prof. Dr. Markus Niederberger, co-examiner
Dr. Florian Bouville, co-examiner

2020

_____

"The real way to gain happiness is to give it to others"

Lord Robert Baden-Powell of Gilwell (1857-1941)

Founder and first Chief Scout of the worldwide Boy Scout Movement

Acknowledgments

First of all, I would like to express my deepest gratitude to Prof. Dr. André R. Studart for supervising me, during my time in his research group, the Complex Materials Group at ETH Zurich. I really enjoyed working here, in such an interdisciplinary environment with many interesting topics and people.

Secondly, I would like to thank Dr. Florian Bouville sincerely for his constant support during my entire time as a PhD Student. Even though, he became a lecturer at Imperial College and left the group, he kept supporting me. In every discussion we had, he gave feedback and inputs, and if I did not know what to do, he already had at least two other strategies in mind how to solve the problem. You really have taught me a lot!

I am also thankful to Prof. Dr. Heli Jantunen from the University of Oulu in Finland and to Prof. Dr. Markus Niederberger from ETH Zurich. I am honored to have a pioneer on cold sintering and an expert on ceramics as my co-examiners.

I had the chance to work with different researchers from other universities, who helped me a lot with my projects. I wish to thank Prof. Dr. Denis Gebauer, Cristina Ruiz-Agudo and Dr. Jonathan Avaro from the University of Konstanz and Hannover as well as Prof. Dr. Eric Maire, Dr. Jérome Adrien and Dr. Anne Bonnin from the Université de Lyon and from the Paul Scherrer Institute for their help and collaboration.

I had the honor to work with three students, who were all very talented and contributed a great deal to one of my projects. I want to thank Sophia Ganzeboom, Samuel Montibeller and Vanessa Barreiro Lomba for their work in the lab.

A big thank you goes also to all the current and former members of the Complex Materials Group. I am very proud that still know all former members in person from my time when I did my Bachelor Thesis in this group with Tobias Niebel. The current members are Lorenzo Barbera, Fabio Bargardi, Marco Binelli, Rani Boons, Julia Carpenter, Fergal Coulter, Gilberto De Freitas Siqueira, Ahmet Demirörs, Alessandro Dutto, Rebecca Faggion Albers, Christian Furrer, Silvan Gantenbein, Raphael Heeb, Etienne Jeoffroy, Nicole Kleger, Isabelle Lendvai, Rafael Libanori, Tommaso Magrini, Iacopo Mattich, Stefano Menasce, Alessandro Ofner, Erik Poloni, Ahmad Rafsanjani, Manuel Schaffner, Elena Tervoort-Gorokhova and Wilhelm Woigk. The former members are Randall Erb, Jonathan Sander, Philipp Chen, Tobias Niebel, Jonas Zürcher, Davide Carnelli, Hortense Le Ferrande, Gisela Angst, Zuzana Tomasikova, Marianne Sommer-Wink, Eve Loiseau, Dimitri Kokkinis, Lauriane Alison, Clara Minas-Payamyar, David Moore,

_____

Summary

Cold sintering is a newly developed densification method in which the porosity of a ceramic material is reduced under pressure and mild temperatures (< 200 °C) in the presence of a liquid phase. This contrasts with the traditional sintering process, where densification is achieved by heating the material to temperatures well above 1000 °C to enhance the mobility and diffusivity of ions and atoms. Because a large amount of energy is needed to reach such high temperatures, extensive research has been dedicated to reducing the sintering temperature and therefore the energy consumption in the ceramics industry. Cold sintering could reduce significantly the energy consumed during the sintering process, resulting in a more sustainable manufacturing route. In this thesis, we investigated cold sintering at room temperature of vaterite, a metastable phase of calcium carbonate, to shed light on possible mechanisms underlying this new sintering approach. We chose to analyze the process at multiple length scales. On a global scale, we first evaluated the influence of processing parameters and crystal structure on the overall densification of vaterite nanopowders. We then applied our newly found knowledge to two other materials. On the one hand, zinc oxide was utilized because it can be produced with a microstructure similar to vaterite. On the other hand, hydroxyapatite was tested for its ability to form crystals in an aqueous medium at room temperature. Finally, we investigated the process on a local scale to study the origin of the densification behavior by directly observing the collective behavior of particles while the external pressure was applied.

The study on cold sintering of calcium carbonates at the global scale revealed that only the metastable vaterite phase shows a pronounced densification behavior when pressed with water. Calcite and amorphous calcium carbonate, compounds with respectively lower and higher aqueous solubility compared to vaterite, exhibit some densification but do not lead to a cohesive material after uniaxial pressing. By changing the pH of the aqueous phase, the solubility of calcium carbonates can change by more than 6 orders of magnitude, but this approach did not show any effect on its densification behavior. This suggests that the dissolution-diffusion-precipitation mechanism commonly proposed to explain cold sintering might not be responsible for the densification of vaterite at room temperature. Compaction experiments also showed that the temperature has a minor influence on the kinetics of the process but does not affect the final density. By contrast, the applied pressure was found to be the most important processing parameter controlling the final relative density of the powder compact. By applying analytical models to the sintering process, we infer that the observed densification phenomenon may result from the irreversible, inelastic deformation of the agglomerates triggered either by dislocation movements or by water-facilitated subcritical crack growth followed by neck formation. The experimental protocol leading to cold sintering

of vaterite does not result in the densification of zinc oxide and hydroxyapatite. Indeed, both materials did not show any significant porosity reduction despite the similar hierarchical structure or the ability to crystallize at room temperature in water. Thus, our experimental results suggest that cold sintering at room temperature is closely related to the crystal structure and the intrinsic properties of the nanovaterite particles.

On the local scale, we investigated the densification process by performing stress relaxation experiments while imaging the material via *in situ* X-Ray tomography in a synchrotron light source facility. When the relaxation experiment was conducted with water, the local strain developed within the powder compact was large and oriented in the direction of the compressive stress, leading to an overall densification of the specimen. Under dry conditions, the motion of the particles was predominantly lateral and therefore did not contribute as efficiently to the densification of the compact. These results clearly indicated the crucial effect of water on the cold sintering of nanovaterite powder. Complementary micro- and nano-indentation experiments on an 85%-dense vaterite sample revealed that the creep response of the compact is dominated by processes that take place at the nanoscale.

Overall, this thesis shows that the cold sintering of calcium carbonate at room temperature is specific to the vaterite phase, which is able to densify through the deformation of agglomerates possibly driven by plasticity and/or fracture followed by necking phenomena at the length scale of the nanoparticles.

Zusammenfassung

Durch Druck und mit der Hilfe einer flüssigen Phase ermöglicht der neu entwickelte Kalt-Sinter Prozess die Verdichtung von keramischen Materialen bei deutlich tieferen Temperaturen (< 200 °C) als herkömmlich. Bei traditionellem Sintern geschieht die Verdichtung von keramischen Materialen bei Temperaturen über 1000 °C, damit die Mobilität der Ionen und Atome durch diffusive Prozesse hoch ist. Das Erzeugen der hohen Temperatur braucht sehr viel Energie, weshalb schon lange geforscht wird, wie die Temperaturen und damit der Energieverbrauch der Keramikindustrie gesenkt werden kann. Das Kalt-Sintern ist ein vielversprechender Prozess, um den Energieverbrauch deutlich zu verringern, was zu einer nachhaltigeren Produktion von keramischen Materialien führen kann. In dieser Dissertation haben wir das Kalt-Sintern von Vaterit, einer metastabilen Phase von Kalziumkarbonat, untersucht, um die möglichen Mechanismen hinter dem Kalt-Sintern zu verstehen. Wir haben uns entschieden, diesen neuen Prozess auf mehreren Ebenen zu analysieren. Auf einer globalen Ebene haben wir den Einfluss der Prozessparameter und der Kristallstruktur auf den Verdichtungsprozess untersucht. Anschliessend versuchten wir das neue Wissen auf zwei andere Materialien anzuwenden: Zum einen auf Zinkoxid, da diese Partikel eine sehr ähnliche Morphologie wie die Vaterit Partikel aufweisen. Zum anderen auf Hydroxylapatit Partikel, weil sich dessen Kristalle direkt in einem wässerigen Medium bei Raumtemperatur bilden lassen. Auf einer lokalen Ebene haben wir das kollektive Verhalten der Partikel beobachtet während sie den Kalt-Sinter Prozess durchlaufen.

Unsere Untersuchungen auf der globalen Ebene haben gezeigt, dass sich nur die metastabile Vaterit Phase stark verdichten lässt und auch nur, wenn diese mit Wasser gepresst wird. Zwei andere Phasen von Kalziumcarbonat, Kalzit und amorphes Kalziumkarbonat, welche eine geringere, beziehungsweise höhere Löslichkeit in Wasser aufweisen als Vaterit, können ebenfalls leicht verdichtet werden, ergeben aber keine gesinterten, kohäsiven Proben unter uniaxialem Druck, selbst wenn die Wasserlöslichkeit durch eine Änderung des pH-Werts über sechs Grössenordnungen variiert wird. Dies lässt darauf schliessen, dass der üblicherweise vorgeschlagene Mechanismus, Auflösung-Diffusion-Ausfällung, im Falle der Vaterit Verdichtung bei Raumtemperatur nicht zum Tragen kommt. Zwei weitere Prozessparameter, die untersucht wurden, waren die Temperatur und der Druck. Experimente bei verschiedenen Temperaturen haben einen kleinen Effekt auf die Kinetik des Verdichtungsprozesses gezeigt, ohne aber die Enddichte zu beeinflussen. In der Tat ist der angelegte Druck der wichtigste Parameter, um die Dichte der Probe einzustellen. Wir haben analytische Modelle aus dem Bereich des traditionellen Sinterns auf diesen neuen Prozess angewendet und konnten daraus schliessen, dass das beobachtete Phänomen seinen Ursprung bei der irreversiblen,

inelastischen Verformung der Agglomerate hat. Diese Deformationen könnten durch Versetzungen ausgelöst werden oder durch unterkritisches Risswachstum, welches durch das Wasser ermöglicht wird.

Dasselbe experimentelle Protokoll, welches bei Vaterit zu Kalt-Sintern geführt hat, zeigte leider keine Verdichtung bei Zinkoxid oder bei Hydroxylapatit. Die Porosität in beiden Materialien konnte nicht reduziert werden, obwohl diese eine ähnliche hierarchische Partikelstruktur aufweisen und Hydroxylapatit sogar Kristalle in Wasser ausbilden kann. Auf Grund von diesen Experimenten können wir darauf schliessen, dass das Kalt-Sintern bei Raumtemperatur eng mit der Kristallstruktur und den intrinsischen Eigenschaften von Vaterit verbunden ist.

Auf der lokalen Ebene haben wir den Verdichtungsprozess genauer untersucht, indem wir die Partikel während einem Druck-Relaxationsexperiment mit einem Röntgentomograph, welcher mit Synchrotron Strahlung betrieben wurde, abgebildet haben. Wenn das Relaxationsexperiment mit Wasser durchgeführt wurde, waren die lokalen Deformationen gross und zeigten in dieselbe Richtung wie die aufgewendete Kraft, was zu einer Verdichtung vom Pulver führte. Unter denselben Bedingungen, aber ohne Wasser, konnten wir eine vorwiegend lokale Deformation lateral zur Kraftrichtung feststellen, welche entsprechend wenig Verdichtung zur Folge hat. Diese Resultate unterstreichen den ausschlaggebenden Effekt von Wasser auf das Kalt-Sinter Verhalten von Vaterit. Ergänzend zu den Relaxationsexperimenten im Röntgentomograph haben wir Nano- und Micro-Eindruckexperimente auf einer 85% dichten Vaterit Probe durchgeführt. Wir konnten damit zeigen, dass das Kriechverhalten, welches zur Verdichtung der Vaterit Proben führt, von Prozessen auf der Nanoebene dominiert wird.

Zusammenfassend zeigt diese Dissertation, dass der Kalt-Sinter Prozess von Kalziumkarbonat bei Raumtemperatur nur mit der metastabilen Vaterit Phase funktioniert. Der Verdichtungsprozess dieser Phase wird durch die Verformung der Agglomerate bestimmt, vermutlich durch Versetzungen oder durch unterkritisches Risswachstum auf der Nanoebene.

Table of Contents

Chapter 3: Uniaxial Pressing of Zinc Oxide and Hydroxyapatite Powders.............47

Chapter 4: Multiscale-Deformation Processes during Cold Sintering of Nanovaterite Compacts 63

_____

"Leave this world a little better than you found it."

Lord Robert Baden-Powell of Gilwell (1857-1941)

Chapter 1: Introduction

1.1. Traditional Sintering

Sintering is an ancient processing technique. It probably dates back to about 24'000 BC, when people observed the improvement in strength when firing clay and ceramic pottery [1]. While there is no record of the actual discovery, archeologists found clay pots from that period that have already been sintered, but at moderate temperatures. Such clay pots were not able yet to hold liquids like water due to their porosity. They were also still weak and rarely survived the firing process. Examples of such early fired structures are displayed in Figure 1.1a. Over the following 14'000 years, people improved and mastered this technique so that we were ultimately able to produce water-tight containers.
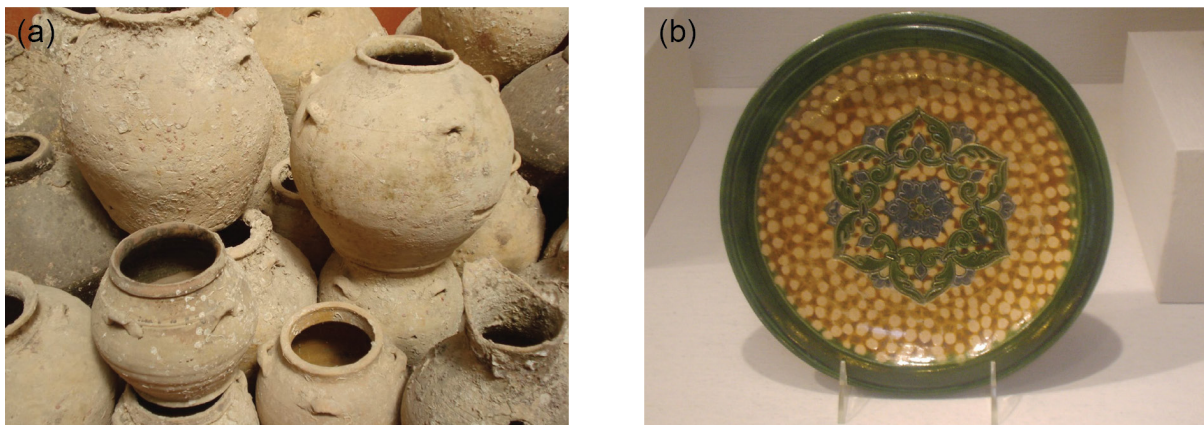
Figure 1.1: *(a) Early sintered pottery, which were neither strong nor were able to hold fluids. (b) Porcelain dish from the Tsing dynasty fabricated at high temperatures around 1300 °C. The images are taken from [1].*

As oven technology developed, the temperature reached during sintering increased and ultimately allowed for a significant improvement in strength, reduction in porosity and made the process available for different materials. By the year 900 AD, temperatures up to 1300 °C could be achieved, which enabled the sintering of porcelain in China (Figure 1.1b) [1].

Today, sintering is simply defined as the process by which a particle-based compact is transformed into a solid material without melting. As such, the fabrication of solid materials through sintering is therefore an essential processing step for all materials with a high melting temperature (T_m) such as ceramics or refractory metals. Sintering is typically activated by increasing the temperature to 0.6-0.8 T_m. At this elevated temperature, a loose assembly of

particles is densified into a solid part through the motion of particles closer together, leading to shrinkage and the elimination of pores.

The study of sintering and the underlying processes aim to provide us with better control over the final microstructure but also to lower the temperature at which sintering occurs. To discuss our current understanding of traditional sintering and of the newly developed cold sintering approach, there are several key aspects that need to be introduced. In this chapter, the driving forces and kinetics of traditional sintering are introduced along with today's available strategies to lower the sintering temperature. Then, two geological sintering processes that take place in the earth's upper crust and lead to the formation of dense rocks are introduced and linked to our knowledge of traditional sintering of ceramics. In the last part, the literature for the newly developed cold sintering process is summarized to show that this novel process finds its root in both traditional and natural sintering processes.

1.1.1. Driving Forces for Sintering

Sintering, as any other process controlled by thermodynamics, spontaneously occurs if there is an overall decrease of the total free energy of the system. In a powder compact, intrinsic sources of high free energy are a large surface area, high total surface energy and curvature gradients [2, 3]. The reduction of free surfaces is the main internal driving force for sintering. The reduction of the surface free energy (E_s) from one mol of monodispersed spherical particles into one dense body can be estimated with the following equation:

$$E_s = \frac{3\gamma_{sv}V_M}{R}$$

Equation 1.1

Where

γ_{sv} is the material specific surface energy
V_M is the molar volume and
R is the radius of the particles.

Taking typical values for γ_{sv}=1 J m^{-2}, V_M=25·10^{-6} m^3 mol^{-1} and R=1 μm, the reduction of surface free energy can be estimated to be E_s=75 J mol^{-1} [2]. For a typical ceramic tea mug of 300 g, this would correspond to 100 J. Such free energy is comparable to the energy required to heat up 10 mL of tea from 25 to 27 °C. While this energy does not seems to be very high, it provides a finite driving force for sintering to occur. With this equation, we can also analyze the influence of the particle size on the sintering process. Decreasing the particle radius leads to a direct increase of the energy gained through the sintering process.

The driving force for sintering can be increased substantially by applying external pressure. The driving force in this case can be approximated from the work done on the system (W_p) by [2]:

$$W_p = \sigma_a V_M$$

Where

σ_a is the applied stress and
V_M is the molar volume.

Taking σ_a=30 MPa and V_M=25·10^{-6} m^3 mol^{-1}, the sintering driving force under external pressure is W_p=750 J mol^{-1} [2]. The tenfold higher energy involved through the application of pressure compared to that associated with the particle surface area indicates the important role of external stresses in promoting the sintering process.

It is important to note though that these energetic driving forces can only give insight on whether or not the sintering process will happen. In addition to thermodynamic energy gains, the kinetics of the process plays an equally important role in understanding and controlling sintering.

1.1.2. Kinetics for Sintering

The system reacts to the driving force mentioned above by mass transport within the particles to reach a thermodynamically more favorable state. In ceramics, diffusion of atoms and ions is the predominant pathway for mass transport. Crystalline materials are usually considered as a model for sintering studies, as diffusion is easier to describe in regular lattices compared to amorphous materials. Ionic diffusion in bulk ceramics is enhanced by defects in the crystalline structure, mainly atomic vacancies. Fick's law [4] can mathematically describe such diffusive processes via the quantitative relation [2]:

$$J = -D(T)\frac{\partial C}{\partial x}$$

Where

J is the flux of atoms (or vacancies)
$D(T)$ is the temperature dependent diffusion coefficient and
$\frac{\partial C}{\partial x}$ is the concentration gradient of vacancies.

The temperature dependence of the diffusion coefficient can be described by an Arrhenius law:

$$D(T) = D_0 \exp\left[-\frac{E_A}{RT}\right]$$

Equation 1.4

Where

D_0 is the maximal diffusion coefficient at infinite temperature
E_A is the activation energy for diffusion
R is the universal gas constant
T is the absolute temperature

This relation indicates a very strong dependence of the diffusivity of ions, atoms, and vacancies on temperature. Therefore, the temperature is the most relevant parameter in sintering processes. It is important to note that the diffusion coefficient can change when different diffusion paths are activated. For example, there are different diffusion coefficients for lattice diffusion and grain boundary diffusion.

Fick's law does not only apply to a gradient in concentration. It can also be rewritten to show a similar dependence on a change in chemical potential. The chemical potential changes, for example, with variations in the curvature of surfaces. This leads to a flux of atoms from a convex surface to a concave surface or a flux of vacancies in the opposite direction. With this mechanism, the system is able to reduce its total surface area and thus its free energy.

As mentioned in chapter 1.1.1, a decrease in particle size leads to an increase in the sintering driving force. Kinetic processes are also affected by the particle size. In this case, it is important to consider that the speed of sintering is dictated by the slowest diffusional process. By applying a scaling law, formulated by Herring in 1950 [5], the effect of particle size on sintering time can be expressed as [2]:

$$\frac{\Delta t_2}{\Delta t_1} = \left(\frac{R_2}{R_1}\right)^l$$

Equation 1.5

Where

Δt_i is the time needed for the sintering to happen, typically taking as the time necessary to reach two defined densities,
R_i is the particle radius and
l is an exponent that depends on the sintering mechanism and can vary between 1 and 4 [2, 5].

The different exponents and the corresponding sintering mechanisms are listed in Table 1.1.

The above relation shows that the time for sintering can be reduced from Δt_1 to Δt_2 by decreasing the particle radius from R_1 to R_2. Depending on the slowest mechanism at play, this decrease in time can be reduced more effectively.

Whereas this description allows extracting the main sintering mechanism, the densification of powder compacts happens in several stages, possibly with different diffusion mechanisms involved. After describing why and how sintering works, we will now discuss sintering mechanisms and stages in more detail.

Table 1.1: Different sintering mechanisms and the corresponding exponents [2].

Sintering Mechanism	Exponent (l)
Surface diffusion	4
Lattice diffusion	3
Vapor transport	2
Grain boundary diffusion	4
Plastic flow	1

1.1.3. Sintering Mechanisms and Sintering Stages

In general, six different mechanisms contribute to sintering [2]. They are (1) surface diffusion, (2) lattice diffusion of atoms from the surface, (3) vapor transport, (4) grain boundary diffusion, (5) lattice diffusion of atoms from the grain boundary and (6) plastic flow (Figure 1.2). All of these mechanisms lead to neck growth and strengthening of the material, but not necessarily to shrinkage and densification. Only grain boundary diffusion, lattice diffusion of atoms from the grain boundary and plastic flow are able to drive the centers of the particles closer and thus promote densification. Even though three of these mechanisms do not lead to densification, they still reduce the overall driving force for sintering by lowering the total surface area of the powder compact.

1. Surface diffusion
2. Lattice diffusion (from the surface)
3. Vapor transport
4. Grain boundary diffusion
5. Lattice diffusion (from the grain boundary)
6. Plastic Flow
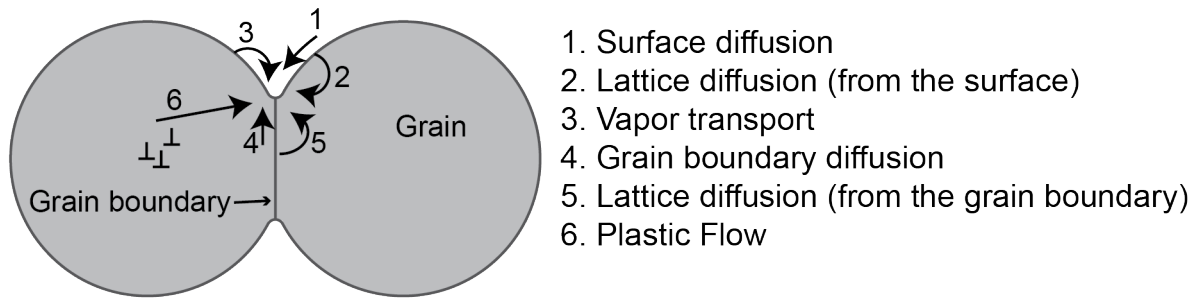
Figure 1.2: *The six distinct mechanisms that can contribute to sintering of crystalline particles. Adapted from [2].*

Ultimately, the sintering process can be divided into three different stages [1, 2], as represented in Figure 1.3. Before the sintering process starts, the particles are loosely packed.
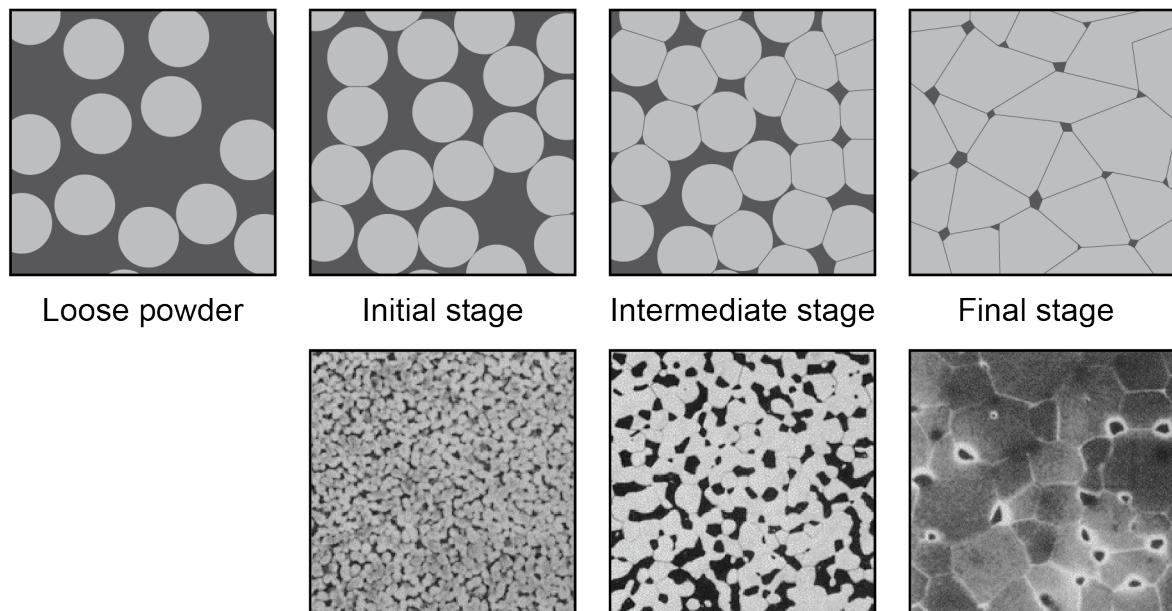
Figure 1.3: *Schematic representation of the sintering stages and matching examples of real microstructures from representative particle compacts [2].*

In the initial stage, the driving force for sintering is the largest and the necks between the particles form and grow rapidly by diffusion, vapor transport, plastic flow or viscous flow. In this stage, only little shrinkage occurs and large differences in surface curvature are removed, which rapidly lowers the driving force for sintering. In the intermediate stage, very high shrinkage is observed and the sample reaches about 90% of the theoretical density, leaving about 10% of porosity. The pores still form a continuous network and they reach an equilibrium shape dictated by the gas pressure and the interfacial tension between the gas and the material surface. As soon as some pores become isolated, typically at the corners of the grains, the final stage of sintering begins. In this final stage, densification occurs predominately by the

dissolution of the gas phase in the ceramic lattice and the diffusion of the dissolved gas away from the pores. However, this is only possible if the gas is soluble in the ceramic material. With these processes, the initial compact can be transformed into fully dense structures.

Different sintering methods have been developed to reduce the temperature, increase the speed or limit unwanted sintering features, such as grain growth. Two of these methods, pressure-assisted sintering and liquid-phase sintering, are discussed in the following chapters as they share some similarities with cold sintering.

1.1.4. Pressure-Assisted Sintering

As discussed in chapter 1.1.1., applying pressure has a tremendous effect on the driving force of the sintering process. Furthermore, the applied pressure significantly enhances the densifying sintering mechanisms while not affecting the non-densifying ones. Therefore, applied stresses lead to a change in sintering mechanisms from lattice or grain boundary diffusion to particle deformation and rearrangement. Particle deformation may occur through plastic deformation mediated by dislocation movement. Whereas particle rearrangement is difficult to analyze, there are methods to quantify the contribution of plasticity to particle deformation.

Particle deformation is only possible because of stress intensification at the grain boundaries and particle contact points. The contact area between two particles is small and therefore the applied macroscopic stress is amplified at that point. This amplification can be expressed in models with a stress intensification factor.

Under these assumptions, a mathematical description of the sintering process with external pressure is possible by adjusting established equations from the Nabarro/Herring creep model. In this model, the applied stress will be relieved in the solid by self-diffusion. The atoms diffuse from the particle contact point, which is under compressive stress and therefore has a higher chemical potential, to the free surface, which is under tension and has a lower chemical potential. Taking these assumptions and applying them to a pressure-assisted sintering model system of two spheres leads to the following equation [2]:

$$\frac{1}{\rho}\frac{d\rho}{dt} = \frac{HD(T)}{kT}\frac{1}{G^m}(\varphi\sigma_a)^f \qquad\qquad \textit{Equation 1.6}$$

Where

ρ is the density of the compact,

$\frac{d\rho}{dt}$ is the densification rate,

H is a numerical constant,

_____

$D(T)$ is the temperature-dependent diffusion coefficient,

k is the Boltzmann constant,

T is the absolute temperature,

G is the grain size,

m is the grain size exponent,

φ is the stress intensification factor,

σ_a is the applied pressure and

f is the stress exponent.

Different grain size exponents m and stress exponents f can be obtained depending on the slowest mechanisms at play. The possible combinations of the exponents and the corresponding mechanisms are summarized in Table 1.2.

While the driving force of sintering can be increased by the applied pressure, the kinetics of the process can be modified with liquid-phase sintering to result in faster densification.

Table 1.2: Different sintering mechanisms and their corresponding grain size exponents and stress exponents [2].

Mechanism	Grain size exponent (m)	Stress exponent (f)
Lattice diffusion	2	1
Grain boundary diffusion	3	1
Plastic deformation	0	≥ 3
Viscous flow	0	1
Grain boundary sliding	1	$1-2$

1.1.5. Liquid-Phase Sintering

In chapter 1.1.2, the diffusion coefficient of atoms was introduced and directly linked with the sintering kinetics. However, the diffusion of atoms in solids can be 100 to 1000 times slower than in liquids. By introducing into the system a secondary phase that has a melting temperature lower than the sintering temperature and wets the surface of the particles, this faster diffusion process can be used to increase the sintering speed [1].

Additionally, the liquid phase during sintering can also reduce the friction between the particles and therefore increase particle rearrangement, which leads to better particle packing, lower porosity and increased sintering performance [2].

1.2. *Densification of Rocks in Geological Formations*

While ceramics are a human invention that is now widely industrially present, other forms of inorganic materials with comparable chemistries can be made in nature by living organisms or exist in the form of rocks generated through long geological processes. The shell of mollusks, for example, contains 95% calcium carbonate and only 5% organic material [6], whereas bone in the human body contains up to 50% calcium phosphate and 50% organic material such as proteins [7]. As far as geological formations are concerned, almost the entire earth's upper crust is made from dense inorganic materials with chemistries similar to those of man-made ceramics [8]. The minerals found here are mostly silicon dioxide, iron oxides or calcium carbonates. The density of such natural minerals depends on the depth at which they were found: the higher the depth, the lower the porosity (Figure 1.4) [9]. Since the pressure in the Earth's upper crust increases with the depth, the low porosity of deep geological formations such as carbonates has been attributed to densification mechanisms under pressure. These observations drove geologists to study the possible phenomena leading to the densification of natural minerals under mild temperatures. One of the most studied densification mechanisms for carbonates involves the dual action of pressure and water close to room temperature, which is known as Pressure Solution Creep.
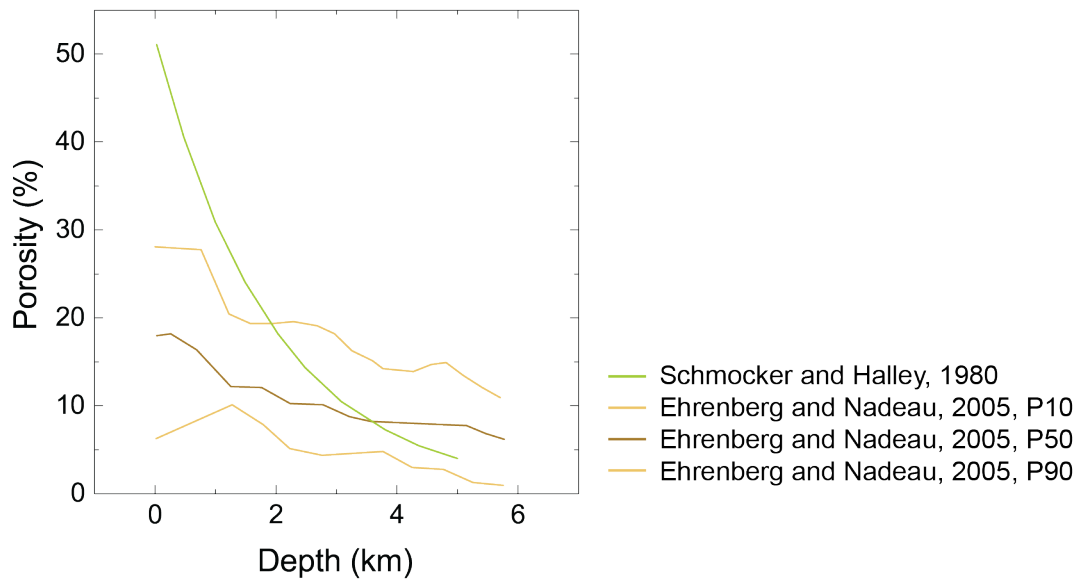
Figure 1.4: *Porosity in carbonates as a function of the depth from different environments. Adapted from [9-11].*

1.2.1. Pressure Solution Creep

One major mechanism responsible for the increase in relative density of geological formations under pressure is called pressure solution creep (PSC) [8]. Geologists have studied this process extensively and found evidence of PSC from near the surface down to 10-15 km. A schematic representation of PSC along with experimental evidence can be found in Figure 1.5. This densification mechanism can be described as a three-step process:

- The solid material is dissolved in the presence of a liquid medium and under non-hydrostatic stress. The material dissolves preferentially at the contact points between grains/particles, where the largest normal stresses are developed (Figure 1.5, red arrows).
- The dissolved ions diffuse through the liquid film present on the surface of the particles away from this highly stressed zone (Figure 1.5, blue arrows).
- Finally, the material is deposited again in the zone of the smallest normal stress (Figure 1.5 light brown zones).

Following the mechanisms described above, the PSC process leads to the densification of the minerals in the earth's upper crust. The driving force for this process is the difference in the chemical potential of the solid between the dissolution zone and the deposition zone. This difference leads to mass transport through the film and ultimately the densification of the material.

_____
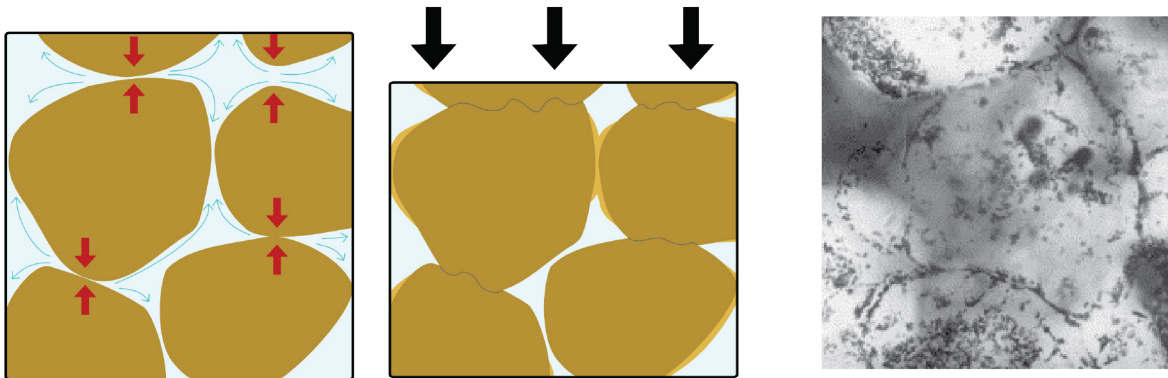
Figure 1.5: Representation of pressure solution creep in the earth upper crust. *The red arrows indicate dissolution zones. The blue arrows describe the diffusion pathways of the dissolved ions. The light brown color in the middle representation indicates the newly deposited solid material. A light microscopy image from NaClO₃ pressed at 5 MPa at room temperature shows the densely packed grain. The grain size is around 200 μm. Adapted from [12].*

Researchers have developed experimental setups to investigate PSC under laboratory conditions and thus systematically analyze the influence of parameters such as pressure, temperature or pore fluid composition on the densification process. A typical setup is displayed in Figure 1.6. Usually, SiO_2 or $CaCO_3$ rocks from a natural source are filled into the testing setup. The pores between the particles can then be filled with a pore fluid, which is typically water, saturated with the ions of the mineral. After the experiment is prepared, the displacement of the piston is measured under a constant load over different periods of time. The typical timescale for such PSC experiments is a few weeks up to a few months under relatively low stresses below 50 MPa.

As described above, there are three successive steps involved: dissolution, diffusion, and precipitation. The slowest of these three steps therefore determines the overall speed of the PSC process. The determining step can change even for a single material. For example, the pressure solution creep rate for quartz (SiO_2) is limited by dissolution at temperatures below 150 °C but is limited by diffusion at higher temperatures [8]. In general, soluble salts, such as sodium chloride (NaCl) are densified under pressure through diffusion-limited processes. For special cases involving the presence of certain impurities on the surface of calcite or quartz, the precipitation step limits the rate of the densification process. For these three cases, the pressure solution creep rate can be estimated from thermodynamic equilibrium constants. The general form of the PSC rate equation is [13]:
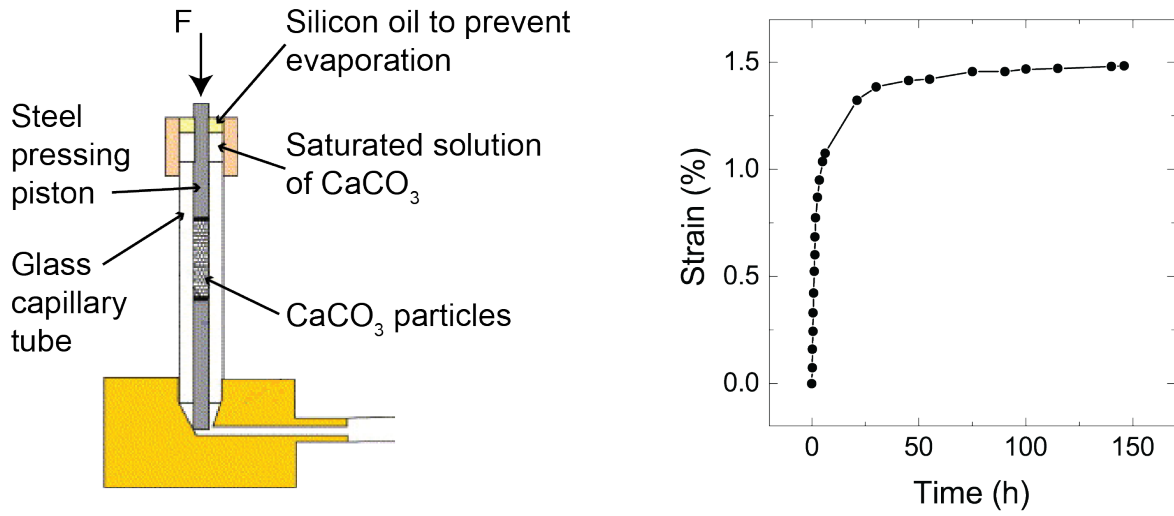
Figure 1.6: *Setup to experimentally measure pressure solution creep (left) and the typical results obtained (right). Adapted from [14].*

$$\dot{\varepsilon} = \alpha \frac{\left[\exp\left(\dfrac{\varphi(\phi_0, \varepsilon_v)\sigma_a V_M}{RT}\right) - 1\right]}{G^\beta} f(\phi_0, \varepsilon_v)$$ *Equation 1.7*

Where

$\dot{\varepsilon}$ is the volumetric strain rate,

α is a constant specific to the limiting process,

$\varphi(\phi_0, \varepsilon_v)$ is a stress intensification factor,

ϕ_0 is the initial porosity,

ε_v is the volumetric strain,

σ_a is the experimentally applied stress,

V_M is the molar volume of the material,

R is the universal gas constant,

T is the absolute temperature,

G is the grain size,

β is the grain size exponent which varies with the rate-limiting process and

$f(\phi_0, \varepsilon_v)$ is the porosity function, which accounts for the evolving grain structure and is specific to the rate-limiting process.

If the process is limited by the dissolution of the solid phase, the PSC rate can be written as

_____

$$\dot{\varepsilon}_s = k_s(T) \frac{\left[\exp\left(\frac{\varphi(\phi_0, \varepsilon_v)\sigma_a V_M}{RT}\right) - 1\right]}{G} f_s(\phi_0, \varepsilon_v)$$

Equation 1.8

Where

$k_s(T)$ is the temperature-dependent dissolution rate coefficient and
$f_s(\phi_0, \varepsilon_v)$ is the porosity function for the dissolution-limited case.

Exact formulas for $\varphi(\phi_0, \varepsilon_v)$ and $f_s(\phi_0, \varepsilon_v)$ can be found elsewhere [13].

If the process is limited by the diffusion of ions, the formula can be written as

$$\dot{\varepsilon}_d = D(T)C(T)S \frac{\left[\exp\left(\frac{\varphi(\phi_0, \varepsilon_v)\sigma_a V_M}{RT}\right) - 1\right]}{G^3} f_d(\phi_0, \varepsilon_v)$$

Equation 1.9

Where

$D(T)$ is the temperature-dependent diffusion coefficient,
$C(T)$ is the temperature-dependent solubility of the material,
S is the average thickness of the fluid phase at the grain boundary and
$f_d(\phi_0, \varepsilon_v)$ is the porosity function for the diffusion-limited case.

Exact formulas for $\varphi(\phi_0, \varepsilon_v)$ and $f_d(\phi_0, \varepsilon_v)$ can be found elsewhere [13].

If the process is limited by the precipitation step, the formula can be written as

$$\dot{\varepsilon}_p = k_p(T) \frac{\left[\exp\left(\frac{\varphi(\phi_0, \varepsilon_v)\sigma_a V_M}{RT}\right) - 1\right]}{G} f_p(\phi_0, \varepsilon_v)$$

Equation 1.10

Where

$k_p(T)$ is the temperature-dependent precipitation rate coefficient and
$f_p(\phi_0, \varepsilon_v)$ is the porosity function for the precipitation-limited case.

Exact formulas for $\varphi(\phi_0, \varepsilon_v)$ and $f_p(\phi_0, \varepsilon_v)$ can be found elsewhere [13].

These analytical models allow for the identification of the relevant mechanisms controlling the deformation rate of materials that densify through the PSC process. As such, they form the theoretical basis that will be used later in the thesis to interpret the experimental results obtained for the different inorganic materials investigated in this work.

1.2.2. Time-Dependent Brittle Creep

Time-dependent brittle creep is another deformation mechanism that can be responsible for the densification of the earth's upper crust. Brzesowsky et al. [15] investigated the creep of SiO_2 in laboratory conditions. By performing experiments on dry and wet sand under pressures up to 30 MPa, these authors have found that the sand particles show significant cracking after the experiment. Acoustic emission data was utilized to record the cracking events of the particles in situ. They hypothesized that the mechanism by which the sand particles crack under such low stresses is similar to subcritical crack growth. Subcritical crack growth is a known mechanism occurring in ceramics, in which a crack can propagate at lower stress intensity factors in the presence of water compared to a dry environment [16]. This time-dependent phenomenon is typically characterized by measuring the speed at which fracture occurs in the material as a function of the applied stress intensity factor. Empirical observations have shown that the velocity of the crack follows a power-law dependence on the applied stress intensity factor, which is characterized by the exponent n. Applying this experimental model to the sand experiments, the measured volumetric strain rate under the applied stress could be correlated with the subcritical crack growth exponent using the following scaling relation:

$$\dot{\varepsilon} \propto \sigma_a^{n/3} \qquad \qquad Equation\ 1.11$$

Where

$\dot{\varepsilon}$ is the volumetric strain rate,
σ_a is the applied stress and
n is the stress corrosion or subcritical crack growth exponent.

The densification of the sand compacts was eventually found to be reasonably described using subcritical crack growth exponents previously reported for silica. This suggests that subcritical crack growth resulted in failure of the grains, enabling intergranular sliding under pressure. Such interpretation was proposed by the authors to explain the mechanism underlying the densification of SiO_2 compacts in the presence of water.
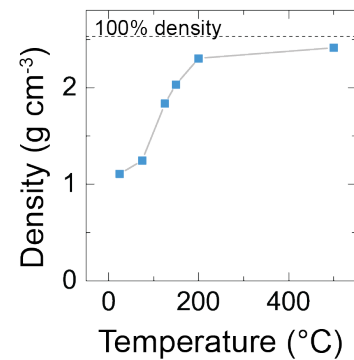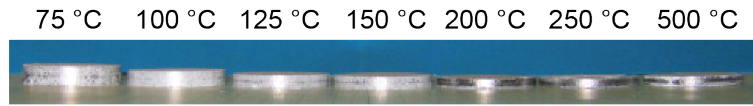
1.3. Cold Sintering

As described in chapter 1.1.2, temperature is the most important parameter when it comes to conventional sintering. High temperatures lead to high mobility of ions and therefore to a fast densification of the material. However, heating a sample to high temperatures requires a lot of energy, which leads to the production of a large amount of CO_2 if fossil fuels are used as an energy source [17, 18]. Unfortunately, the CO_2 levels in the atmosphere have reached an all-time peak and the presence of such greenhouse gases leads to global warming [19]. Therefore, a major societal and technological challenge has been to reduce the amount of CO_2 generated from industrial processes, which ultimately demands a reduction in the amount of energy required in manufacturing technologies. In the ceramics industry, researchers are therefore investigating methods to reduce the sintering temperature needed to densify powder compacts [17]. This has been an important motivation for the development of the relatively new research field of cold sintering.

1.3.1. The Development of Cold Sintering

In the following paragraphs, the most important literature on cold sintering is summarized. The literature is presented in chronological order and is not exhaustive. The focus is set on the materials, the processes and process parameters reported and not on the application of the reported materials. Several research groups have published multiple papers on cold sintering. The review below focuses on the most relevant publications of a given research team. At the end of this subchapter, an effort was made to collect most of the materials and publications to draw conclusions on our current knowledge of cold sintering.

To the best of our knowledge, cold sintering was first mentioned in the year 1979 by Gutmanas and Rabinkin from the Technion-Israel Institute of Technology [20]. They published a paper with the title "Cold Sintering under High Pressure", which reported the densification behavior of many different metals, including steel and several ionic compounds. These authors performed experiments at an applied pressure of 4 GPa and a temperature of 300 K. Excellent cold sintering behavior was manifested in the form of high mechanical properties and a high relative density of 98% for Al, Cu, Nb, Ta, CdTe, and RbI specimens. They attributed this strong densification to plastic flow of the material under the high applied pressures.

(a) Influence of the dwell temperature
at constant pressure - 100 MPa

75 °C   100 °C   125 °C   150 °C   200 °C   250 °C   500 °C

(b) Influence of the mechanical pressure applied
at constant temperature - 150 °C

5 MPa   25 MPa   50 MPa   100 MPa
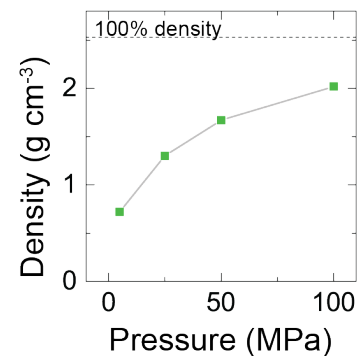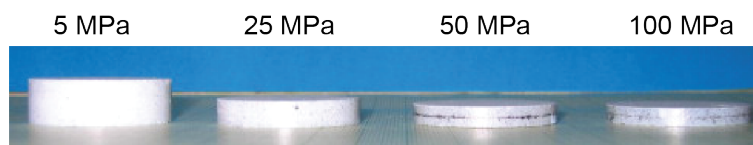
Figure 1.7: Cold sintering of apatite. Influence of (a) the temperature and (b) the pressure on both the sample height and density. Adapted from [21].

In the year 2009, Grossin *et al.* in the group of Prof Drouet from the Université de Toulouse in France [21] reported for the first time the densification of the apatite crystal ($Ca_{10-(x-u)}(PO_4)_{6-x}(HPO_4)_x(OH)_{2-(x-2u)}$) at temperatures substantially lower than the traditional sintering temperatures used for this material. Apatite is a material used for bone tissue engineering, as it has a chemical composition and crystal structure similar to the mineral part of bone. The experiments were carried out in a spark plasma sintering oven (SPS) with nanocrystalline apatite at temperatures below 500 °C (Figure 1.7a) and at pressures up to 100 MPa (Figure 1.7b). At a pressure of 100 MPa, a sintering temperature as low as 200 °C was sufficient to increase the density of the compact to 2.3 g cm^{-3}, while the powder density of non-stoichiometric apatite is 2.53 g cm^{-3}. Although no water was initially added to the powder before pressing, FTIR measurements indicate the presence of a hydrated layer on the nanocrystals. Since these temperatures are too low to provide the thermal energy necessary for atom self-diffusion, the authors suggest that the hydration layer might allow for sufficient ion mobility to densify the powder at such a low temperature.

In 2014, Kähäri *et al.* in the group of Prof Jantunen from the University of Oulu in Finland [22] reported the densification of lithium molybdate (Li_2MoO_4) at room temperature and low applied pressures. A final density of 93% was reached at room temperature under uniaxial pressure of 130 MPa. In this case, deionized water was sprayed on the powder before loading
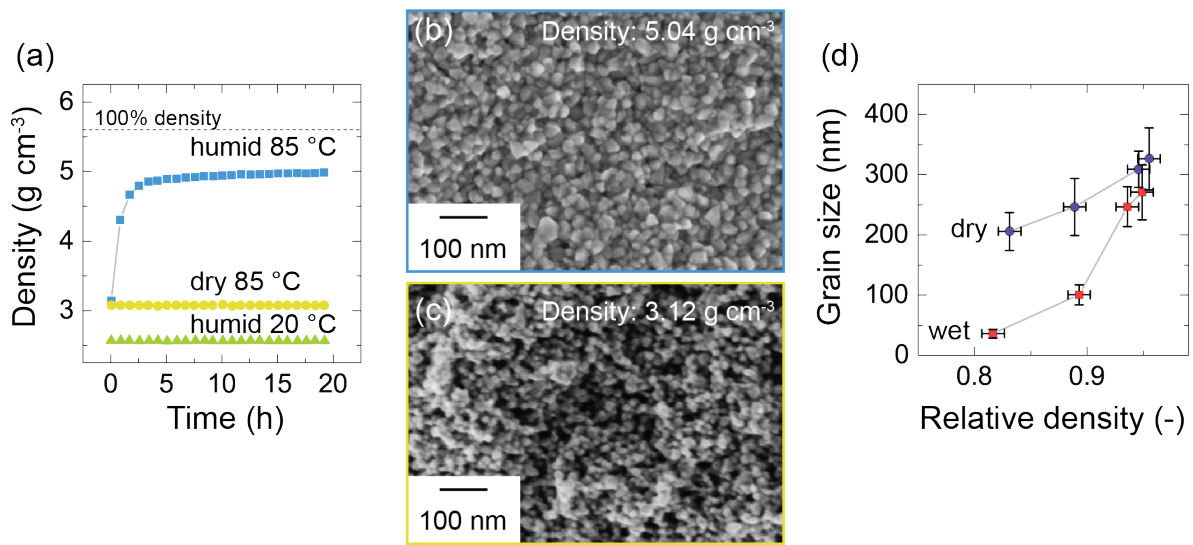
Figure 1.8: Cold sintering of ZnO. *(a) Density as a function of time for ZnO nanoparticles pressed at 50 MPa under different conditions. (b,c) SEM images of the fracture surfaces of ZnO compacts pressed at 85 °C in (b) humid or (c) dry conditions. (d) Grain size as a function of the relative density after pressing in wet and dry conditions. Adapted from [23].*

it into a pressing tool. Compared to apatite, Li_2MoO_4 is highly soluble in water. With an aqueous solubility of up to 440 g L^{-1}, Li_2MoO_4 is even more soluble than sodium chloride (360 g L^{-1}). The cold sintering mechanism is probably due to the high solubility of Li_2MoO_4 in water, which enables the dissolution and thus densification of the sample during pressing. The authors highlight that such low processing temperatures of ceramic materials open the way for the fabrication of new kinds of composites with seamless integration of ceramics and polymers.

Dargatz *et al.* from the group of Prof Guillon from the Forschungszentrum Jülich in Germany [23] published in 2015 a paper on the improved compaction behavior of zinc oxide (ZnO) nanoparticles at 85 °C under a pressure of 50 MPa. ZnO is an n-type semiconductor used in electronics and optoelectronics. Before pressing at 85 °C, the powder was stored at the same temperature in a moist environment at a humidity of 140 g m^{-3}, which corresponds to 85% relative humidity. A final relative density of 86% was reached after pressing (Figure 1.8a). The authors also showed evidence of limited grain growth under these mild conditions compared to the significant grain coarsening typically observed during high-temperature sintering (Figure 1.8d).
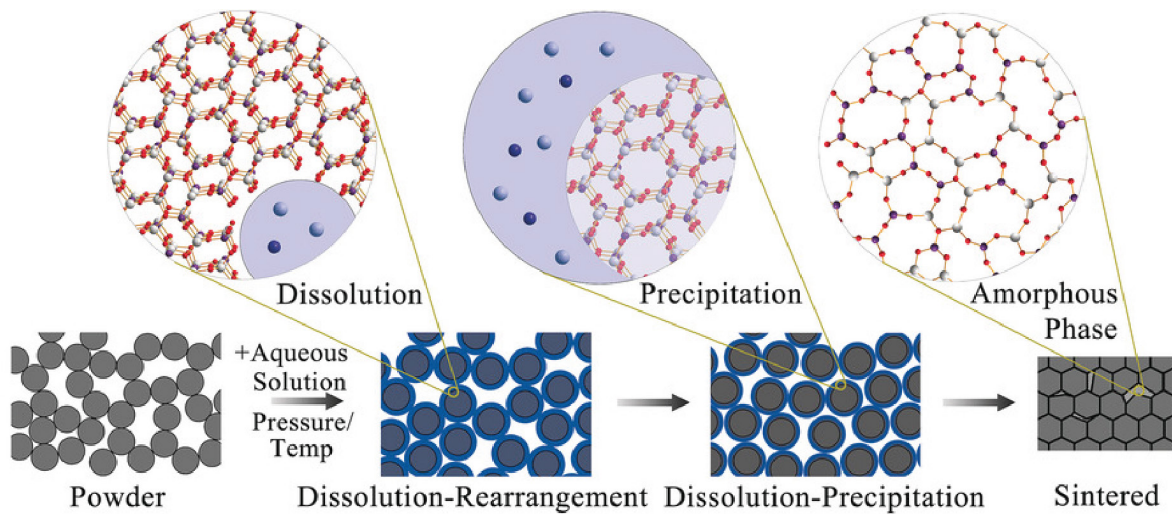
Figure 1.9: *Cold sintering mechanisms proposed by Guo J, Guo H et al. from Prof Randall's group. Reproduced from [24]*

In 2016, Guo J., Guo H. *et al.* from the group of Prof Randall from The Pennsylvania State University in the United States [24] introduced a new term for these ultra-low temperature sintering process: the cold sintering process (CSP). They report the core concept of CSP as follows: densification occurs in the presence of a transient liquid phase and the densification is supposedly mediated by a dissolution-precipitation process (Figure 1.9). The ceramic powder is wetted by the liquid, which causes sharp edges to dissolve and enable the rearrangement of particles. This concept finds its root in the ones presented previously in this chapter, namely the densification under pressure with a liquid phase utilized in traditional ceramic processing and the pressure solution creep process observed in geology. Under pressure, the contact point between two particles becomes highly stressed, leading to an increase in the thermodynamic chemical potential. Ionic species dissolved in the aqueous phase thus diffuse to zones with lower chemical potential. This mass transport mechanism enables the system to minimize its surface free energy, removing the porosity between particles. In a final stage, the transient liquid is removed, possibly leaving an amorphous phase at the grain boundary depending on the species dissolved in the liquid. This amorphous phase can be crystallized in a subsequent annealing step, which is conducted generally at a temperature around 100-200 °C lower than the conventional sintering temperature. In this first study, the authors show pressure-less cold sintering of sodium chloride (NaCl) at room temperature, sintering of alkali molybdates (K_2MoO_4, Na_2MoO_4, Li_2MoO_4) and vanadium oxide (V_2O_5) at 120 °C under a pressure of 570 MPa.

Bouville and Studart from ETH Zurich in Switzerland [25] reported in 2017 on a geologically-inspired process for the room-temperature densification of calcium carbonate. They were inspired by the formation of dense rocks in the earth's upper crust, presented in chapter 1.2.1. The densification of calcium carbonate ($CaCO_3$) was investigated in the pressure range 10-
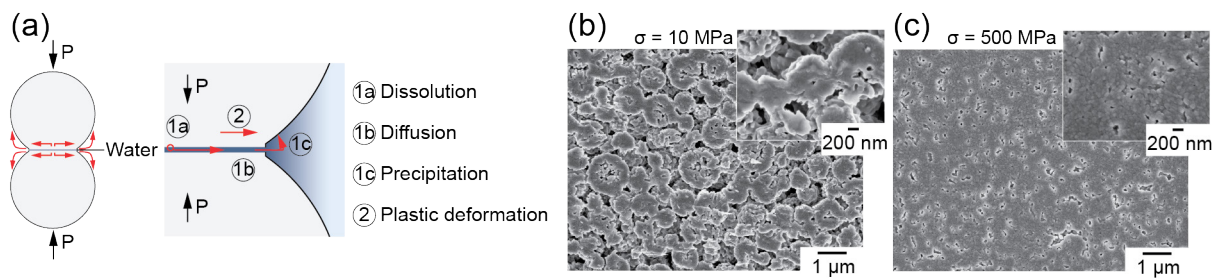
Figure 1.10: Cold sintering of calcium carbonate. *(a) Schematic representation of the possible densification mechanisms. (b,c) SEM micrographs of polished surfaces densified with water at (b) 10 MPa and (c) 500 MPa. Adapted from [25].*

800 MPa, at room temperature and in the presence of water. The final relative density of this material was shown to depend strongly on the applied pressure. The mechanical properties of the final product were 10 times higher than that of concrete. As a possible cold sintering mechanism, the authors referred to the pressure solution creep process found in geology. This is also based on dissolution − diffusion − precipitation steps, similar to the mechanism proposed by Guo J., Guo H. *et al.* Dislocation-mediated plastic deformation within the particles was also discussed as an additional possible densification mechanism (Figure 1.10).

In 2018, Hong *et al.* from the group of Prof Chen from the Zhejiang University in China [26] investigated the densification behavior of NaCl at room temperature under pressure between 50 and 300 MPa in the presence of water. NaCl pressed at 50 MPa with water showed a relative density of 88% while the dry-pressed particle compacts reached 80%. At pressures higher than 150 MPa, the dry-pressed compact achieved even higher relative densities than the one pressed under wet conditions. This is not commonly observed during cold sintering, which suggests that the low hardness of NaCl enables plastic deformation of the particles and is most likely the main mechanism responsible for the densification under high pressure.

Ndayishimiye *et al.* from the group of Prof Goglio from the Université de Bordeaux in France [27] published in 2018 a manuscript on the cold sintering of amorphous silicon dioxide (SiO_2) compacts with water at 300 °C under a pressure of 190 MPa. The authors found that the water layer on the surface of the particles strongly influences the densification behavior. Because the process used to synthesize the silica nanoparticles (60 nm in size) occurs in water, there is naturally a physisorbed water layer on each particle. While heating the sample under pressure, the silica particles start dissolving under the imposed hydrothermal conditions, allowing densification to take place. The final density can be further improved by adding water to the initial sample. The physisorbed water alone is not sufficient to densify the compacts of silica particles.
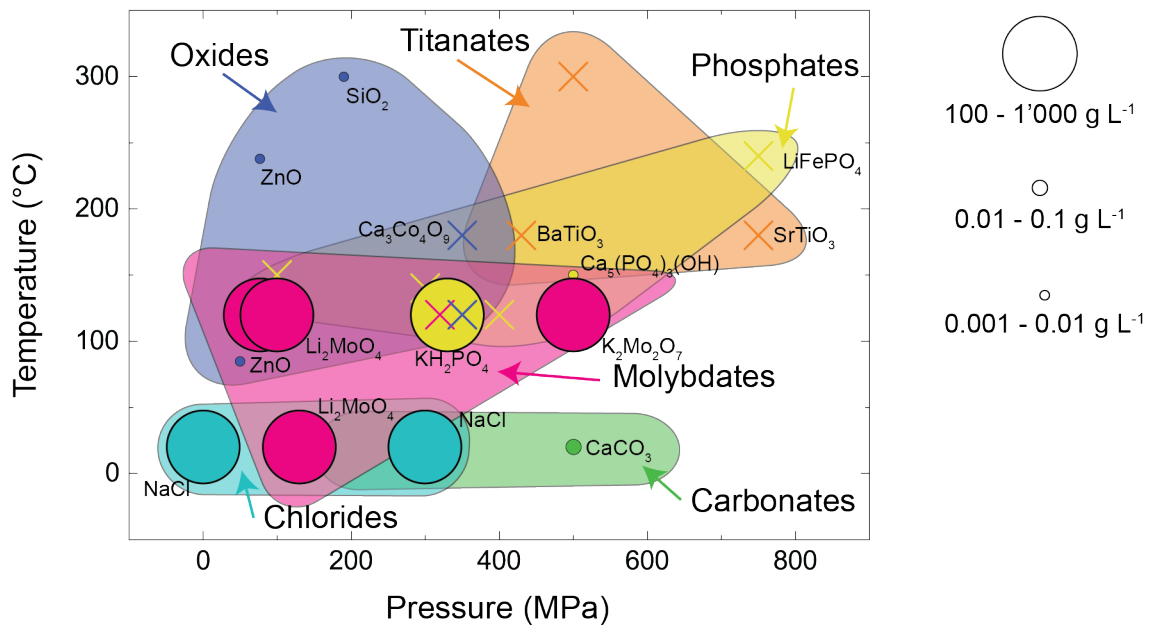
Figure 1.11: Summary of the processing parameters needed for cold sintering of a wide range of different materials.
The size of the circles is proportional to the solubility of the material. A cross stands for materials with no solubility data available.

Many of the research groups mentioned above have been following up on their cold sintering research. Prof Jantunen has published several papers on the densification behavior and further applications of Li_2MoO_4 [28-34]. The team has managed to produce several composite materials, for example with titanium dioxide and published the first magnetic composite produced at room temperature. The group of Prof Guillon has investigated the cold sintering of ZnO in more detail [35, 36]. They applied established methods to analyze the sintering mechanisms of relevance for cold sintering and found that grain boundary diffusion is not the controlling mechanism for the densification of samples subjected to field-assisted sintering/spark plasma sintering. These authors also evaluated the formation of defects with Kelvin Probe Force Microscopy to conclude that the grain boundaries are highly defective and present much higher surface energy compared to the bulk material. Prof. Drouet's team further investigated the cold sintering behavior of apatite, with a focus on methods that enable the crystallization of amorphous calcium phosphate at very low temperatures [37]. Prof Randall's team has published more than 30 papers on different materials in the past 3 years, including barium titanate ($BaTiO_3$) and zirconium oxide (ZrO_2) [38-69], proving the general applicability of the method.

To summarize this growing body of work on cold sintering and compare the data with the hypothesized underlying mechanisms, we have compiled in Figure 1.11 the pressure and temperature ranges necessary to densify materials in the presence of an aqueous liquid phase.

Only materials that achieved a relative density higher than 80% after the cold sintering process were considered. The size of the circles in Figure 1.11 additionally represents, when available, the material solubility in water at room temperature. The solubility of materials at temperatures higher than room temperature is difficult to access experimentally, even more so in hydrothermal conditions. Yet the collected solubility data can provide an indication of how prone the compositions are to dissolve spontaneously in water and thus how easy they can densify by cold sintering via a dissolution-diffusion-precipitation mechanism. A table with all the data used in Figure 1.11 can be found in Appendix A, Table A.1.

In general, materials that are highly soluble in water ($100 - 1000$ g L^{-1}) can be cold sintered at lower temperatures and at lower pressures. Conversely, materials that are insoluble in water at ambient conditions need to be processed at high temperature and at high pressure, typically under hydrothermal conditions. There are, however, two materials that should be highlighted: calcium carbonate can be processed at room temperature and ZnO at temperatures below 100 °C despite their low solubility in water.

1.3.2. Cold Sintering of Ceramic – Polymer – Composites

In several of the publications mentioned in the previous paragraph, the main motivation to develop a cold sintering process was the production of ceramic – polymer composites. With such low sintering temperatures, polymer/ceramic composites could be manufactured in a one-step process during which both the ceramic and the polymer phases are consolidated at the same time. Some of the results obtained for composites produced by cold sintering are presented below.

In 2015, Brouillet *et al.* from Université de Toulouse [70] published a paper in which the fabrication of an apatite/cellulose composite is described. Densification was achieved using a pressure of 100 MPa and a temperature of 150 °C. Similarly to the work performed by Grossin *et al.* [21], the authors densified the sample using SPS. The obtained samples showed tensile strength higher than 10 MPa.

The group of Prof. Randall also published results on the preparation of ceramic – polymer composites but this time for functional applications. Guo J. *et al.* [42] produced samples with Li_2MoO_4 and PTFE, whereas Funahashi *et al.* [45] published a method to make a $ZnO - Ca_3Co_4O_9$ – PTFE composite for thermoelectric generation.

1.4. Aim and Structure of this Thesis

The aim of this thesis is to investigate the mechanisms responsible for the room-temperature cold sintering of vaterite nanoparticles, a metastable polymorph of calcium carbonate. We chose this as a model system because no temperature is needed for the densification, which ultimately makes it easier to perform and observe the compaction process compared to cold sintering processes involving hydrothermal conditions. Moreover, calcium carbonates are attractive CO_2-based materials with potentially carbon-neutral footprint.

We start by investigating the cold sintering of vaterite on a global scale under different process parameters, such as pressure, temperature, solvent and crystallinity (chapter 2). The experimental results are interpreted on the basis of existing analytical models to better understand the observed densification behavior.

We then apply the gained knowledge to other materials to evaluate whether the behavior observed in vaterite could be employed to lower the cold sintering temperature of other compositions (chapter 3). We chose ZnO particles for this part of the study because of its similar hierarchical structure to vaterite. Hydroxyapatite particles were also investigated due to its hierarchical structure as well as its ability to form crystalline precipitates in an aqueous environment at room temperature. These features were hypothesized to be important for the cold sintering of vaterite powder.

Finally, we investigate the cold sintering of vaterite on a local scale by using complementary analytical approaches (chapter 4). With the help of *in situ* X-Ray tomography, the deformation behavior of the particle compact is visualized under an externally applied stress. This is complemented by instrumented micro and nano indentation measurements to identify the most important length scale for the room-temperature cold sintering of vaterite powder.

References

[1]   R.M. German, SINTERING - From Emperical Observations to Scientific Principles, 1. ed., Elsevier2014.

[2]   M.N. Rahaman, Ceramic Processing and Sintering, 2 ed., CRC Press2003.

[3]   H. Djohari, J.I. Martínez-Herrera, J.J. Derby, Transport mechanisms and densification during sintering: I. Viscous flow versus vacancy diffusion, Chem. Eng. Sci. 64(17) (2009) 3799-3809.

References

_____

[4]   A. Fick, Ueber Diffusion, Annalen der Physik 170(1) (1855) 59-86.

[5]   C. Herring, Diffusional Viscosity of a Polycrystalline Solid, J. Appl. Phys. 21(5) (1950) 437-445.

[6]   F. Bouville, E. Maire, S. Meille, B. Moortèle, A.J. Stevenson, S. Deville, Strong, tough and stiff bioinspired ceramics from brittle constituents, Nat. Mater. 13(5) (2014) 508-514.

[7]   K.J. Koester, J.W. Ager, R.O. Ritchie, The true toughness of human cortical bone measured with realistically short cracks, Nat. Mater. 7(8) (2008) 672-677.

[8]   J.-P. Gratier, D.K. Dyshe, F. Renard, Chapter 2 - The Role of Pressure Solution Creep in the Ductility of the Earth's Upper Crust, Adv Geophys 54 (2013) 47-179.

[9]   D. Croizé, F. Renard, J.-P. Gratier, Chapter 3 - Compaction and Porosity Reduction in Carbonates: A Review of Observations, Theory, and Experiments, Adv Geophys 54 (2013) 181-238.

[10]   S. Ehrenberg, P.H. Nadeau, Sandstone vs. carbonate petroleum reservoirs: A global perspective on porosity-depth and porosity-permeability relationships, AAPG Bulletin 89 (2005) 435-445.

[11]   J.W. Schmoker, R.B. Halley, Carbonate porosity versus depth: a predictable relation for south Florida, (1982).

[12]   B. den Brok, M. Zahid, C.W. Passchier, Pressure solution compaction of sodium chlorate and implications for pressure solution in NaCl, Tectonophysics 307(3-4) (1999) 297-312.

[13]   X. Zhang, C.J. Spiers, C.J. Peach, Compaction creep of wet granular calcite by pressure solution at 28°C to 150°C, J. Geophys. Res. 115(B9) (2010).

[14]   X. Zhang, C.J. Spiers, Compaction of granular calcite by pressure solution at room temperature and effects of pore fluid chemistry, Int. J. Rock Mech. Min. Sci. 42(7-8) (2005) 950-960.

[15]   R.H. Brzesowsky, S.J.T. Hangx, N. Brantut, C.J. Spiers, Compaction creep of sands due to time-dependent grain failure: Effects of chemical environment, applied stress, and grain size, J. Geophys. Res. Solid Earth 119(10) (2014) 7521-7541.

[16]   S.M. Wiederhorn, Subcritical Crack Growth in Ceramics, in: R.C. Bradt, D.P.H. Hasselman, F.F. Lange (Eds.), Fracture Mechanics of Ceramics: Volume 2 Microstructure, Materials, and Applications, Springer US, Boston, MA, 1974, pp. 613-646.

_____

[17]   T. Ibn-Mohammed, C.A. Randall, K.B. Mustapha, J. Guo, J. Walker, S. Berbano, S.C.L. Koh, D. Wang, D.C. Sinclair, I.M. Reaney, Decarbonising ceramic manufacturing: A techno-economic analysis of energy efficient sintering technologies in the functional materials sector, J. Eur. Ceram. Soc. 39(16) (2019) 5213-5235.

[18]   K. Caldeira, A.K. Jain, M.I. Hoffert, Climate Sensitivity Uncertainty and the Need for Energy Without CO2 Emission, Science 299(5615) (2003) 2052.

[19]   D.S. Jenkinson, D.E. Adams, A. Wild, Model estimates of CO2 emissions from soil in response to global warming, Nature 351(6324) (1991) 304-306.

[20]   E.Y. Gutmanas, A. Rabinkin, M. Roitberg, Cold sintering under high pressure, Scr. Metall. 13(1) (1979) 11-15.

[21]   D. Grossin, S. Rollin-Martinet, C. Estournès, F. Rossignol, E. Champion, C. Combes, C. Rey, C. Geoffroy, C. Drouet, Biomimetic apatite sintered at very low temperature by spark plasma sintering: Physico-chemistry and microstructure aspects, Acta Biomater. 6(2) (2010) 577-585.

[22]   H. Kähäri, M. Teirikangas, J. Juuti, H. Jantunen, Dielectric Properties of Lithium Molybdate Ceramic Fabricated at Room Temperature, J. Am. Ceram. Soc. 97(11) (2014) 3378-3379.

[23]   B. Dargatz, J. Gonzalez-Julian, O. Guillon, Improved compaction of ZnO nano-powder triggered by the presence of acetate and its effect on sintering, Sci. Technol. Adv. Mater. 16(2) (2015) 025008.

[24]   J. Guo, H. Guo, A.L. Baker, M.T. Lanagan, E.R. Kupp, G.L. Messing, C.A. Randall, Cold Sintering: A Paradigm Shift for Processing and Integration of Ceramics, Angew. Chem. Int. Ed. 55(38) (2016) 11457-11461.

[25]   F. Bouville, A.R. Studart, Geologically-inspired strong bulk ceramics made with water at room temperature, Nat. Commun. 8 (2017) 14655.

[26]   W.B. Hong, L. Li, M. Cao, X.M. Chen, Plastic deformation and effects of water in room-temperature cold sintering of NaCl microwave dielectric ceramics, J. Am. Ceram. Soc. 101(9) (2018) 4038-4043.

[27]   A. Ndayishimiye, A. Largeteau, S. Mornet, M. Duttine, M.-A. Dourges, D. Denux, M. Verdier, M. Gouné, T. Hérisson de Beauvoir, C. Elissalde, G. Goglio, Hydrothermal Sintering for Densification of Silica. Evidence for the Role of Water, J. Eur. Ceram. Soc. 38(4) (2018) 1860-1870.

[28]   H. Kähäri, M. Teirikangas, J. Juuti, H. Jantunen, Improvements and Modifications to Room-Temperature Fabrication Method for Dielectric Li2MoO4 Ceramics, J. Am. Ceram. Soc. 98(3) (2015) 687-689.

[29]   H. Kähäri, M. Teirikangas, J. Juuti, H. Jantunen, Room-temperature fabrication of microwave dielectric Li2MoO4–TiO2 composite ceramics, Ceram. Int. 42(9) (2016) 11442-11446.

[30]   H. Kähäri, P. Ramachandran, J. Juuti, H. Jantunen, Room-temperature-densified Li2MoO4 ceramic patch antenna and the effect of humidity, International Journal of Applied Ceramic Technology 14(1) (2017) 50-55.

[31]   M. Väätäjä, H. Kähäri, J. Juuti, H. Jantunen, Li2MoO4-based composite ceramics fabricated from temperature- and atmosphere-sensitive MnZn ferrite at room temperature, J. Am. Ceram. Soc. 100(8) (2017) 3626-3635.

[32]   M. Nelo, J. Peräntie, T. Siponkoski, J. Juuti, H. Jantunen, Upside-down composites: Electroceramics without sintering, Applied Materials Today 15 (2019) 83-86.

[33]   P. Ramachandran, H. Kähäri, J. Juuti, H. Jantunen, Room temperature densified ceramics for weight optimized circular polarized GPS antenna design, Microwave and Optical Technology Letters 60(4) (2018) 1061-1066.

[34]   M. Nelo, H. Liimatainen, M. Väätäjä, J. Ukkola, J. Juuti, H. Jantunen, Solid Air—Low Temperature Manufacturing of Ultra-Low Permittivity Composite Materials for Future Telecommunication Systems, Frontiers in Materials 6(94) (2019).

[35]   J. Gonzalez-Julian, K. Neuhaus, M. Bernemann, P.J. da Silva, A. Laptev, M. Bram, O. Guillon, Unveiling the mechanisms of cold sintering of ZnO at 250 °C by varying applied stress and characterizing grain boundaries by Kelvin Probe Force Microscopy, Acta Mater. 144 (2018) 116-128.

[36]   J.G. Pereira da Silva, M. Bram, A.M. Laptev, J. Gonzalez-Julian, Q. Ma, F. Tietz, O. Guillon, Sintering of a sodium-based NASICON electrolyte: A comparative study between cold, field assisted and conventional sintering methods, J. Eur. Ceram. Soc. 39(8) (2019) 2697-2702.

[37]   C. Ortali, I. Julien, M. Vandenhende, C. Drouet, E. Champion, Consolidation of bone-like apatite bioceramics by spark plasma sintering of amorphous carbonated calcium phosphate at very low temperature, J. Eur. Ceram. Soc. 38(4) (2018) 2098-2109.

[38]   A. Baker, H. Guo, J. Guo, C. Randall, Utilizing the Cold Sintering Process for Flexible–Printable Electroceramic Device Fabrication, J. Am. Ceram. Soc. 99(10) (2016) 3202-3204.

[39] H. Guo, J. Guo, A. Baker, C.A. Randall, Hydrothermal-Assisted Cold Sintering Process: A New Guidance for Low-Temperature Ceramic Sintering, ACS Appl. Mater. Interfaces 8(32) (2016) 20909-20915.

[40] H. Guo, A. Baker, J. Guo, C.A. Randall, Protocol for Ultralow-Temperature Ceramic Sintering: An Integration of Nanotechnology and the Cold Sintering Process, ACS Nano 10(11) (2016) 10606-10614.

[41] H. Guo, A. Baker, J. Guo, C.A. Randall, Cold Sintering Process: A Novel Technique for Low-Temperature Ceramic Processing of Ferroelectrics, J. Am. Ceram. Soc. 99(11) (2016) 3489-3507.

[42] J. Guo, S.S. Berbano, H. Guo, A.L. Baker, M.T. Lanagan, C.A. Randall, Cold Sintering Process of Composites: Bridging the Processing Temperature Gap of Ceramic and Polymer Materials, Adv. Funct. Mater. 26(39) (2016) 7115-7121.

[43] S.S. Berbano, J. Guo, H. Guo, M.T. Lanagan, C.A. Randall, Cold sintering process of Li1.5Al0.5Ge1.5(PO4)3 solid electrolyte, J. Am. Ceram. Soc. 100(5) (2017) 2123-2135.

[44] S. Funahashi, J. Guo, H. Guo, K. Wang, A.L. Baker, K. Shiratsuyu, C.A. Randall, Demonstration of the cold sintering process study for the densification and grain growth of ZnO ceramics, J. Am. Ceram. Soc. 100(2) (2017) 546-553.

[45] S. Funahashi, H. Guo, J. Guo, A.L. Baker, K. Wang, K. Shiratsuyu, C.A. Randall, Cold sintering and co-firing of a multilayer device with thermoelectric materials, J. Am. Ceram. Soc. 100(8) (2017) 3488-3496.

[46] H. Guo, T.J.M. Bayer, J. Guo, A. Baker, C.A. Randall, Cold sintering process for 8 mol%Y2O3-stabilized ZrO2 ceramics, J. Eur. Ceram. Soc. 37(5) (2017) 2303-2308.

[47] H. Guo, J. Guo, A. Baker, C.A. Randall, Cold sintering process for ZrO2-based ceramics: significantly enhanced densification evolution in yttria-doped ZrO2, J. Am. Ceram. Soc. 100(2) (2017) 491-495.

[48] H. Guo, T.J.M. Bayer, J. Guo, A. Baker, C.A. Randall, Current progress and perspectives of applying cold sintering process to ZrO2-based ceramics, Scr. Mater. 136 (2017) 141-148.

[49] J. Guo, A.L. Baker, H. Guo, M. Lanagan, C.A. Randall, Cold sintering process: A new era for ceramic packaging and microwave device development, J. Am. Ceram. Soc. 100(2) (2017) 669-677.

[50] J.-P. Maria, X. Kang, R.D. Floyd, E.C. Dickey, H. Guo, J. Guo, A. Baker, S. Funihashi, C.A. Randall, Cold sintering: Current status and prospects, J. Mater. Res. 32(17) (2017) 3205-3218.

[51] J.-H. Seo, J. Guo, H. Guo, K. Verlinde, D.S.B. Heidary, R. Rajagopalan, C.A. Randall, Cold sintering of a Li-ion cathode: LiFePO4-composite with high volumetric capacity, Ceram. Int. 43(17) (2017) 15370-15374.

[52] R. Boston, J. Guo, S. Funahashi, A.L. Baker, I.M. Reaney, C.A. Randall, Reactive intermediate phase cold sintering in strontium titanate, RSC Adv. 8(36) (2018) 20372-20378.

[53] D. Wang, H. Guo, C.S. Morandi, C.A. Randall, S. Trolier-McKinstry, Cold sintering and electrical characterization of lead zirconate titanate piezoelectric ceramics, APL Materials 6(1) (2018) 016101.

[54] J. Guo, R. Floyd, S. Lowum, J.-P. Maria, T.H.d. Beauvoir, J.-H. Seo, C.A. Randall, Cold Sintering: Progress, Challenges, and Future Opportunities, Annu. Rev. Mater. Res. 49(1) (2019) 275-295.

[55] S.H. Bang, T. Herisson De Beauvoir, C.A. Randall, Densification of thermodynamically unstable tin monoxide using cold sintering process, J. Eur. Ceram. Soc. 39(4) (2019) 1230-1236.

[56] W.-T. Chen, A.E. Gurdal, S. Tuncdemir, J. Guo, H. Guo, C.A. Randall, Considering the possibility of bonding utilizing cold sintering for ceramic adhesives, J. Am. Ceram. Soc. 100(12) (2017) 5421-5432.

[57] T.H. de Beauvoir, S. Dursun, L. Gao, C. Randall, New Opportunities in Metallization Integration in Cofired Electroceramic Multilayers by the Cold Sintering Process, ACS Applied Electronic Materials 1(7) (2019) 1198-1207.

[58] J. Guo, H. Guo, D.S.B. Heidary, S. Funahashi, C.A. Randall, Semiconducting properties of cold sintered V2O5 ceramics and Co-sintered V2O5-PEDOT:PSS composites, J. Eur. Ceram. Soc. 37(4) (2017) 1529-1534.

[59] J. Guo, B. Legum, B. Anasori, K. Wang, P. Lelyukh, Y. Gogotsi, C.A. Randall, Cold Sintered Ceramic Nanocomposites of 2D MXene and Zinc Oxide, Adv. Mater. 30(32) (2018) 1801846.

[60] J. Guo, N. Pfeiffenberger, A. Beese, A. Rhoades, L. Gao, A. Baker, K. Wang, A. Bolvari, C.A. Randall, Cold Sintering Na2Mo2O7 Ceramic with Poly(ether imide) (PEI) Polymer to Realize High-Performance Composites and Integrated Multilayer Circuits, ACS Applied Nano Materials 1(8) (2018) 3837-3844.

[61] J. Guo, X. Zhao, T. Herisson De Beauvoir, J.-H. Seo, S.S. Berbano, A.L. Baker, C. Azina, C.A. Randall, Recent Progress in Applications of the Cold Sintering Process for Ceramic–Polymer Composites, Adv. Funct. Mater. 28(39) (2018) 1801724.

_____

[62] D.S.B. Heidary, J. Guo, J.-H. Seo, H. Guo, R. Rajagopalan, C.A. Randall, Microstructures and electrical properties of V2O5and carbon-nanofiber composites fabricated by cold sintering process, Jpn. J. Appl. Phys. 57(2) (2018) 025702.

[63] W. Lee, C.K. Lyon, J.-H. Seo, R. Lopez-Hallman, Y. Leng, C.-Y. Wang, M.A. Hickner, C.A. Randall, E.D. Gomez, Ceramic–Salt Composite Electrolytes from Cold Sintering, Adv. Funct. Mater. 29(20) (2019) 1807872.

[64] J.-H. Seo, K. Verlinde, J. Guo, D.S.B. Heidary, R. Rajagopalan, T.E. Mallouk, C.A. Randall, Cold sintering approach to fabrication of high rate performance binderless LiFePO4 cathode with high volumetric capacity, Scr. Mater. 146 (2018) 267-271.

[65] J.-H. Seo, K. Verlinde, R. Rajagopalan, E.D. Gomez, T.E. Mallouk, C.A. Randall, Cold sintering process for fabrication of a high volumetric capacity Li4Ti5O12 anode, Materials Science and Engineering: B 250 (2019) 114435.

[66] D. Sohrabi Baba Heidary, M. Lanagan, C.A. Randall, Contrasting energy efficiency in various ceramic sintering processes, J. Eur. Ceram. Soc. 38(4) (2018) 1018-1029.

[67] D. Wang, D. Zhou, K. Song, A. Feteira, C.A. Randall, I.M. Reaney, Cold-Sintered C0G Multilayer Ceramic Capacitors, Advanced Electronic Materials 5(7) (2019) 1900025.

[68] X. Zhao, J. Guo, K. Wang, T. Herisson De Beauvoir, B. Li, C.A. Randall, Introducing a ZnO–PTFE (Polymer) Nanocomposite Varistor via the Cold Sintering Process, Adv. Eng. Mater. 20(7) (2018) 1700902.

[69] Y. Zhao, S.S. Berbano, L. Gao, K. Wang, J. Guo, K. Tsuji, J. Wang, C.A. Randall, Cold-sintered V2O5-PEDOT:PSS nanocomposites for negative temperature coefficient materials, J. Eur. Ceram. Soc. 39(4) (2019) 1257-1262.

[70] F. Brouillet, D. Laurencin, D. Grossin, C. Drouet, C. Estournes, G. Chevallier, C. Rey, Biomimetic apatite-based composite materials obtained by spark plasma sintering (SPS): physicochemical and mechanical characterizations, J. Mater. Sci. Mater. Med. 26(8) (2015) 223.

Chapter 2: Cold Densification and Sintering of Nanovaterite by Pressing with Water

Abstract

While dissolution-precipitation, plastic deformation and fracture mechanisms have been proposed to explain the compaction of carbonates in geological formations, the role of these mechanisms on the densification process of calcium carbonate nanoparticles in synthetic systems remains poorly understood. Here, we systematically investigate the effect of pH of the aqueous phase between 1 and 7, temperature between 10 and 90 °C and pressure between 10 and 800 MPa on the cold compaction of nanovaterite powder with water to shed light on the microscopic mechanisms underlying this unique densification process. Compaction experiments reveal that the applied pressure plays a major role on the densification of calcium carbonate nanopowder with water. Our experimental data thus suggest that plastic deformation or subcritical crack growth might be important densification mechanisms for nanovaterite particles. These findings provide a new perspective into the cold compaction of nanopowders with water and may open promising routes for the manufacturing of CO_2-based structural materials at mild processing conditions.

2.1. Introduction

Calcium carbonates constitute a major fraction of the Earth's crust and are widely used in industry as building material, rheology modifiers or inorganics fillers [1, 2]. Given the importance of sustainable technologies that mitigate the greenhouse effects, carbonates have also attracted interest as a potential material for carbon sequestration [3, 4]. Carbon fixation in the form of carbonates is possible by injecting CO_2 in the deep ocean where it is absorbed by rocks through a chemical weathering process [5]. In analogy to carbonate-based mollusk shells made by living organisms, CO_2-based inorganic materials have also been envisioned as sustainable building blocks for the fabrication of strong building materials with neutral or even negative carbon footprint [6]. However, the processing of carbonates into the dense microstructures found in mollusk shells and other biological materials remains a major challenge. In addition to remarkable fracture resistance, these mineralized biological shells are produced in water at room temperature, in contrast to the high temperatures and carbon footprint associated with state-of-the-art building materials.

Inspired by the densification of carbonates in geological processes, we have recently shown that calcium carbonates in the form of vaterite nanoparticles can be densified under pressure into strong and stiff bulk parts using water at room temperature [6]. Vaterite is a metastable calcium carbonate polymorph that can be obtained as nanoparticles using straightforward precipitation protocols [7]. In contrast to the geological timescales needed for the densification of coarse-grained limestone in nature, the nano-sized vaterite particles can reach up to 90%

relative density in less than 30 minutes when subjected to uniaxial pressures in the range of 10 – 800 MPa. The ability to densify calcium carbonate using water at room temperature and thus obtain bulk parts with mechanical properties exceeding those of stone and concrete makes this an attractive technology for the sustainable manufacturing of CO_2-based materials with minimal carbon footprint. Earlier work on oxide-based ceramics have also reported on the densification of nanoparticle compacts under hydrothermal conditions at pressures and temperatures typically ranging from 40 to 350 MPa and 85 to 250 °C, respectively.[8-11]. This process, referred to as cold sintering, was already applied to densify various types of oxide particles, thus allowing for the fabrication of functional ceramics and composites at temperatures up to 1000 °C lower compared to conventional sintering routes [11].

Several physical and chemical mechanisms have been proposed to describe the densification of carbonates and oxides in geological and synthetic conditions, respectively [12, 13]. These include stress-induced dissolution-precipitation processes, plastic deformation, as well as particle fracture and rearrangement assisted by subcritical crack growth [14-16]. Because of the higher temperatures and hydrothermal conditions involved, dissolution-precipitation processes seems to play a major role in the cold sintering of oxides. Recent work has shown that the creep rate of ZnO compacts exhibits a strong dependence on the applied stress, suggesting that plastic deformation also takes place during hydrothermal cold sintering of this and other oxides [17]. A strong stress dependence has been reported also for carbonaceous rocks under creep. Since plastic deformation of these rocks at room temperature is limited, grain fracture and rearrangement facilitated by subcritical crack growth was proposed as a possible mechanism to explain densification of minerals in geological formations [18-21]. Our earlier work on the geologically-inspired densification of nanovaterite powder has clearly shown the importance of water for the sintering process. However, the mechanisms responsible for the water-assisted densification of these calcium carbonate nanoparticles are still unclear.

Here, we systematically investigate the effect of processing parameters on the room-temperature compaction behavior of selected calcium carbonate powders to shed light onto the mechanisms controlling the water-assisted sintering of vaterite nanoparticles during uniaxial pressing. The influence of the applied pressure, the temperature, the crystalline morphology of the powder and the pH of the aqueous medium is first studied using compaction experiments under well-defined mechanical loading conditions. The evolution of the relative density at a constant displacement rate is then thoroughly analyzed to quantify the effect of the applied pressure on the first stage of the compaction process. By keeping the applied stress constant after the first compaction stage, the creep response of the vaterite parts with water was evaluated at different mechanical loading levels. Finally, the obtained experimental data are quantitatively compared to predictions from sintering and geological

models to discuss the possible physical and chemical mechanisms controlling the room-temperature densification of nanovaterite with water.

2.2. Materials and Methods

2.2.1. Synthesis of Nanovaterite Particles

Nanovaterite particles were synthesized following the method originally proposed by Parakhonskiy *et al*. [7]. Briefly, 16 ml of a calcium chloride 2 mol L^{-1} aqueous solution (calcium chloride dihydrate, $CaCl_2 \cdot 2H_2O$, Merck, Germany,) and of a sodium carbonate 2 mol L^{-1} aqueous solution (Na_2CO_3, Sigma-Aldrich, Germany) were each mixed with 80 ml ethylene glycol (technical, VWR, France), resulting in two solutions with a salt concentration of 0.36 mol L^{-1}. The Na_2CO_3 − ethylene glycol solution was added to $CaCl_2$ − ethylene glycol solution under vigorous stirring. The precipitates formed were kept in the solution under stirring for 1 hour before centrifugation at 4500 rpm for 15 min. The particles were then washed with ethanol (94% denatured with toluene, Alcosuisse) twice before they were dried in the oven at 60 °C for one day and 120 °C for another day.

2.2.2. Synthesis of Amorphous Calcium Carbonate (ACC) Particles

ACC nanoparticles were synthesized following the protocol developed by Avaro *et al*. [22]. Following this procedure, water enriched in carbon dioxide was first added to a saturated calcium hydroxide solution ($K_{sp}(Ca(OH)_2 = 5.5 \times 10^{-6}$) in a stepwise manner. The CO_2-enriched solution was prepared by bubbling CO_2 into milliQ water set at 7 °C for 30 min. 50 mL of the calcium hydroxide solution kept at 7 °C was placed into a plastic beaker and the pH was monitored with a Metrohm pH electrode (model 6.0256.100). The CO_2-enriched solution was afterwards added drop-by-drop to the calcium hydroxide solution at a rate of 10 to 12 mL min^{-1} until the pH dropped from 12.43 (pH of $Ca(OH)_2$ saturated solution) to pH 10.00. The solution was then poured into absolute ethanol until a volume ratio of initial calcium hydroxide solution to ethanol of 1:20 was reached. The resulting solution was stirred with a magnetic stirrer for 3 min. After removing the magnetic stirrer, the solution was left to sediment for 30 min. Sedimented ACC was then transferred into a falcon tube and centrifuged at 9000 rpm for 10 min in a benchtop centrifuge. In the following, the supernatant solution was removed, the ACC nanoparticles were re-suspended in acetone and centrifuged again, re-suspended in acetone and stored. To obtain dry particles for the compaction experiments, we

slip casted the ACC suspension onto a small gypsum mold. Capillary forces induced by the pores of the model removed the acetone from the suspension, concentrating the ACC particles. The particles were then dried at 60 °C to eliminated any residual acetone. The ACC agglomerates obtained after drying were ground with a pestle in a mortar to obtain a fine powder.

2.2.3. Preparation of Calcite Particles

Precipitated $CaCO_3$ particles (Fisher Scientific, UK) were ground for 1 hour in a planetary mill at 300 rpm using an alumina crucible loaded with 5 mm alumina spheres. The particles were then separated from the solution by centrifugation and washed with ethanol twice.

2.2.4. Particle Characterization

The morphology of the particles was analyzed by scanning electron microscopy (SEM, LEO1530, Zeiss, Germany). Prior to acquiring images, the samples were coated with a 5 nm layer of Pt in order to make the surface electrically conductive. Images were obtained using a secondary electron detector operated at a 2 kV acceleration voltage. Crystallographic phases were identified by X-ray diffraction (XRD, Panalytical X'Pert PRO MPD, Netherlands) using a Cu anode (generation voltage 40 kV, tube current 45 mA) and a monochromator. The time per step was set to 200 s and the step size to 0.0167 while varying the 2θ angle from 10° to 70°.

2.2.5. Compaction Experiments

In a typical compaction experiment, 0.3 g of the particles were mixed with 0.75 ml of water. The resulting liquid-powder mixture was then inserted into a pressing tool (Modell 10, Gr. 2, diameter 11 mm, P/O Weber, Germany) placed in a mechanical testing machine (Instron 8562, Instron) equipped with a 100 kN load cell. After applying a preload of 200 N, the sample was pressed at a displacement rate of 0.5 mm min^{-1} until the targeted force was reached (stage 1, Figure 2.1). At this point, the machine was switched to load control mode, where the displacement is constantly adjusted in order to keep the set load (stage 2, Figure 2.1). Because of the high mechanical loads applied during compaction, the contribution of the machine and of the pressing tool to the total measured displacement was measured and used to correct the raw data. The correction curve was recorded using an empty pressing tool and was then used to calculate the machine spring constant $K_{machine}$. The corrected sample displacement at each load was obtained using the following formula: $\Delta L_{powder}(F) = \Delta L_{measured} - K_{machine}F$, where ΔL_{powder} is the displacement of the powder only, $\Delta L_{measured}$ is the total measured displacement, and F is the applied load. We fitted a polynomial function (degree 40) to the

acquired displacement data and used this fitted function to obtain a smoothed displacement derivative curve. To calculate the density of the sample during compaction, we measured the mass of the sample 24 hours after the testing. During this period, the sample was kept in the oven at 60 °C to remove all the solvent. For the calculations of the relative density we used the following specific gravity values: 2.54 g cm^{-3} for vaterite [23], and 2.71 g cm^{-3} for calcite [23]. Compaction experiments at different temperatures were conducted by heating the pressing tool with a cylindrical heating element (MB2J1JN1, watlow, USA). The heating element was wrapped and tightened around the pressing tool in order to apply the heat as close as possible to the sample. The temperature reported in these experiments was measured in the heating element.

2.2.6. Calculation of the Theoretical Particle Solubility

We used thermodynamic equilibrium constants to estimate the solubility of the calcium carbonate powders. The estimated data are based on literature values for calcite. The solubility, x, in mol L^{-1} was obtained from the relation: $x = \sqrt{K_{sp}/\alpha_2}$, where $\alpha_2 = K_{a1}K_{a2}/([H_3O^+]^2 + K_{a1}[H_3O^+] + K_{a1}K_{a2})$, K_{sp} is the solubility product ($10^{-8.4}$), and K_{a1} and K_{a2} are the equilibrium constants for the protonation/deprotonation reactions of calcium carbonates ($10^{-6.5}$ and $10^{-10.3}$ respectively) [24].

2.3. Results and Discussion

The compaction behavior of selected calcium carbonate powders with water was studied by performing uniaxial pressing experiments under controlled pH, temperature and pressure with particles of different polymorph type. In these tests, the powder is first subjected to a constant displacement rate until the target plateau stress, σ, is achieved (stage 1). This is followed by a creep experiment at constant external pressure (stage 2). The response of the powder to this stress profile is measured as a net shrinkage, ΔL, that can be directly converted into the actual relative density of the compact (ρ) (Figure 2.1).

Mechanical compaction tests were first performed on calcium carbonate powders in the form of vaterite, calcite and amorphous CaCO$_3$ (ACC) particles. The powders differ significantly in terms of particle size and morphology (Figure 2.2a-c). The vaterite powder displays a hierarchical morphology consisting of 40 nm primary particles that are assembled into larger 500 nm-sized agglomerates. By contrast, the amorphous calcium carbonate powder comprises nanoparticles of 50 nm without noticeable agglomeration. Whereas the amorphous calcium carbonate is indeed amorphous after synthesis, as assessed by FTIR (Appendix B Figure B.2), the XRD analysis done after a few weeks in acetone storage and right before pressing shows
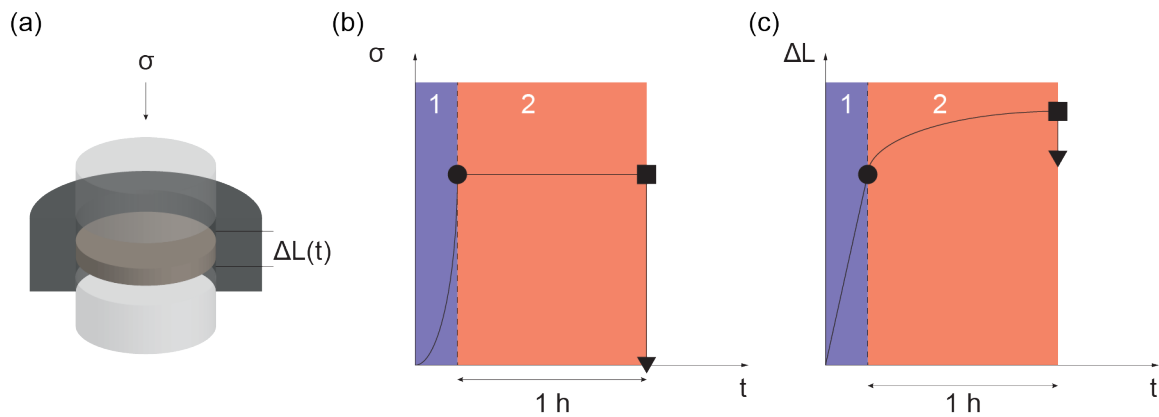
Figure 2.1: Compaction setup, measuring protocol and experimental data used to study the cold densification of calcium carbonate. *(a) Schematics of the uniaxial pressing tool with applied stress σ and strain $\Delta L(t)$ as input and output parameters, respectively. (b) Two-stage protocol utilized for the characterization of the compaction process. In stage 1, the powder is subjected to a constant displacement rate until a prescribed stress is reached. In stage 2, a creep experiment is performed at fixed applied stress. The symbols indicate the end of stage 1 (●), the end of stage 2 (■) and the final stress and deformation after unloading the sample (▼). (c) Schematics of the typical deformation response obtained throughout each one of the two compaction stages.*

already the presence of a small fraction of crystalline calcite (Appendix B Figure B.3). Finally, the calcite powder contains particles with size on the order of 1 μm, which were obtained upon planetary milling of as-received powder. This grinding process was conducted to reduce the size of the calcite particles to a value closer to that of the nanovaterite powder.

The compaction behavior of powders subjected to a uniaxial pressure of 500 MPa was found to change significantly depending on the size, morphology and crystalline structure of the calcium carbonate particles (Figure 2.2d-f). While the partially crystallized ACC and calcite specimens show a steeper increase in relative density in the first stage, the vaterite samples densify predominantly by creep in the second stage. Eventually, the relative density of the vaterite compacts pressed with water reach 86%, as compared to 84% for the calcite powder. These final relative density values are 6-15% higher than those obtained from samples subjected to the same stress level in the dry state (Figure 2.2d-f). In contrast to the vaterite powder, the ACC particles were found to partially transform into calcite initially and during the compaction procedure (Appendix B Figure B.2-Figure B.5). Because the specific gravity of ACC (1.5 g cm^{-3}) [25] is significantly lower than that of calcite (2.7 g cm^{-3}) [23] and the extent of transformation is unknown, the compaction profile of the partially crystallized ACC particles is displayed in terms of the absolute rather than the relative density of the compact (Figure 2.2f).

In addition to the compaction profile, the mechanical properties of as-pressed specimens are also strongly dependent on the calcium carbonate powder used. Compacts obtained by pressing vaterite nanoparticles with water exhibit fracture strength comparable or even higher
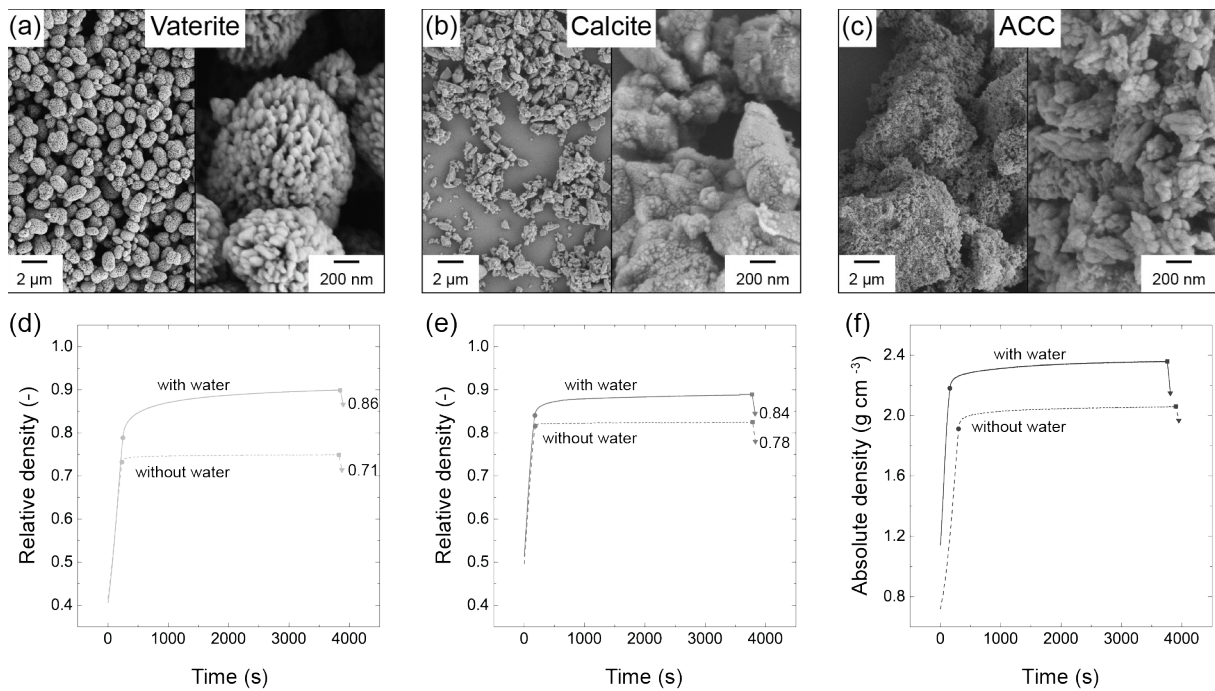
Figure 2.2: Compaction behavior of calcium carbonate powders with distinct particle crystallinities and morphologies. (a-c) Scanning electron microscopy images of the particles before pressing of (a) nanovaterite, (b) ball-milled calcite and (c) partially crystallized amorphous calcium carbonate. (d-f) Evolution of the relative density of the compacts made out of (d) vaterite, (e) calcite, and (f) ACC during uniaxial pressing at 500 MPa with and without water. Data for both stages 1 and 2 is shown. The final densities achieved with distinct powders at the end of the compaction process are indicated inside the graphs.

than those of concrete and stone [6]. By contrast, samples made with partially crystallized ACC and calcite were not strong enough to be manipulated and mechanically tested.

The low mechanical strength of the calcite and partially crystallized ACC specimens contrasts with the high relative densities achieved with these powders after the first stage of compaction with water (Figure 2.2). Scanning electron microscopy of calcite powder after compaction indicate the presence of a large quantity of fractured particles with no evidence of interparticle bonding. This suggests that the densification process of this powder occurs through particle fracture and that the resulting large fragments are not cohesive enough to obtain a mechanically stable compact. As opposed to the lack of cohesion between calcite fragments, SEM images taken in our earlier study (Appendix B Figure B.1) [6] indicate that vaterite nanoparticles are always connected by necks after compaction. To explain the low strength of the partially crystallized ACC samples, X-ray diffraction and Fourier Transform Infrared spectroscopy were utilized to analyze possible changes in the crystalline structure of the partially crystallized ACC powder during compaction. The results confirm that the ACC powder continues to transform into calcite and vaterite during compaction with water and in air (Appendix B, Figure B.2 - Figure B.5).

Altogether, our densification experiments, structural analysis and mechanical stability assessment indicate that the nanovaterite is the only powder from the investigated calcium carbonates that undergoes water-assisted densification and sintering during uniaxial pressing while keeping its original crystallographic phase. A practical evidence of this cold densification and sintering process is the fact that the pressed vaterite specimens maintain their mechanical integrity even when stored for as long as 1 year in air.

The possible mass transport mechanisms underlying the water-assisted densification and sintering process were investigated by evaluating the effect of the initial pH and the temperature of the aqueous phase on the densification of the nanovaterite (Figure 2.3). Compaction tests at a target plateau stress of 500 MPa revealed that the water-assisted densification of vaterite nanoparticles is not affected by the initial pH of the aqueous medium (Figure 2.3a,c). The increase in relative density of the powder compact follows a similar profile during the two stages of the pressing procedure for pH values of 1, 2, 3 and 7 (Figure 2.3a). The comparable compaction behavior translated into a final relative density of 87-89% for all the specimens, regardless of the initial pH of the water phase. Although the actual pH of the aqueous phase will differ from its initial value due to the partial dissolution of the calcium carbonate particles in water, the marked effect of pH on the solubility of calcium carbonate allows us to obtain insights on the possible influence of dissolution processes on the cold sintering process. The solubility of calcite in water increases by seven orders of magnitude as the pH decreases from 7 to 1 (Figure 2.3c). In the absence of literature data, we assumed a similar change in solubility for vaterite particles. Due to the small size of the primary particles and corresponding short diffusion length, we assume that dissolution rather than diffusion is more likely to be the rate-limiting step if the densification process occurs via a pressure solution mechanism. In view of the strong dependence of the solubility on pH, our compaction results suggest that the dissolution of the calcium carbonate in the aqueous medium might not be the rate-limiting step in the densification process of the nanovaterite powder. In addition to the difficulty in quantifying the actual pH of the aqueous medium, it is also important to bear in mind though that the solubility data considered in our analysis are derived from thermodynamic quantities taken for calcite and thus may not represent the possible non-equilibrium conditions of our compaction experiments nor the local pH at the particle's surface.

In addition to pH, temperature is another control parameter that can be deliberately adjusted in our compaction experiments. Compaction of nanovaterite powder under controlled temperatures in the range $10 - 90\,°C$ reveal that the densification process in the first stage of the test is accelerated at higher temperatures (Figure 2.3b). This effect is opposite to what would be expected in a pressure solution mechanism, in which higher temperatures would decrease the solubility of calcium carbonate and thus slow down the densification process [26]. The relative density measured after the first stage increases from 78 to 86% as the temperature
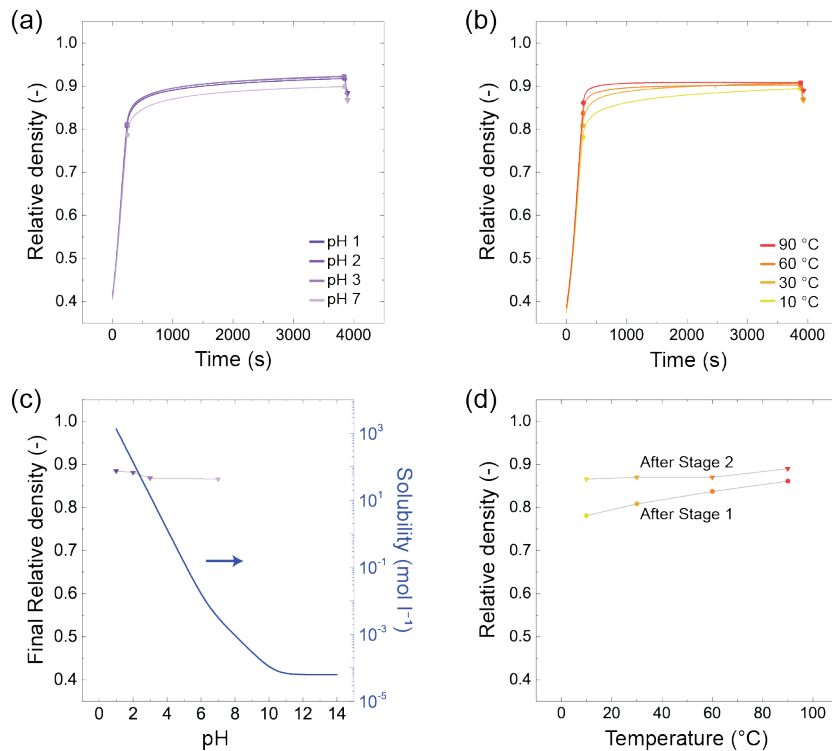
Figure 2.3: The effect of initial pH and temperature on the compaction of nanovaterite particles with water at 500 MPa for both stages 1 and 2. (a,b) Evolution of the relative density of the compact during pressing with water at different (a) pHs and (b) temperatures. (c,d) Final relative densities of the compacts as a function of (c) the initial pH and (d) the temperature of the aqueous phase.

is changed from 10 to 90 °C (Figure 2.3d). Eventually, the difference in relative density observed in this initial stage vanishes if the powders subjected to distinct temperatures are held long enough at high pressure in the second stage of the compaction procedure. This indicates a stronger densification in the second compaction stage for samples tested at lower temperatures. Such opposing effects of temperature on the densification behavior in the first and second stages probably arising from the several temperature-dependent parameters involved. Indeed, increasing the temperature from 10 to 90 °C decreases by twofold the solubility of calcium carbonate in water [13] while at the same time reducing the viscosity of the aqueous medium by a factor of about 4. Moreover, higher temperatures are expected to accelerate any thermally-activated mechanism at play during sintering, such as the diffusion of ions, the motion of dislocations and the rupture of ionic bonds.

Despite the opposing trends observed for tests performed at different temperatures, the results obtained from compaction tests at distinct pHs and temperatures indicate that the room-temperature densification and sintering of vaterite compacts under pressure does not seem to be controlled by a dissolution-diffusion-precipitation mechanism of mass transport close to the contact point between particles, as hypothesized in previous work on oxides [11].
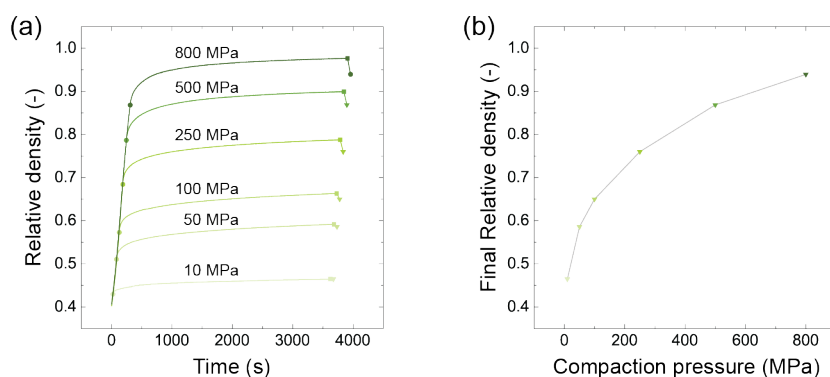
Figure 2.4: Compaction behavior of nanovaterite powders under different uniaxial pressures with water. (a) Evolution of the relative density during water-assisted compaction at different applied stresses. (b) Effect of the applied pressure on the final relative density of the nanovaterite compact.

Instead, other mechanisms must dominate the water-assisted densification of nanovaterite under pressure.

In contrast to the pH and temperature, the applied pressure markedly affects the densification of the nanovaterite powder with water (Figure 2.4). Powders compacted at an external pressure of 10 MPa reach a final relative density of only 46%, whereas those subjected to a pressure of 800 MPa achieve a remarkable final density of 94% after uniaxial compression. Because of the relatively high pressures applied, elastic recovery is observed upon mechanical unloading of the specimens (Figure 2.4a). As expected, the extent of elastic recovery increases for higher levels of external pressure. Overall, the final relative density obtained after the compaction process was observed to increase monotonically with the externally applied pressure (Figure 2.4b).

To better understand the effect of the applied pressure on the water-assisted densification process, we thoroughly analyzed the response of the vaterite powder in the first and second stages of the compaction procedure (Figure 2.5). In the first stage, the densification process resembles the typical pattern observed during the compact of powders at a constant displacement rate (Figure 2.5a,b) [27, 28]. At low applied stresses, only a mild increase in relative density is observed due to mostly particle re-arrangement within the compact. Higher pressures significantly increase the stresses at the contact point between particles, resulting in strong shrinkage and densification.

In an attempt to interpret this compaction behavior during stage 1, we revisit empirical analytical models previously reported in the literature to correlate the macroscopic stress with the actual volume fraction of solids in load-bearing particle systems. In colloidal networks of attractive particles, the macroscopic yield stress (τ) under shear often follows a power law dependence on the volume fraction of particles (ϕ): $\tau_y \sim \phi^\gamma$, with the exponent γ typically varying between 1.4 and 5.5 [29]. For networks containing fractal-like aggregates, a high γ
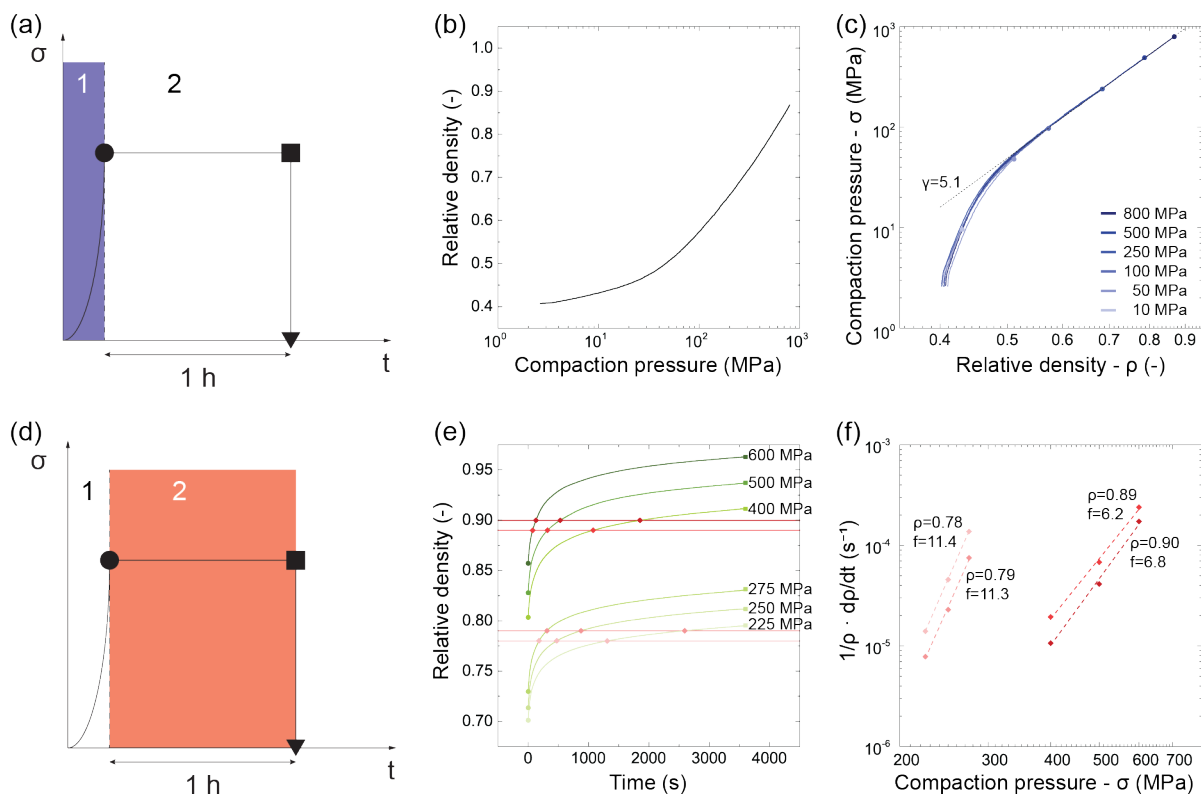
Figure 2.5: Densification and creep behavior of nanovaterite powders during uniaxial compaction with water. (a,d) Schematics of the stress pattern applied during (a) stage 1 and (d) stage 2 of the compaction process. (b) Relative density of the nanovaterite compacts at the end of the first stage for different applied pressure levels. (c) Correlation between the applied stress and the relative density in stage 1, indicating the power law dependence observed at high densities. (e) Creep behavior of vaterite compacts subjected to different stress levels in stage 2. (f) Creep strain rate as a function of the applied stress for vaterite specimens with distinct relative densities.

exponent is associated with denser and more compact aggregated microstructures. Given the microstructural similarities between such colloidal networks and the powder compacts studied here, we re-plot our experimental data in a double logarithmic chart that correlates the applied macroscopic compressive stress (σ) with the actual relative density of the compact (ρ). Interestingly, the dependence of σ on ρ at high applied stresses can also be described by a power law scaling relation (Figure 2.5c). A power law exponent of 5 was derived by fitting this scaling relation to the data obtained at high compressive stresses. While additional experiments are required to further explore this analogy between the mechanical response of colloidal networks and powder compacts, our analysis suggests that the densification of the nanovaterite powder might occur through the local rupture of contact points between particles in a similar way to the attractive interparticle bonds in colloidal gels.

Besides its practical relevance, the strong effect of the applied pressure on the compaction of the nanovaterite powder can also provide further insights into the microscopic mechanisms that control the water-assisted densification process. This is possible by examining the

influence of the applied stress on the second stage of the compaction procedure (Figure 2.5d-f). In this stage, the creep behavior of the compact is evaluated by tracking the increase in relative density of the sample while it is subjected to a constant external pressure. The compact exhibits a typical creep behavior with the speed of densification being highest at the beginning of the test and continuously decreasing within our 30 min timeframe. The experimental results show that a gain in relative density of the compact between 9 and 11% is obtained when pressures in the range of 225-600 MPa are applied for 1 hour.

The dependence of the creep rate on the applied stress provides information about the possible mechanisms underlying the densification process. The strain rate during creep, $\dot{\varepsilon}$, usually follows a power law relation with the applied stress, σ, such that: $\dot{\varepsilon} \sim \sigma^f$ [30]. In this scaling relation, f is a stress exponent that depends on the mechanism that dominates the densification process. Densification resulting from the diffusion of atoms via the bulk lattice, the grain boundaries or through viscous flow lead to a weak stress dependence with $f = 1$ [28]. By contrast, densification mechanisms involving dislocation motion (plastic deformation) give rise to a strong stress dependence with f values ranging from 3 to 5 [28, 31, 32].

To shed light on the possible densification mechanisms at play during the compaction of the vaterite nanopowder, we estimate the stress exponents from the creep data obtained at different applied stresses (Figure 2.5e). Because the creep rate depends on the actual relative density of the compact [30], the effect of the applied stress on the normalized densification speed is quantified by comparing data from samples with the same relative density. Using this approach, the initial density of the samples at the beginning of the stage 2 differ by only ±3%, a value considered to be sufficiently low in geological studies to ensure a similar initial microstructure and thus contact area in the creep experiments [33]. Strain rate data for the selected relative densities of 0.78, 0.79, 0.89 and 0.90 were obtained from measurements conducted at external uniaxial pressures between 225 and 600 (Figure 2.5f).

The experimental results show stress exponents (f) of approximately 6 and 11 for the high and low relative densities/pressures ranges, respectively. A similar stress exponent is obtained if the strain rate data is depicted as a function of the normalized porosity, as is typically the case in geological studies (Appendix B Figure B.6). This strong stress dependence of the creep rate provides further experimental evidence that diffusion processes involving dissolution-precipitation or mass transport via lattice, grain boundary and viscous flow mechanisms ($f = 1$) may not be the rate-limiting steps in the water-assisted densification of the nanovaterite powders used in this study. Instead, high stress exponents are typically observed in calcite samples when the creep response is dominated by strain hardening or fracture mechanisms.

Strain hardening resulting from the pile-up of dislocations at grain boundaries have been proposed to explain the creep response of calcite at high temperatures [14]. This mechanism leads to apparent stress exponents varying from 4.5 to 8 in synthetic calcite specimens tested

between 600 and 800 °C using differential pressures up to 100 MPa [14]. Dislocation pile-up and crystal twinning have also been observed in geological limestone pressed under differential stresses up to 300 MPa at room temperature if samples are subjected to a confining pressure during triaxial compaction [15]. When a power law model is used to interpret these room-temperature tests, the creep rate of such geological samples was found to follow a similar stress dependence as that of the synthetic calcite specimens measured above 600 °C (f = 4.5) [14, 15]. In comparison to these synthetic and geological calcite samples, our nanovaterite compacts exhibit significantly smaller grain/particle sizes and were subjected to higher stress levels under uniaxial compaction.

As an alternative to dislocation-based mechanisms, the deformation of the nanovaterite compacts under pressure might also be controlled by so-called brittle creep [32]. In this creep mechanism, macroscopic deformation under a constant mechanical load results from microcracking and microfracture events at sites where the externally applied stresses are locally amplified. The resulting cracks increase the compliance of the structure, allowing for macroscopic deformation and further densification of the compact. Although this mechanism is often times only dominant when the external mechanical stress lies close to the fracture strength of the structure, the presence of water within the compact can greatly facilitate the local rupture of bonds and thus reduce the stresses required for the onset of brittle creep [16, 34]. This water-assisted fracture mechanism results from the well-known phenomenon of subcritical crack growth. In such interpretation, the necks initially formed between sintered nanoparticles are fractured via water-assisted subcritical crack growth, allowing for the sliding and rearrangement of the nanoparticles into denser compacts that are subsequently strengthened through interparticle bonds arising from newly formed necks. Importantly, the high number density of such interparticle necks in the vaterite specimens is expected to be crucial for the formation of compacts with high mechanical strength after densification.

In spite of the available literature on the densification process of geological calcite, the different grain sizes and crystalline structures of our nanovaterite compacts make it difficult to draw conclusions based on the experimental results obtained in this work. Therefore, further studies are needed to evaluate the effect of strain hardening and subcritical crack growth on the creep behavior of nanovaterite compacts and thus improve our understanding of the water-assisted densification process.

2.4. Conclusions

Calcium carbonate powders in the form of vaterite can be strongly densified by uniaxial pressing with water. The lower density and lack of structural integrity of powders pressed in air confirms the importance of water in the cold compaction process. On the basis of

compaction experiments carried out under highly solubilizing acidic conditions, we infer that dissolution-precipitation mechanisms might not control the observed densification effect. Densification during mechanical loading at constant displacement rate was found to be stronger at higher temperatures, suggesting that cold compaction is governed by a thermally-activated process. From all the investigated processing parameters, the applied pressure shows the strongest effect on the final relative density of nanovaterite compacts. Pronounced densification under pressure occurs both during constant displacement rate as well as under creep conditions. The relation between the relative density and the applied stresses under constant displacement rate follows a similar behavior to that expected for percolating networks of interconnected particles. Under creep conditions, the normalized densification rate depends on the applied stress following a power law with stress exponents higher than 6. The strong stress dependence of the creep rate suggests strain hardening or fracture via water-accelerated subcritical crack growth as possible mechanisms responsible for the densification of vaterite nanopowders during uniaxial pressing. Further studies are required to identify the mechanism at play and possibly exploit it for the cold compaction of other nanoparticle systems.

Acknowledgements

References

[1]   J. Geyssant, Geology of calcium carbonate, in: F.W. Tegethoff (Ed.), Calcium Carbonate - From the cretaceous period into the 21st century, Birkhäuser, Basel; Boston; Berlin, 2001.

[2]   D. Gebauer, A. Völkel, H. Cölfen, Stable prenucleation calcium carbonate clusters, Science 322(5909) (2008) 1819-1822.

[3]   A. Sanna, M. Uibu, G. Caramanna, R. Kuusik, M.M. Maroto-Valer, A review of mineral carbonation technologies to sequester CO2, Chem. Soc. Rev. 43(23) (2014) 8049-8080.

[4]   X. Lim, How to make the most of carbon dioxide, Nature News 526(7575) (2015) 628.

[5]   S. Colman, D. Dethier, Rates of Chemical Weathering of Rocks and Minerals, Academic
       Press1986.

[6]   F. Bouville, A.R. Studart, Geologically-inspired strong bulk ceramics made with water at
       room temperature, Nat. Commun. 8 (2017) 14655.

[7]   B.V. Parakhonskiy, A. Haase, R. Antolini, Sub-Micrometer Vaterite Containers: Synthesis,
       Substance Loading, and Release, Angew. Chem. Int. Ed. 51(5) (2012) 1195-1197.

[8]   H. Kähäri, M. Teirikangas, J. Juuti, H. Jantunen, Dielectric Properties of Lithium Molybdate
       Ceramic Fabricated at Room Temperature, J. Am. Ceram. Soc. 97(11) (2014) 3378-3379.

[9]   H. Kähäri, M. Teirikangas, J. Juuti, H. Jantunen, Improvements and Modifications to
       Room-Temperature Fabrication Method for Dielectric Li2MoO4 Ceramics, J. Am. Ceram.
       Soc. 98(3) (2015) 687-689.

[10]   B. Dargatz, J. Gonzalez-Julian, O. Guillon, Improved compaction of ZnO nano-powder
       triggered by the presence of acetate and its effect on sintering, Sci. Technol. Adv. Mater.
       16(2) (2015) 025008.

[11]   J. Guo, H. Guo, A.L. Baker, M.T. Lanagan, E.R. Kupp, G.L. Messing, C.A. Randall, Cold
       Sintering: A Paradigm Shift for Processing and Integration of Ceramics, Angew. Chem. Int.
       Ed. 55(38) (2016) 11457-11461.

[12]   J.-P. Gratier, D.K. Dyshe, F. Renard, Chapter 2 - The Role of Pressure Solution Creep in the
       Ductility of the Earth's Upper Crust, Adv Geophys 54 (2013) 47-179.

[13]   L.N. Plummer, E. Busenberg, The solubilities of calcite, aragonite and vaterite in CO2-H2O
       solutions between 0 and 90 C, and an evaluation of the aqueous model for the system
       CaCO3-CO2-H2O, Geochim. Cosmochim. Acta 46(6) (1982) 1011-1040.

[14]   J. Renner, B. Evans, G. Siddiqi, Dislocation creep of calcite, J. Geophys. Res. 107(B12)
       (2002) 2364.

[15]   A. Nicolas, J. Fortin, J.B. Regnet, B.A. Verberne, O. Plümper, A. Dimanov, C.J. Spiers, G. Y.,
       Brittle and semibrittle creep of Tavel limestone deformed at room temperature, J.
       Geophys. Res. Solid Earth 122(6) (2017) 4436-4459.

[16]   A. Voigtländer, K. Leith, M. Krautblatter, Subcritical crack growth and progressive failure
       in Carrara marble under wet and dry conditions, J. Geophys. Res. Solid Earth 123(5)
       (2018) 3780-3798.

[17] J. Gonzalez-Julian, K. Neuhaus, M. Bernemann, P.J. da Silva, A. Laptev, M. Bram, O. Guillon, Unveiling the mechanisms of cold sintering of ZnO at 250 °C by varying applied stress and characterizing grain boundaries by Kelvin Probe Force Microscopy, Acta Mater. 144 (2018) 116-128.

[18] Y. Nara, K. Kashiwaya, Y. Nishida, T. Ii, Influence of surrounding environment on subcritical crack growth in marble, Tectonophysics 706 (2017) 116-128.

[19] B.K. Atkinson, Subcritical crack growth in geological materials, J. Geophys. Res. Solid Earth 89(B6) (1984) 4077-4114.

[20] B.K. Atkinson, Subcritical crack propagation in rocks: theory, experimental results and applications, J. Struct. Geol. 4(1) (1982) 41-56.

[21] N. Brantut, M.J. Heap, P. Baud, P.G. Meredith, Mechanisms of time-dependent deformation in porous limestone, J. Geophys. Res. Solid Earth 119(7) (2014) 5444-5463.

[22] J.T. Avaro, C. Ruiz-Agudo, E. Landwehr, K. Hauser, D. Gebauer, Impurity-free amorphous calcium carbonate, a preferential material for pharmaceutical and medical applications, Eur. J. Mineral. 31(2) (2019) 231–236.

[23] J.W. Anthony, R.A. Bideaux, K.W. Bladh, M.C. Nichols, Handbook of Mineralogy, Mineralogical Society of America, Chantilly, VA 20151-1110, USA.

[24] W.M. Haynes, D.R. Lide, T.J. Bruno, CRC handbook of chemistry and physics: a ready-reference book of chemical and physical data., 97 ed., CRC Press, Boca Raton, Florida, USA, 2016.

[25] H. Cölfen, A. Völkel, Application of the Density Variation Methodon Calciumcarbonate Nanoparticles, Springer, Berlin, Heidelberg, 2006, pp. 126-128.

[26] E. Liteanu, A. Niemeijer, C.J. Spiers, C.J. Peach, J.H.P. de Bresser, The effect of CO2 on creep of wet calcite aggregates, J. Geophys. Res. Solid Earth 117(B3) (2012).

[27] R.G. Frey, J.W. Halloran, Compaction Behavior of Spray Dried Alumina, J. Am. Ceram. Soc. 67(3) (1984) 199-203.

[28] M.N. Rahaman, Ceramic Processing and Sintering, 2 ed., CRC Press2003.

[29] A.R. Studart, E. Amstad, L.J. Gauckler, Yielding of weakly attractive nanoparticle networks, SOFT MATTER 7(14) (2011) 6408-6412.

[30] G. Antou, P. Guyot, N. Pradeilles, M. Vandenhende, A. Maître, Identification of densification mechanisms of pressure-assisted sintering: application to hot pressing and spark plasma sintering of alumina, J. Mater. Sci. 50(5) (2015) 2327-2336.

[31] A.H. Chokshi, T.G. Langdon, Characteristics of creep deformation in ceramics, Mater. Sci. Technol. 7(7) (1991) 577-584.

[32] A. Hynes, R. Doremus, Theories of creep in ceramics, CRIT REV SOLID STATE 21(2) (1996) 129-187.

[33] A.M.H. Pluymakers, C.J. Peach, C.J. Spiers, Diagenetic compaction experiments on simulated anhydrite fault gouge under static conditions, J. Geophys. Res. Solid Earth 119(5) (2014) 4123-4148.

[34] S.M. Wiederhorn, L.H. Bolz, Stress corrosion and static fatigue of glass, J. Am. Ceram. Soc. 53(10) (1970) 543-548.

Chapter 3: Uniaxial Pressing of Zinc Oxide and Hydroxyapatite Powders

Abstract

Room-temperature cold sintering is a new method by which calcium carbonate can be compacted into dense structures with specific mechanical properties 10 times better than cementitious materials. Possible mechanisms for this sintering behavior include plastic deformation or subcritical crack growth facilitated by water. So far, this process was exclusively investigated for the different polymorphs of $CaCO_3$ and works only for micron-sized agglomerates of vaterite nanoparticles — one of the carbonate's metastable forms. Here, we investigate the compaction behavior of zinc oxide (ZnO) and hydroxyapatite (HA) powders under uniaxial pressing and compare their response to that observed for nanovaterite. ZnO can be synthesized in hierarchical agglomerates with a similar size as the nanovaterite particles. HA not only presents a structure made of agglomerated nanoparticles agglomerates but also forms crystalline precipitates in water at room temperature, similar to nanovaterite. We found that room-temperature cold sintering seems to be a very specific process to nanovaterite, since ZnO and HA cannot be densified to the levels reached by nanovaterite when subjected to uniaxial pressing with water.

3.1. Introduction

Cold sintering and especially room-temperature cold sintering has the potential to make the ceramics industry more environmental friendly, because the temperatures involved in this new process are significantly lower than in traditional sintering and could potentially save up to 90% of the energy used during manufacturing [1-3]. Currently, researchers are expanding the portfolio of materials that are accessible by this process. While a broad range of materials has already been shown to cold sinter at temperatures between 80 and 250 °C [2, 4-6], room-temperature cold sintering of sparsely soluble materials seems to be exclusive to nanovaterite, one specific polymorph of calcium carbonate [1]. Nanovaterite shows significant densification at room temperature under pressures between 10 and 800 MPa and in the presence of water, despite its orders of magnitude lower solubility in water compared for example with NaCl.

Two materials previously reported that show substantial densification at low temperature are hydroxyapatite ($Ca_5(PO_4)_3(OH)$, HA) [4] and zinc oxide (ZnO) [5]. Grossin *et al.* [4] reported an unusual high density of HA when processed in spark plasma sintering oven (SPS) at 100 MPa and at 150 °C. They concluded that the high mobility of ions in a hydrated layer on the surface of the nanoparticles might be responsible for the densification behavior. Furthermore, the low temperatures involved are essential to maintain this hydrated layer. Dargatz *et al.* [5] published a paper about the densification of ZnO nanoparticles at temperatures as low as 85 °C and under stresses up to 50 MPa. Thanks to their cold densification process, they were able to maintain

a small grain size during the process, while reaching a relatively high density of 89%. Additionally, because ZnO is used in electronic and optoelectronic systems and HA for bone tissue engineering, sintering these powders close to room temperature would enable faster and less energy-demanding manufacturing of polymer-ceramic composites for these applications.

In the previous chapter, we investigated the influence of process parameters such as pH of the aqueous medium, temperature and pressure on the room-temperature cold sintering of nanovaterite and discussed possible mechanisms underlying this process [7]. We found that pressure has the strongest effect on the cold sintering process for nanovaterite and that plastic deformation or subcritical crack growth are two possible mechanisms responsible for the room-temperature cold sintering phenomenon. However, we still do not completely understand why nanovaterite densifies at such low temperatures. One possible explanation for the room temperature cold sintering mechanism is as follows: the starting material should form agglomerates, within which nanoparticles form necks between each other. Agglomerates of highly packed nanoparticles leads to a large density of contact points (necks) between nanoparticles, thus increasing the mechanical properties of the compact. When pressure is applied in the presence of water, the necks can be fractured by a water-assisted fracture mechanism, known as subcritical crack growth, allowing sliding and rearrangement of the nanoparticles in a denser compact. Because of the ability of the material to crystalize in water at ambient temperature, new necks between the nanoparticles can be formed again, which ultimately gives the mechanical strength of the compact [7].

In this chapter, we apply the strategies for room-temperature cold sintering of nanovaterite to zinc oxide (ZnO) and hydroxyapatite (HA). Room-temperature cold sintering of materials, which are not readily soluble in water is exclusively observed for nanovaterite. However, there is no synthetic route known to obtain vaterite in a different powder morphology, preventing us from investigating in more detail the effect of this physical parameter alone. Therefore, we investigated different materials exhibiting a similar hierarchical powder morphology. We hypothesize that this hierarchical microstructure is sufficient to lower the sintering temperature for ZnO and HA to room temperature, as it provides a combination of nanometric particle size while increasing the number of contact points between the particles compared to a loose assembly of nanoparticles. Additionally, HA can precipitate in crystalline form at room temperature in water, similarly to the nanovaterite. This is however not the case for ZnO particles. Such difference in the precipitation behavior allows us to also investigate the role of the crystallinity of the material precipitated at the grain boundary on the mechanical properties of the pressed compacts.

3.2. Materials and Methods

3.2.1. Synthesis of Nanovaterite Particles

Nanovaterite particles were prepared according to a method published by Parakhonskiy *et al.* [8]. Briefly, aqueous solution of calcium chloride dihydrate (CaCl$_2$·2H$_2$O, Merck, Germany) and sodium carbonate (Na$_2$CO$_3$, Aldrich, Germany) were prepared, each with a concentration of 2 mol L^{-1}. 16 mL of each solution was separately mixed with 80 mL ethylene glycol (technical, VWR, France) resulting in a final salt concentration of 0.36 mol L^{-1}. The Na$_2$CO$_3$ solution was rapidly added to the CaCl$_2$·2H$_2$O solution and stirred vigorously for one hour. The precipitates were removed from the suspension by centrifugation at 4500 rpm for 15 min. The agglomerates were then washed twice with ethanol (94% denaturated with toluene, Alcosuisse) before they were dried in an oven at 60 °C overnight and at 120 °C for another day. The morphology of the particles was analyzed with a scanning electron microscope (SEM, LEO1530, Zeiss, Germany). The images were acquired using a secondary electron detector operated at a 2 kV acceleration voltage. Prior to obtaining the images, the sample was coated with a 5 nm layer of Pt in order to make the surface electrically conductive. The size of the agglomerates and of the primary particles were measured from SEM images.

3.2.2. Synthesis of ZnO Particles

To prepare ZnO nanoparticles, 40 g of zinc acetate (Zn(ac), puriss., Sigma Aldrich, Germany) were added to 200 mL diethylene glycol (DEG, 98%, Acros, USA) in a round bottom flask and immersed in a preheated oil bath at 190 °C. The powder fully dissolved and the solution became clear as soon as the temperature of the solvent reached 154 °C. The solution then became turbid as it reached a temperature of 170 °C, a sign of the nucleation of the ZnO nanoparticles. The reaction was stopped after 30 min, the flask was removed from the oil bath and the solution let to cool down to ambient temperature. The suspended product was collected by filtering, washed with 100 mL of ethanol, and dried under vacuum at 1 mbar for 24 h. The morphology and the particle size of the agglomerates were analyzed with an SEM. The same SEM settings as described above were used. The synthetic method was adapted from Kränzlin *et al.* [9, 10].

3.2.3. Synthesis of Hydroxyapatite Platelets

Hydroxyapatite (Ca$_5$(PO$_4$)$_3$(OH), HA) platelets were synthesized combining two protocols published by Jha *et al.* and Silva *et al.* [11, 12]. Typically, 200 mL of an aqueous solution with

0.5 mol L^{-1} ammonium hydrogen phosphate ($(NH_4)_2HPO_4$, puriss., Sigma Aldrich, Geramany) was added dropwise to 240 mL of an aqueous solution with 0.5 mol L^{-1} calcium nitrate ($Ca(NO_3)_2$, Sigma Aldrich, Germany). The solution of precipitates was stirred for 1 h at room temperature before the platelets were removed from the suspension by vacuum filtration. The platelets were then washed twice with deionized (DI) water. The white particles were then redispersed in 400 mL of an aqueous solution of sodium hydroxide (1 mol L^{-1}, NaOH, VWR, USA) and stirred for 20 h. The platelets were sedimented, the excess basic solution was decanted and the remaining precipitates were washed three times with 1 L of DI water to remove the remaining ions. After the third washing step, 300 mL DI water were added and the suspension was frozen in a liquid nitrogen bath under constant stirring to avoid sedimentation. The frozen suspension was then freeze dried. The morphology and the particle size of the obtained powder was analyzed with the SEM as described above.

3.2.4. Compaction Experiments

Typically, 0.3 g of HA particles or 0.6 g of the ZnO particles were mixed with 0.75 mL of DI water before placing the resulting water-powder mixture in a pressing tool. To avoid the powder from sticking to the pressing tool, a round polyimide (Kapton) film was placed at the bottom and on the top of the powder in the pressing tool. The pressing tool was placed in a mechanical testing machine for uniaxial pressing (Instron 8562, Instron, equipped with a 100 kN lead cell). The load was increased with a displacement rate of 0.5 mm min^{-1} until the target force was reached, at which point the machine switched to load-controlled mode and the displacement was automatically adjusted to maintain the target pressure. The compliance of the machine and of the pressing tool with the polyimide films was deducted from the measurement by recording a correction curve. From the correction data, we calculated a spring constant for the set up: $K_{machine}$. The displacement was corrected with the following formula: $\Delta L_{powder}(F) = \Delta L_{measured} - K_{machine}F$, where ΔL_{powder} is the displacement from the powder only, $\Delta L_{measured}$ is the total displacement measured with the machine and F is the applied force. We used the following density values for the calculation of the relative densities: 2.54 g cm^{-3} for vaterite, 3.16 g cm^{-3} for HA and 5.61 g cm^{-3} for ZnO.

For the experiments at elevated temperatures, we mounted a cylindrical heating element on the pressing tool. The temperature reported was measured at the heating element. These experiments were conducted on a simple hydraulic hand press, in which the displacement was manually adjusted to keep a constant force. The sample was pressed for 30 min.

3.3. Results and Discussion

We investigated the compaction of zinc oxide (ZnO) and hydroxyapatite ($Ca_5(PO_4)_3(OH)$, HA) particles in the presence of water to understand if the hierarchical morphology or the ability of a material to crystalize at room temperature in water are important requirements for the cold sintering process. Table 3.1 summarizes the difference and similarities between these two materials relative to nanovaterite powder. ZnO particles precipitated at 170 °C in diethylene glycol present a morphology similar to the nanovaterite. Nanovaterite particles were synthesized in the form of spherical agglomerates with a diameter of 500 nm to 1 μm consisting of spherical primary particles with a diameter of 40 to 60 nm (Figure 3.1). The ZnO agglomerates are 50% smaller with a diameter of 200-600 nm and primary particles two times smaller with a diameter of 10 to 20 nm (Appendix C Figure C.1). Additionally, nanovaterite is also only twice as soluble in water as ZnO [13, 14] (Table 3.1). However, ZnO has a shear modulus 30% higher and a bulk modulus twice as high as nanovaterite and cannot form crystalline precipitates at room temperature [9].

Table 3.1: Comparison between the different materials investigated in this study. ZnO can be produced in a similar morphology as the nanovaterite particles. HA can be produced by biomineralization, precipitates in crystalline form at room temperature, and it contains the same cation as nanovaterite. The elastic constants are obtained from the material project database [15] and the solubility from values reported in the literature [13, 14, 16].

|	Zinc oxide	Nanovaterite	Hydroxyapatite
	ZnO	$CaCO_3$	$Ca_5(PO_4)_3(OH)$
Cation	Zn^{2+}	Ca^{2+}	Ca^{2+}
Anion	O^{2-}	CO_3^{2-}	PO_4^{3-} and OH^-
Morphology	Round agglomerates	Round agglomerates	Platelets
Agglomerates size	200-600 nm	500-1000 nm	5-20 μm
Primary particle size	10-20 nm	40-60 nm	30-60 nm
Bulk modulus	130 GPa	70 GPa	100 GPa
Shear modulus	40 GPa	30 GPa	60 GPa
Solubility	1-6 mg L^{-1}	11 mg L^{-1}	0.031 mg L^{-1}
Biomineralization?	No	Yes	Yes
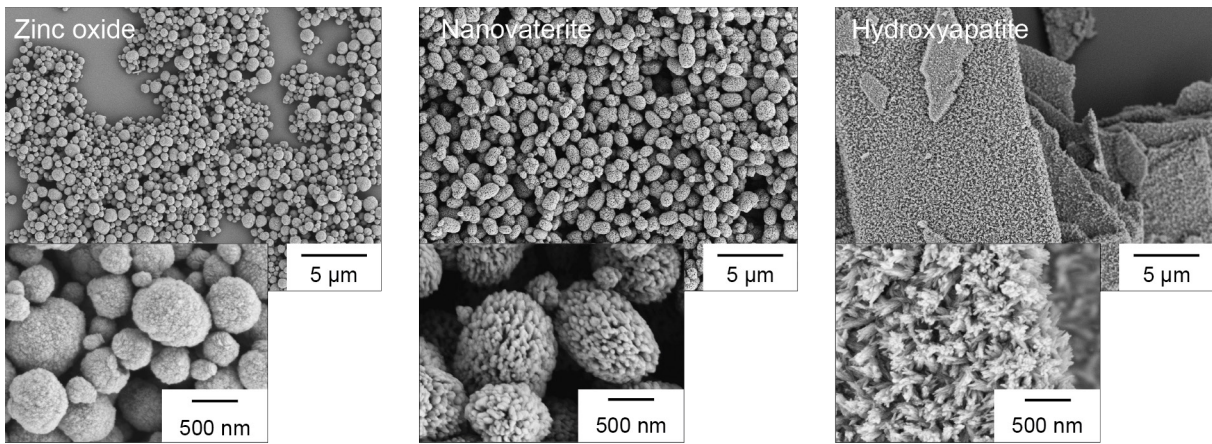
Figure 3.1: SEM micrographs show the morphology of the three materials.

By contrast, HA can be produced through biomineralization and forms crystalline precipitates at room temperature [11, 12, 17] as well as contains the same cation as nanovaterite. HA can be synthesized in platelet shape agglomerates of diameter of 5 to 20 µm and thickness of 200 to 500 nm. Such platelets are 10 times larger than the round agglomerates of nanovaterite or ZnO. However, they still contain primary nanoparticles of diameter comprising between 30 to 60 nm, a size comparable to the primary particles of nanovaterite. The solubility of HA, however, is three orders of magnitude smaller than from nanovaterite [16]. The shear modulus of HA is also two times higher than the one of the nanovaterite. The elastic constant of ZnO and HA are based on estimations from machine learning algorithms based on Discreet Fourier Transform (DFT) calculation and should thus be treated as approximations [15].
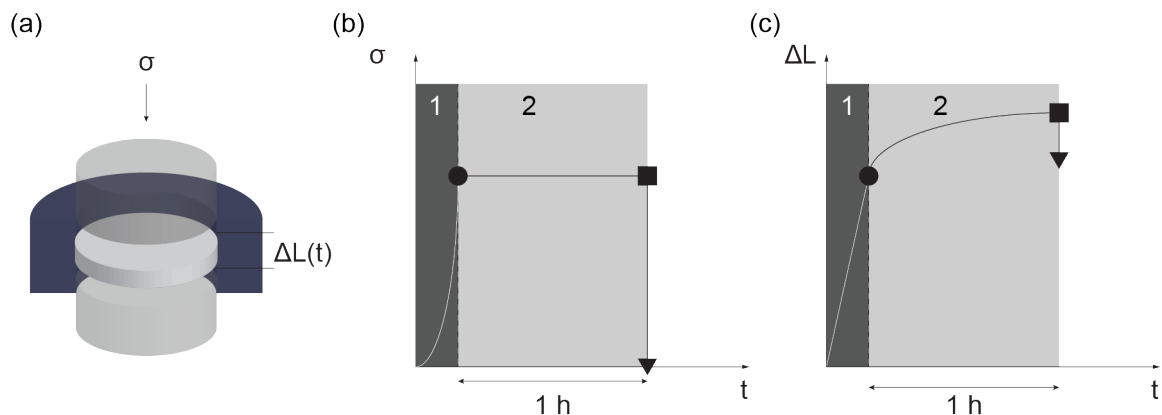
Figure 3.2: Schematic of the cold sintering process. *During the cold sintering process, constant pressure is applied on the sample over a time period up to 1 h, during which we record the vertical contraction of the sample. The densification process can be monitored in situ in a mechanical testing machine. During stage 1 (dark grey) the displacement is increased linearly to reach the targeted force while during stage 2 (light grey) the displacement is constantly adjusted to keep the same applied pressure.*

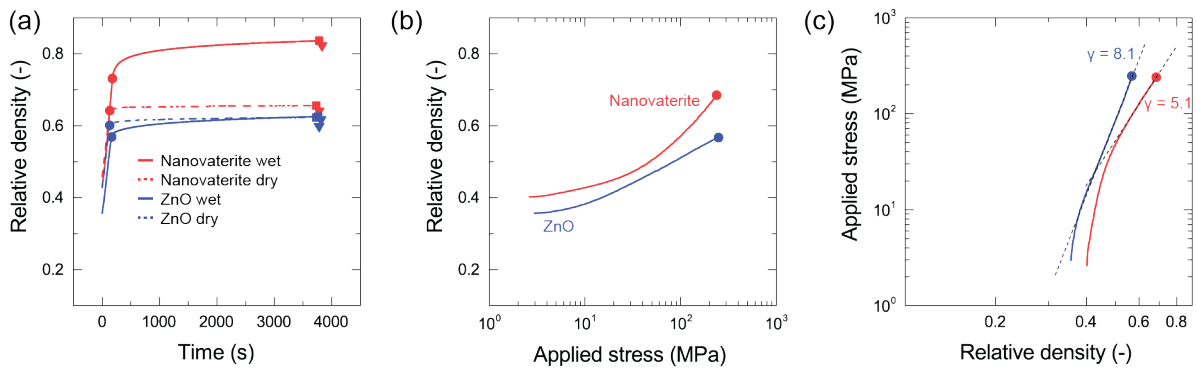*Figure 3.3: Room temperature densification of ZnO compared to reference CaCO₃ powder.* (a) *Relative density as a function of time during compaction in both stages at a pressure of 250 MPa for both nanovaterite and ZnO agglomerates. (b) Stage 1 of the compaction process for the ZnO and nanovaterite agglomerates, both pressed with water. (c) Relative density as function of applied stress for ZnO and nanovaterite.*

The cold sintering behavior of these two materials was investigated by measuring the densification *in situ* with a mechanical tester. In these tests, the stress applied on the powder is increased with a constant displacement rate (Figure 3.2b,c, stage 1). Once the targeted stress level is reached, the machine is programmed to maintain that stress level by adjusting the displacement (Figure 3.2b,c, stage 2). The density of the powder compact was then calculated at each time step using the corrected displacement data.

3.3.1. Uniaxial Pressing of Zinc Oxide

The densification behavior of the ZnO agglomerates differs significantly from that observed for the nanovaterite (Figure 3.3a). Compaction tests were first performed on zinc oxide (ZnO) particles at an applied stress of 250 MPa at room temperature. Over the entire course of the experiment, the relative density of the ZnO remains lower than of the nanovaterite in similar conditions. The difference in density between the ZnO particles pressed with and without water is significantly smaller than for the nanovaterite agglomerates. When pressed with water, nanovaterite particles reach a final density of 82%, which is 20% higher than pressed dry. ZnO reaches a density of 62% and 59% when subjected to the same stress level as the nanovaterite powder with and without water, respectively.

The relative density of both, nanovaterite and ZnO, increases slowly at low applied stress (Figure 3.3b) probably due to particle rearrangement. At higher applied stress, the relative density of the nanovaterite increases at a faster rate than the ZnO particles.

Another interesting experimental observation is that the ZnO samples typically disintegrate into powder when removed from the pressing mold. For this reason, the mechanical properties of pressed ZnO samples could not be reported here.

During stage 2 of the compaction process, we observe an increase in relative density for the nanovaterite powder from 73% to 83%, whereas the same powder pressed without water only increases from 64% to 65%. The relative density of ZnO pressed with water increases from 57% to 63%, which is 4% more than when pressed without water (60% to 62%). Since the final does not change, we can conclude that no densification is taking place. The observed change in the kinetics during stage 2 could originate from the excess water being squeeze out of the powder compact similar to a sponge being pressed. This effect of water being expelled is also present in the nanovaterite samples, but we cannot discriminate this phenomenon from the densification.

We applied the analytical model described in the previous study to the ZnO compacts as well (chapter 2.3.). To use this model, we again assume that the morphology of the ZnO particles and the nanovaterite particles is similar to the microstructure of a colloidal network of attractive particles. The densification during stage 1 in the double logarithmic chart relative density versus applied stress is displayed in Figure 3.3c. In such colloidal networks, the macroscopic yield stress (τ_y) under shear can be described as a power law dependence on the volume fraction of the particles (ϕ): $\tau_y \sim \phi^\gamma$ with the exponent γ typically between 1.4 and 5.5 [18]. Larger exponents correspond to denser and more compact colloidal networks. The power law exponent (γ) calculated for the ZnO particles is 8 and therefore significantly higher than the value of 5 obtained for the nanovaterite. From these results and under the assumptions mentioned above, we can conclude that the nanoparticles within an ZnO agglomerate are more densely packed compared to those in the nanovaterite counterparts. This higher packing density might make the agglomerates too strong and difficult to break during the compaction process, therefore limiting the densification of this oxide material.

Despite a similar particle morphology, shear modulus, and relatively close solubility in water, room-temperature cold sintering of ZnO in the presence of water does not lead to the same results as with nanovaterite. Thus, we have chosen to investigate hydroxyapatite (HA, $Ca_5(PO_4)_3(OH)$), as a material that also displays a hierarchical powder structure and that can be precipitate in crystalline form at room temperature, similarly to $CaCO_3$.

3.3.2. Uniaxial Pressing of Hydroxyapatite

The compaction behavior of hydroxyapatite (HA) with water was investigated with the same methods as with the ZnO powder. HA particles present a similar hierarchical organization as that of the other powders, with needle-shaped nanoparticles assembled into micron-sized agglomerates. However, both the size and morphology of HA agglomerates differ significantly from the spherical ones of ZnO and nanovaterite. HA platelets present a diameter of 5-20 μm and thickness in the range 200-500 nm. The densification curves of the HA agglomerates in the
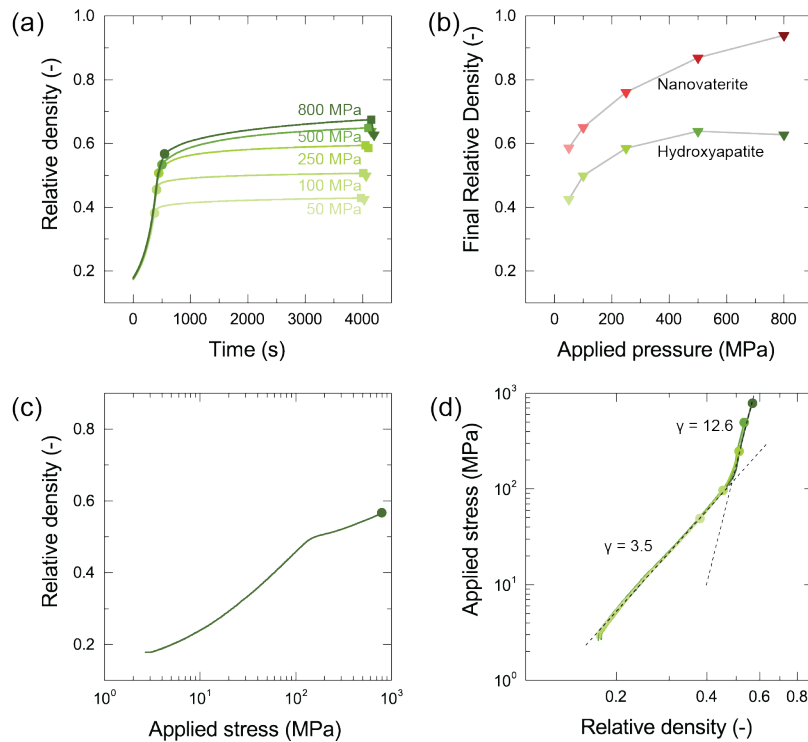
Figure 3.4: Room-temperature uniaxial pressing of HA (Ca₅(PO₄)₃(OH)) compared to reference CaCO₃ (vaterite) samples. (a) Densification curves of HA pressed with water recorded at increasing pressures from 50 to 800 MPa. (b) Relative density obtained at the end of stage 2 as a function of the pressure applied for HA and nanovaterite. (c) Relative density as a function of the applied stress during stage 1 for HA agglomerates at pressures up to 800 MPa. (d) Applied stress as a function of the relative density with fitting lines used to extract the exponent γ.

presence of water at pressure varying from 50 to 800 MPa are plotted in Figure 3.4a. Similar to nanovaterite, we observe a densification during stage 2, in which the relative density increases between 5% and 11% from the end of stage 1.

The final relative density measured after subtracting the elastic rebound increases from 42% to 63% when the pressure is increased from 50 MPa to 800 MPa (Figure 3.4b). The relative density increases with pressure gradually and saturates at higher stress levels, with 8% net increase when the pressure is increased from 50 to 100 MPa, eventually reaching 63% when the pressure is further increased from 500 to 800 MPa. The relative density of nanovaterite on the other hand continues to increase with increasing pressure, reaching 92% at 800 MPa (Figure 3.4b). Additionally, HA samples pressed at 500 and 800 MPa show significant cracking when the pellet was taken from the pressing tool so that no cohesive sample could be obtained. The final relative density of 63% could be obtained only with particle rearrangement without cold sintering. This conclusion is supported by the fact that the final relative density is close to the theoretical random packing of spherical particles of 63.5% [19]. This low relative density and the lack of cohesion of the samples suggests that room-temperature cold sintering seems to be absent for the HA particles.
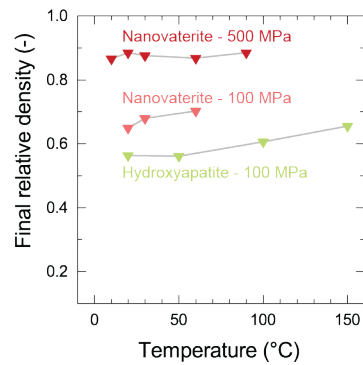
Figure 3.5: Relative density of HA and nanovaterite agglomerates as a function of temperature.

As for nanovaterite and ZnO, we characterized the strength of the particle network using a colloidal model analogy. Two different stages can be identified in the stage 1 densification (Figure 3.4d). Up to a pressure of 100 MPa, we find a γ exponent of 3.4 which indicates a rather weak packing of particles (Figure 3.4d). At pressures higher than 100 MPa, the exponent increases to 12.6. Such a high exponent suggests a much denser network of particles that are more resistant to densification. A possible interpretation for the two different γ exponents is that the loosely-packed network observed at low applied stresses comprises platelet-like HA agglomerates, whereas the denser network formed at high stresses consist of nanoparticles inside the agglomerates. This possible scenario is supported by the fact that platelet-shaped agglomerates are likely to form looser networks that are easily ruptured upon mechanical loading. If this hypothesis is correct, the high exponent obtained at higher stresses (γ = 12.6) indicate that the HA nanoparticles reach high packing densities inside agglomerates, thus hindering any further densification.

The effect of pressure on the densification behavior of HA platelets at room temperature is significantly smaller than that observed for the nanovaterite powder ($CaCO_3$). However, literature results have shown that HA can be sintered at temperatures as low as 150 °C in the presence of water [4]. This indicates that higher temperatures could in principle enhance the densification of the HA agglomerates.

To evaluate this hypothesis, we finally investigated the influence of temperature on the densification process of our hierarchically-organized HA agglomerates with water. Hydrothermal sintering of HA nanopowders at mild temperatures has been reported in literature [4]. Grossin *et al.* for example pressed hydrated apatite powder in a Spark Plasma Sintering oven at 100 MPa and 150 °C and measured a final density of 2 g cm^{-3} (relative density of 79%). Following this earlier work, we performed experiments at room temperature, 50, 100 and 150 °C and at an applied pressure of 100 MPa. The results of our compaction experiments show an increase in final density from 56% at room temperature and 50 °C to 66% at 150 °C

(Figure 3.5). The increase in relative density follows a linear trend between 50 and 150 °C. Because hydrothermal processes are operative at 150°C, the dissolution and recrystallization of materials is expected at these conditions, even in materials that are relatively insoluble at room temperature [20]. Despite the increase in density, the samples produced at temperatures above room temperature did not lead to a cohesive pellet. We compare the effect of temperature on the densification of HA with that of the nanovaterite reference powder (Figure 3.5). The effect of temperature on the final density of nanovaterite depends on the pressure applied. At 500 MPa the final density remains between 87% and 88%. By contrast, for an applied pressure of 100 MPa, the final density increases from 65% to 70% when the temperature is changed from room temperature to 60 °C. We cannot report the final density of nanovaterite at 100 MPa and 90 °C since we observed a phase transformation from vaterite to calcite during the cold sintering process at this temperature (Appendix C Figure C.3). This transformation also led to a sample that was not cohesive enough to be taken from the mold without damage.

The results obtained for HA powder agrees with previous literature data indicating low densification at temperatures below 150 °C. Similar to the ZnO powder, the hierarchical morphology of the HA agglomerates does not seem to contribute to the densification of this material under pressure with water.

3.4. Conclusions

The compaction behavior of zinc oxide and hydroxyapatite powders at room temperature in the presence of water provides new insights into the possible mechanisms governing the densification of nanovaterite via cold sintering. Using ZnO and HA particles, it was possible to check whether a hierarchical morphology or the capacity of the material to crystalize in water at room temperature would help the densification process. We found that the hierarchical morphology of these powders is not sufficient to promote room-temperature cold sintering, which remains specific to nanovaterite agglomerates.

Our analysis of the compaction behavior during mechanical loading of the ZnO particles (stage 1) reveal that the nanoparticles are already strongly packed within the agglomerates, thus preventing significant deformation and densification of the powder during uniaxial pressing. Hence, the sintering temperature of around 85 °C for the cold densification of ZnO cannot be further reduced by using powders with hierarchical morphology.

The results for the HA platelets indicate an enhanced densification of the powder up to a pressure of 100 MPa. This probably results from the pressure-induced rearrangement of loosely-packed platelets into more compact structures. At higher pressure, the resistance of

the material against densification becomes significantly higher, which indicates the presence of tightly-packed nanoparticles within the platelet-like agglomerates. This limits the ability of the platelets to deform under the imposed pressure. By increasing the temperature, the relative density of the pellet could be increased from 56% to 66%, but samples were not cohesive after removal from the mold.

Our study suggests that the poor packing of nanoparticles within vaterite agglomerates might play an important role on the pressure-assisted densification of this powder at room temperature. Cold sintering of nanovaterite particles is likely intimately linked with the specific morphology and chemical composition of this powder.

Acknowledgements

References

[1]   F. Bouville, A.R. Studart, Geologically-inspired strong bulk ceramics made with water at room temperature, Nat. Commun. 8 (2017) 14655.

[2]   J. Guo, H. Guo, A.L. Baker, M.T. Lanagan, E.R. Kupp, G.L. Messing, C.A. Randall, Cold Sintering: A Paradigm Shift for Processing and Integration of Ceramics, Angew. Chem. Int. Ed. 55(38) (2016) 11457-11461.

[3]   T. Ibn-Mohammed, C.A. Randall, K.B. Mustapha, J. Guo, J. Walker, S. Berbano, S.C.L. Koh, D. Wang, D.C. Sinclair, I.M. Reaney, Decarbonising ceramic manufacturing: A techno-economic analysis of energy efficient sintering technologies in the functional materials sector, J. Eur. Ceram. Soc. 39(16) (2019) 5213-5235.

[4]   D. Grossin, S. Rollin-Martinet, C. Estournès, F. Rossignol, E. Champion, C. Combes, C. Rey, C. Geoffroy, C. Drouet, Biomimetic apatite sintered at very low temperature by spark plasma sintering: Physico-chemistry and microstructure aspects, Acta Biomater. 6(2) (2010) 577-585.

_____

[5]   B. Dargatz, J. Gonzalez-Julian, O. Guillon, Improved compaction of ZnO nano-powder triggered by the presence of acetate and its effect on sintering, Sci. Technol. Adv. Mater. 16(2) (2015) 025008.

[6]   H. Kähäri, M. Teirikangas, J. Juuti, H. Jantunen, Dielectric Properties of Lithium Molybdate Ceramic Fabricated at Room Temperature, J. Am. Ceram. Soc. 97(11) (2014) 3378-3379.

[7]   M. Haug, F. Bouville, C. Ruiz-Agudo, J. Avaro, D. Gebauer, A.R. Studart, Cold densification and sintering of nanovaterite by pressing with water, J. Eur. Ceram. Soc. 40(3) (2020) 893-900.

[8]   B.V. Parakhonskiy, A. Haase, R. Antolini, Sub-Micrometer Vaterite Containers: Synthesis, Substance Loading, and Release, Angew. Chem. Int. Ed. 51(5) (2012) 1195-1197.

[9]   N. Kränzlin, M. Niederberger, Wet-Chemical Preparation of Copper Foam Monoliths with Tunable Densities and Complex Macroscopic Shapes, Adv. Mater. 25(39) (2013) 5599-5604.

[10]   D. Jezequel, J. Guenot, N. Jouini, F. Fievet, SUBMICROMETER ZINC-OXIDE PARTICLES - ELABORATION IN POLYOL MEDIUM AND MORPHOLOGICAL-CHARACTERISTICS, J. Mater. Res. 10(1) (1995) 77-83.

[11]   A. Jha, E. Elmadani, T. Peralli, M.S. Duggal, D. Walsh, C. Jappy, T. Brown, W. Sibbett, Microstructural characterization of laser sintered synthetic calcium phosphate-natural dentine interface for the restoration of enamel surface, AIMS Mater. Sci. 1(3) (2014) 148-158.

[12]   M.H. Prado Da Silva, J.H.C. Lima, G.A. Soares, C.N. Elias, M.C. de Andrade, S.M. Best, I.R. Gibson, Transformation of monetite to hydroxyapatite in bioactive coatings on titanium, Surf. Coat. Technol. 137(2) (2001) 270-276.

[13]   R.B. Reed, D.A. Ladner, C.P. Higgins, P. Westerhoff, J.F. Ranville, Solubility of nano-zinc oxide in environmentally and biologically important matrices, Environ. Toxicol. Chem. 31(1) (2012) 93-99.

[14]   W.M. Haynes, D.R. Lide, T.J. Bruno, CRC handbook of chemistry and physics: a ready-reference book of chemical and physical data., 97 ed., CRC Press, Boca Raton, Florida, USA, 2016.

[15]   M. de Jong, W. Chen, T. Angsten, A. Jain, R. Notestine, A. Gamst, M. Sluiter, C. Krishna Ande, S. van der Zwaag, J.J. Plata, C. Toher, S. Curtarolo, G. Ceder, K.A. Persson, M. Asta, Charting the complete elastic properties of inorganic crystalline compounds, Sci. Data 2(1) (2015) 150009.

_____

[16]   H.W. Kaufman, I. Kleinberg, Studies on the incongruent solubility of hydroxyapatite, Calcif. Tissue Int. 27(1) (1979) 143.

[17]   H. Cölfen, A crystal-clear view, Nat. Mater. 9(12) (2010) 960-961.

[18]   A.R. Studart, E. Amstad, L.J. Gauckler, Yielding of weakly attractive nanoparticle networks, SOFT MATTER 7(14) (2011) 6408-6412.

[19]   M.N. Rahaman, Ceramic Processing and Sintering, 2 ed., CRC Press2003.

[20]   K. Byrappa, T. Adschiri, Hydrothermal technology for nanotechnology, Prog. Cryst. Growth Charact. Mater. 53(2) (2007) 117-166.

Chapter 4: Multiscale-Deformation Processes during Cold Sintering of Nanovaterite Compacts

Abstract

Cold sintering is a promising route towards the manufacturing of dense ceramics at mild processing conditions, but our poor understanding of the process has prevented the wider spread of this attractive densification approach. Using nanovaterite powders with well-defined multiscale morphology, we perform *in-situ* X-Ray tomography on compacts subjected to controlled mechanical load and quantify the multiscale deformation processes responsible for the water-assisted cold sintering of this powder with the help of instrumented indentation experiments at the micro- and nano-scale. Our results reveal the crucial effect of water in promoting the macroscopic densification process and highlight the dominant role of the nanoparticle network inside agglomerates in controlling the cold sintering of compacts at high mechanical loads. By providing new insights into the deformation processes responsible for the densification effect, this study can potentially guide the discovery of novel chemical compositions and particle morphologies that can be more easily densified through room-temperature cold sintering with water.

4.1. Introduction

Cold sintering of powder compacts is a well-known geological process leading to rock formation in nature [1, 2] and has recently been explored for the fabrication of advanced ceramics for electronic and structural applications [3-6]. In geology, the densification of granular materials through pressure solution creep is an important mechanism underlying the formation and transformations of sedimentary rocks [2, 7]. Pressure solution creep is a cold sintering process that enables the transport of atoms from inter-particle contacts to pore walls in a similar fashion to the conventional densification and sintering of ceramics at high temperatures. As far as ceramics are concerned, cold sintering offers an attractive sustainable pathway for the fabrication of stiff and strong functional materials in aqueous environment at much lower temperature compared to standard sintering conditions [3]. Given its relevance to such a broad spectrum of materials and research fields, cold sintering processes have been intensively studied by the geology and materials science communities in recent years [3, 5, 6, 8].

The densification of powder compacts through cold sintering has been demonstrated for a wide range of chemical compositions and processing conditions [9]. While low-temperature dissolution and reprecipitation processes have long been known to enable the pressure-assisted densification of sedimentary rocks [10], the possibility to cold sinter salts, phosphates, carbonates and oxide ceramics featuring much lower solubility in water has only recently been evidenced by materials scientists [3-11]. Early works exploring this attractive processing route

focused on the cold sintering of hydroxyapatite and lithium molybdate powders under temperatures and pressures in the range of 20-250 °C and 50-130 MPa [5, 11]. Other studies revealed that similar pressures and temperatures can be used to densify ZnO powder compacts through hydrothermal processes [4, 8]. More recent research has shown that hydrothermal conditions can be extended to cold sinter an impressive range of chemical compositions, including various simple and complex oxides, carbonates and salts [6]. Inspired by the densification of carbonates in geological formations, we have demonstrated that the cold sintering of nanovaterite powder is possible even at room temperature by compaction of the powder with water under pressures in the range 10-800 MPa [3]. Despite these several successful demonstrations of cold sintered materials, the microstructural deformation processes underlying the densification of such powders remain poorly understood. In particular, the morphology of the initial powders is expected to play an important role on the room-temperature sintering of nanovaterite with water, but its effect on the deformation processes within the compact under pressure has not yet been systematically studied.

Three-dimensional X-Ray tomography is a powerful *in-situ* experimental technique to assess the deformation processes within materials subjected to mechanical loading [12]. This has allowed for the space and time-resolved quantification of the porosity of metal powder compacts used in powder metallurgy [13, 14], the mapping of strains and defects developed during the mechanical deformation of metals [15], and the analysis of matter transport mechanisms during high-temperature sintering of glass and oxide-based composites [16, 17]. Synchrotron based tomography has also been used to observe particle morphology changes during pressure solution creep of 100 μm sodium chloride particles [18]. Besides *in-situ* tomography, instrumented micro- and nano-indentation has also been extensively employed to quantify the mechanical response and deformation processes in consolidated or pressed materials [19]. By measuring the creep response of specimens tested with different indenter sizes, this technique provides a means to probe deformation processes at different length scales [20]. The combined use of such imaging and mechanical characterization tools should therefore be a powerful approach to study cold sintering phenomenon in powder compacts.

Here, we apply *in-situ* X-Ray tomography and instrumented mechanical indentation to investigate the deformation processes at play during the room-temperature cold sintering of nanovaterite under pressure with water. Because the investigated vaterite powder displays a multiscale morphology comprising agglomerates of interconnected nanoparticles, special attention is given to the quantification of the deformation mechanisms operating at different length scales. To this end, the displacement of vaterite agglomerates during uniaxial pressing is first observed through spatially- and time-resolved imaging using a custom-made mechanical testing setup positioned in a synchrotron beamline. Digital volume correlation is then applied on the reconstructed volumes to map local deformation of the compacts during stress relaxation experiments. This is later complemented with micro- and nano-indentation analysis

to understand the role of the multiscale powder morphology on the cold sintering process. On the basis of these experiments, we finally propose a model to describe the deformation processes responsible for the water-assisted densification of nanovaterite powder under compression.

4.2. Materials and Methods

4.2.1. Synthesis of Nanovaterite Particles

Nanovaterite particles were synthesized following a procedure published in the literature [21]. Briefly, 2 mol L^{-1} aqueous solutions of sodium carbonate (Na_2CO_3, Sigma-Aldrich, Germany) and of calcium chloride (calcium chloride dihydrate, $CaCl_2 \cdot 2H_2O$, Merck, Germany) were prepared with deionized (DI) water. 16 ml of each solution were diluted with 80 ml of DI water, resulting in a solute concentration of 0.33 mol L^{-1}. The solutions were mixed well for a few minutes and the precipitated vaterite particles were immediately separated from the water by centrifugation at 4500 rpm for 5 min. The particles were then re-dispersed and washed twice with ethanol (94% denatured with toluene, Alcosuisse) before drying in an oven at 60 °C overnight and at 120 °C for another 24 h. One batch typically resulted in 3 g of $CaCO_3$ particles.

4.2.2. Characterization of the Nanovaterite Particles

The crystallographic phase of the particles was characterized by X-Ray powder diffraction (XRD, Panalytical X'Pert PRO MPD, Netherlands) using a Cu anode (generation voltage 40 kV, tube current 45 mA) and a monochromator. The time per step was set to 600 s and the step size to 0.0167° while varying the 2θ angle from 10° to 70°. The morphology of the particles was analyzed by scanning electron microscopy (SEM, Zeiss, LEO 1530, Zeiss, Germany). Prior to acquiring the images, the particles were coated with a 5 nm layer of Pt in order to make the samples electrically conductive.

4.2.3. Tomography Set Up

To build the custom-made pressing die and punch, a round single boron tube (outer diameter: 1.27 mm, inner diameter: 0.50 mm, length: 50 mm) and a solid rod (diameter: 0.50 mm, length: 50 mm) made from alumina (99.8%) were acquired from Ortech Inc. (Sacramento, Ca, USA). The tube was cut into small pieces, each 6 mm long with a wire saw. For the lower part of the pressing die the inner solid rod was carefully broken to reach 2 mm inside the tube. The

upper part of the pressing tool was broken to remain 2 mm outside the die in the absence of powder in the cavity. The lower part of the pressing tool together with the outer tube was glued onto a metallic base plate using super glue (UHU, Superflex Gel).

For the tomography experiments, the particles were mixed with water to reach a liquid-to-powder (L/P) mass ratio of 0.25. After filling the cavity with either the prepared wet powder or dry powder, the pressing tool was taped to better accommodate the nanovaterite particles. The pressing punch was inserted and used to slightly compact the powder before placing the setup in a custom-made tensile/compression rig positioned at the beam line. More details on the rig can be found in previous work by Maire *et al.* [15]. To ensure that the water would not evaporate from the wet sample during the measurement, a drop of water was placed on top of the pressing tool before the series of scans started.

The rig was used to increase the force acting on the powder while a constant displacement rate was applied. Once the desired forces of 20 N (100 MPa) or 100 N (500 MPa) were reached the tester was stopped manually. Force and displacement data were recorded at a frequency of 2 Hz. Scans were then acquired at constant displacement after 2, 5, 10, 30 and 30 min to track the movement of the particles over time.

A PCO-Edge 5.5 Camera was used in a Optic Peter MB optical microscope at a magnification of 4 resulting in a lateral pixel size of 0.165 in the projections. The exposure time was 30 ms per projection with no delay time. The following scanning settings were used: 601 projections, 20 darks and 40 flats with no inter-flats. The sample was rotated by a total amount of 180°. The dimension in pixels of the projections was 2560x2160 pixels. We used a paganin phase retrieval algorithm and adjusted the rotation center. For the reconstruction, the Gridrec algorithm with the ramp filter was employed. The reconstruction was stored slice by slice as .tif files coded on 8 bits.

4.2.4. Digital Volume Correlation

The slices were scaled down by a factor of 0.25 in all 3 dimensions by applying the 'scale' command from Fiji [22] to obtain a stack of processable size. Averaging was used during downsizing. Images from the different time steps were loaded into one hyper stack. A region of interest in the lower part of the 3D volume was selected to apply the Fiji plugin 'correct 3D drift' to correct for the drift between the different time steps. We cropped a circle in Fiji to remove the reconstruction artifacts on the edge of the 3D volume. The outside was afterwards manually set to the value 0 (black). Black slices with no information on the top and the bottom were removed and the different time steps were taken apart again. The images were then ready to run with the digital volume correlation algorithm.

The .tif images were eventually loaded into MatLab and saved as .mat files. With these files, the fast iterative digital volume correlation algorithm for large deformations (FIDVC) was run [23]. The calculated results were then exported as .vtk files and visualized in Paraview [24]. To convert the output file from pixels to displacement, we multiplied the data by 4 (downsizing) and by 0.1625 μm pix^{-1} (resolution).

4.2.5. Indentation

Samples for indentation experiments were cold sintered prior to the testing. To this end, 0.3 g of particles were mixed with 0.075 ml of DI water, poured into a pressing tool (Modell 10, Gr. 2, diameter 11 mm, P/O Weber, Germany) and pressed at 500 MPa for 1 hour using a mechanical testing machine (Instron 8562, Instron). The resulting pellets were 87% dense. The pellets were fixed onto the stage for indentation using a wax. The indentation was performed in a NanoTest Vantage from Micro Mechanics (Wrexham, U.K.) using a Berkovich tip. For the microindents, the force was increased with a speed of 80 mN s^{-1} until a holding force of 4800 mN was reached. The sample was then unloaded with the same speed. For the nanoindents, we programmed the instrument to perform an array of 100 indents (10 by 10). In this case, the force was increased with a speed of 0.25 mN s^{-1} until the holding force of 5 mN was reached. The sample was unloaded with the same speed. Specimens measured under wet conditions were soaked in water prior to the test. A wet sponge was attached next to these samples to minimize water evaporation during the measurement.

4.3. Results and Discussion

4.3.1. Multiscale Spatial and Temporal Analysis of the Cold Sintering Process

Vaterite compacts that undergo cold sintering exhibit a multiscale structure, consisting of an assembly of interconnected nanoparticles inside individual agglomerates and the assembly of agglomerates into a macroscopic sample of well-defined geometry (Figure 4.1 top row). The deformation of the assembly of nanoparticles and the assembly of agglomerates under the imposed uniaxial stress determines the creep rate, the final relative density, and the possible build-up of density gradients within the compacts. To shed light on the contribution of these multiscale deformation processes on the cold sintering of vaterite compacts we employ in-situ X-Ray tomography during uniaxial pressing and instrumented mechanical indentation on compacted samples at two different length scales (Figure 4.1 bottom row). In-situ X-Ray
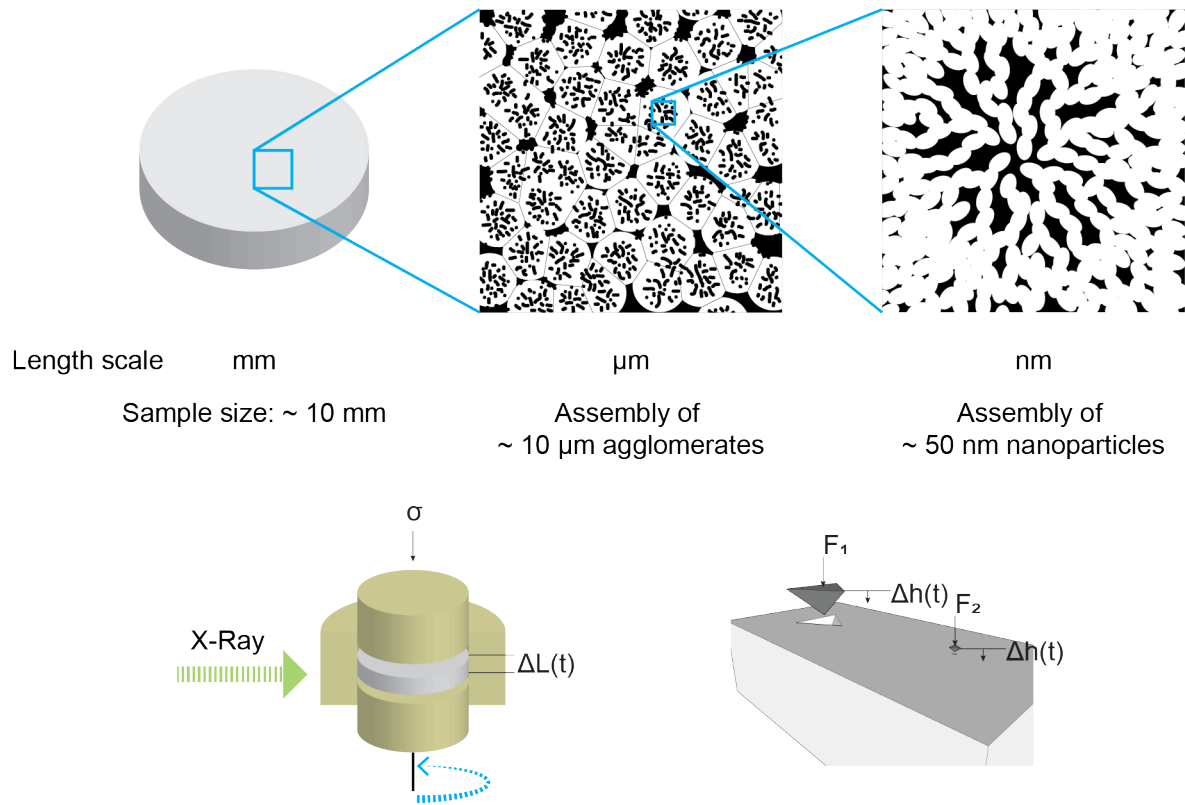
Figure 4.1: Schematics of the multiscale structure of the nanovaterite compacts and the characterization tools used to study the cold sintering process. Top row: Hierarchical structure of the vaterite compact, indicating (left) the macroscopic sample, (middle) the assembly of micron-sized agglomerates of vaterite nanoparticles, and (right) the network of vaterite nanoparticles inside an agglomerate. Bottom row: multiscale mechanical analysis of the vaterite compacts using (left) macroscopic mechanical tests coupled with in-situ synchrotron X-Ray tomography, and (right) instrumented indentation at the micro- and nanoscale.

tomography was used to quantify the deformation of agglomerates throughout the mechanically-loaded compact by measuring the evolution of local displacement in stress relaxation experiments. Instrumented mechanical indentations were performed on compacted specimens to measure the deformation of the assembly of nanoparticles and of the assembly of agglomerates at the micro- and nano-scales, respectively, and their contributions to the overall creep rate of the macroscopic vaterite sample.

Specimens for these experiments were prepared from nanovaterite powder obtained from the precipitation of calcium chloride and sodium carbonate in water, as previously reported [21]. The precipitation reaction results in spherical agglomerates in the size range 8-15 µm, which are formed by interconnected nanoparticles with size on the order of 50 nm (Figure 4.2). X-Ray diffraction of the precipitated powder confirms the formation of vaterite crystals. The presence of a calcite peak in the X-Ray diffraction spectrum is associated with the formation of a few large calcite particles that are readily visible by SEM imaging [21].
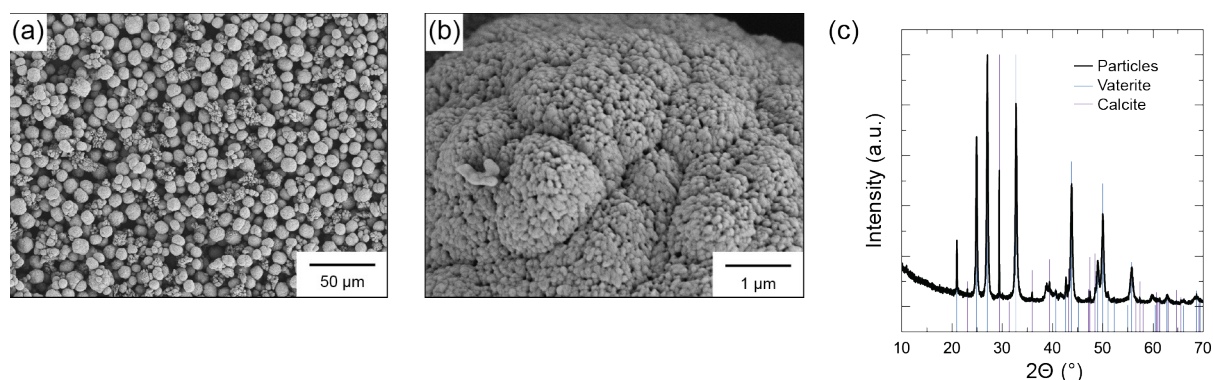
Figure 4.2: Nanovaterite powder used for the preparation of compacts. (a) Spherical vaterite agglomerates obtained after the precipitation reaction. (b) Hierarchical structure of the vaterite agglomerates, highlighting the presence of interconnected nanoparticles at smaller length scales. (c) X-Ray powder diffraction of the precipitated nanopowder, which indicates the predominant formation of vaterite crystals.

4.3.2. In Situ X-Ray Synchrotron Tomography

The compaction behavior of the vaterite powder was investigated by performing *in-situ* X-Ray tomography while the sample was subjected to uniaxial die pressing in a custom-made mechanical tester (Figure 4.3a, b). To enable the visualization of individual agglomerates, this experimental setup was assembled in a synchrotron light source that provides a pixel size of 162.5 nm and temporal resolution of 0.03 Hz (PSI, Villigen). The vaterite powder was pressed inside a custom-made alumina crucible of 0.50 mm inner diameter with walls that are sufficiently thin to minimize X-Ray attenuation but thick enough to enable compression of the sample under a uniaxial stress of up to 500 MPa (Figure 4.3c, d). By rotating the cylindrical sample around its long axis during the measurement, three-dimensional reconstructions of the microstructure were first obtained when the targeted pressure was reached. This was followed by tomography measurements 2, 5, 10, 20 and 30 min after the initial scan under external pressure (Figure 4.3c). The spatial resolution achieved at the beamline was high enough to visualize the shape of individual particles (Figure 4.3d).

Compression experiments were carried out by applying uniaxial pressures of 100 or 500 MPa onto the powder with water (wet) or under dry conditions. This initial pressure was reached by applying a constant displacement rate in the first stage of the compression test. After this maximum pressure was reached, the sample was allowed to relax under the initially imposed displacement (stage 2, Figure 4.3c). The results of the compression experiments show a significant effect of the presence of water on the stress relaxation behavior of the vaterite compacts. A stress drop of 40% was observed in the presence of water for samples subjected to a uniaxial pressure of 500 MPa. By contrast, the experiment with dry powder showed a
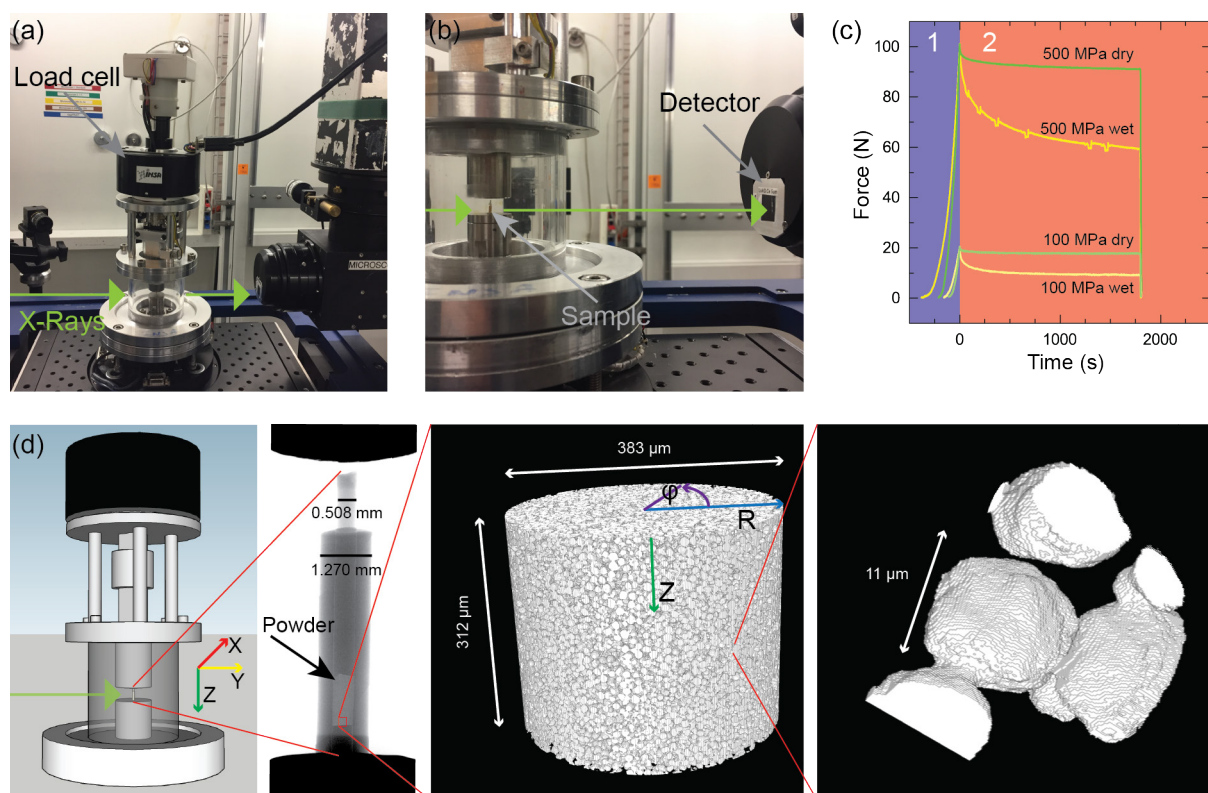
_____

Figure 4.3: In-situ synchrotron X-Ray tomography setup and three-dimensional reconstructed images of a mechanically-tested compact. *(a,b) Mechanical testing apparatus positioned in front of an X-Ray beamline at the synchrotron facility. (c) Mechanical compaction (stage 1, blue) and stress relaxation (stage 2, red) curves recorded simultaneously with the in-situ X-Ray tomography measurements. (d) Schematic representation of the uniaxial pressing tool under the load cell (left), highlighting the location of the nanovaterite powder inside the custom-made alumina crucible (middle left). The load cell was constructed to fit into the beamline and can rotate freely to acquire all necessary images for the 3D reconstruction. Representative 3D reconstruction of the vaterite compact acquired at the bottom of the pressing tool (middle right), indicating the coordinate system used to describe the compaction process and a representative reconstruction of several nanovaterite agglomerates showing the necks between them (right).*

stress drop of only 10% for this initial pressure. A similar trend was found for the specimens subjected to the initial stress of 100 MPa.

The observed stress relaxation is caused by the deformation of particles and agglomerates within the mechanically-loaded vaterite compact. To quantify the deformation at the length scale of agglomerates, we performed digital volume correlation analysis between tomographic images obtained at 0 min and after 30 min at the end of the stress relaxation experiments (Figure 4.4a). The displacement vectors obtained by digital volume correlation provide valuable information about local variations in the relative motion of agglomerates within the sample. To analyze such local variations we map the length of the displacement vector along the Z direction using 2D vertical slices of the reconstructed tomograms (Figure 4.4b). Longitudinal displacements at selected radial positions at the center and edges of the reconstructed
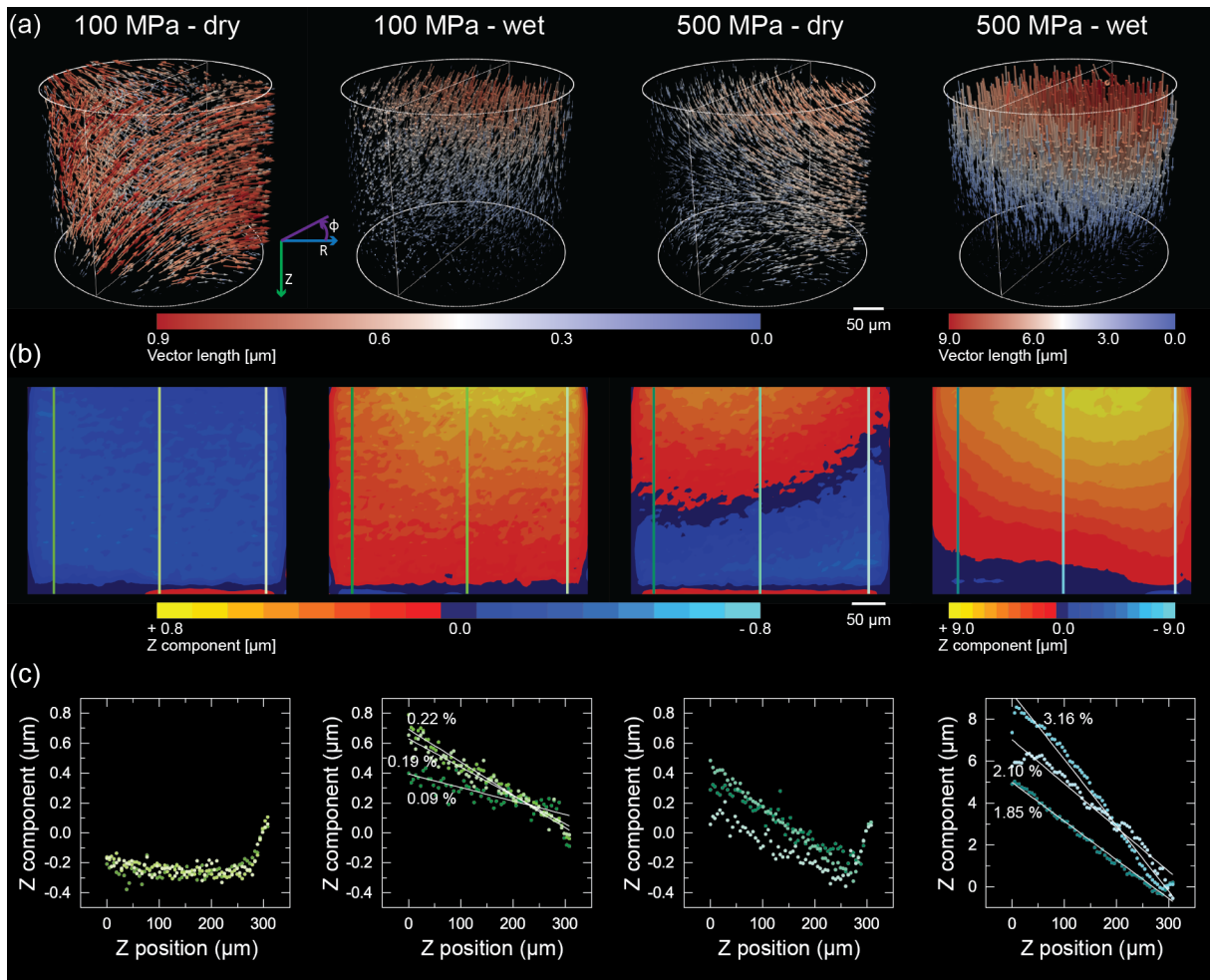
Figure 4.4: Displacement of agglomerates after stress relaxation of vaterite compacts subjected to distinct mechanical loading conditions. *(a) 3D representations of the total displacement vectors indicating the motion of agglomerates inside vaterite compacts initially loaded with 100 or 500 MPa under dry or wet conditions. The displacement vectors were measured by Digital Volume Correlation of image-stacks acquired at the beginning (0 min) and end (30 min) of the stress relaxation experiments. (b) Contour plots displaying the magnitude of agglomerate displacement along the z direction for representative vertical slices of the 3D volumes shown in (a). The color code represents the magnitude of the vector component. (c) z-displacement of agglomerates as a function of the sample height for different mechanical testing conditions. The displacement data were obtained along the three different radial positions shown in Figure 4.4b. Lines were fitted to the displacement data to estimate the local strain along the edges and center of the compact after stress relaxation.*

tomograms are then plotted as a function of the sample height to quantitatively compare the deformation of the compact under different testing conditions (Figure 4.4c).

The resulting plots show that a clear negative displacement gradient develops along the height (*z*) of the compacts tested in water, whereas dry samples display a less-defined displacement profile in the *z* direction with even a positive gradient in the bottom half of the pressing tool. The negative displacement gradient measured for the wet samples indicates the development of strong compressive strains inside the compact along the pressing direction. For samples subjected to an external stress of 500 MPa, the displacements are 10-fold higher than those

measured for specimens tested in the dry state under the same pressure. This shows that the presence of water clearly promotes the densification of the compact through the longitudinal displacement of vaterite agglomerates. Such longitudinal displacement arises most likely from deformation processes at the contact points between agglomerates, which change their initial spherical morphology into more densely packed truncated shapes. In contrast to the wet compacts, specimens tested in the dry state showed no detectable longitudinal displacement at 100 MPa and a relatively weak compressive longitudinal displacement at 500 MPa. The significant radial (off-axis) displacement observed in these dry specimens (Figure 4.4a) suggest that the agglomerates in these compacts undergo lateral rearrangements that do not allow for an effective reduction of the material's internal stresses. Such behavior is typical of brittle powders subjected to uniaxial pressing [25].

To better quantify the longitudinal compressive strains developed during the cold sintering process with water, we evaluate in more details the displacement gradients formed within the wet specimen pressed at 500 MPa. Longitudinal strains ϵ_z are directly obtained from the slope of the line fitted to the z displacement value, d_z, when plotted against the height (z) of the sample: $\epsilon_z = \frac{\partial d_z}{\partial z}$. Using this fitting approach, strain data at selected radial positions at the center and edges of the compact were derived from the reconstructed tomographs (Figure 4.4c). The slopes of the fitted data show that the wet samples subjected to 500 MPa reach longitudinal strain values as high as 2% and 3% at the edge and close to the center of the compact, respectively. The lower strain at the edge of the compact may result from the friction of the powder that is located closer to the walls of the alumina die. The observed difference in compressive strain leads inevitably to a densification gradient between the center and the edge of the compact. Taking the experimentally-measured relative density of 79% at the beginning of the stress relaxation test, we estimate the relative densities at the center and at the edge of the compact to reach, respectively, 81% and 82% at the end of the experiment.

In addition to the total strain at the end of the densification process, we also use our 3D reconstructed tomographs to assess the evolution of the strain distribution inside the wet compact during stress relaxation (Figure 4.5). This provides valuable information about the propagation of the externally imposed stress throughout the compact microstructure. For wet specimens pressed at 500 MPa, the restructured tomographs indicate that most of the longitudinal displacement within the compact develops in the first few couple of minutes of the 30-min long stress relaxation experiment (Figure 4.5a,b). Indeed, the net displacement measured after 2 minutes is about 3 times higher than that observed in the last 10 minutes of the test. Such a high initial deformation releases some of the elastic energy stored in the pressed compact, resulting in the strong stress relaxation detected by the mechanical load cell in the beginning of the test.
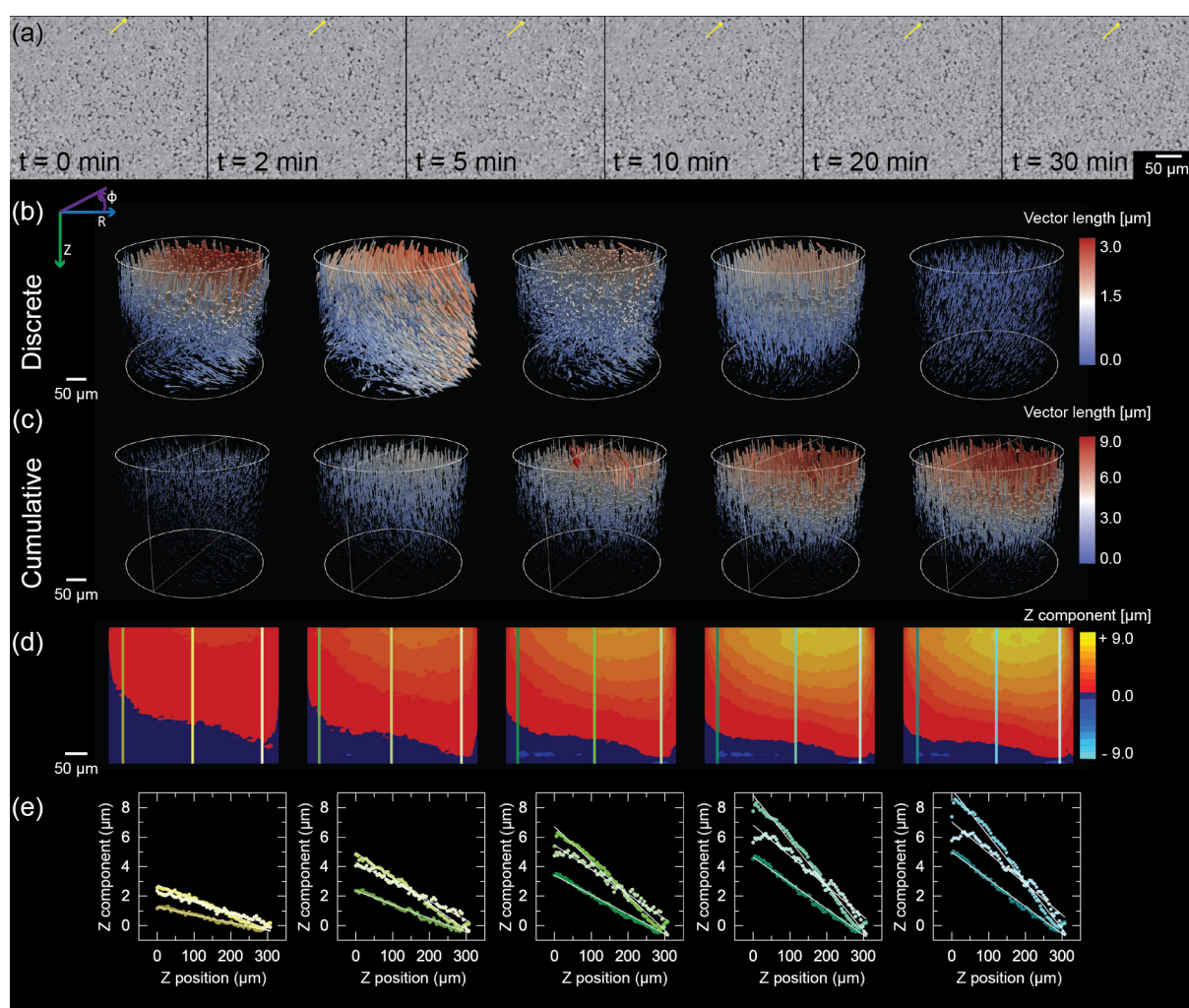
Figure 4.5: Evolution of the agglomerate displacement during stress relaxation of vaterite compacts initially pressed at 500 MPa with water. (a) Snapshots of the microstructure of the compact obtained at different time points along the stress relaxation process. The images correspond to vertical slices of 3D tomography reconstructions. The local displacement of agglomerates inside the compact is qualitatively illustrated by tracking a pore positioned close to the top of the specimen (yellow arrow). (b,c) 3D representations of the displacement vectors of agglomerates measured (b) between snapshots or (c) accumulated over the entire stress relaxation experiment. The color code represents the magnitude of the vector. (d) Contour plots displaying the magnitude of agglomerate displacement along the z direction for representative vertical slices of the 3D volumes shown in (c). (e) z-displacement of agglomerates as a function of the sample height measured at the edges and center of the compact at selected time points along the test.

Analysis of the cumulative displacement maps at the early stage of the relaxation experiment also indicates that the developed strain is uniform along the entire height of the compact within the first minutes of the test (Figure 4.5c, d). The lack of strain gradients within the sample implies the existence of an elastic network of percolating agglomerates, which quickly distributes the externally applied stress through stress transfer at inter-agglomerate contacts (Figure 4.3d). Despite the uniform strain distribution along the height of the sample, we found that the expected lower strains at the edge of the compact are already visible at a very early stage of the stress relaxation experiment. This is evident by comparing the estimated strains

at the edge and at the center of the specimen as a function of time. Such comparison shows that the strain mismatch remains relatively constant throughout the densification process (Figure 4.5d, e). In addition to the increased friction of the powder located closer to the die walls, the observed radial gradient and the asymmetry of the displacement data might also arise from the fact that the pressing punches used in these experiments are not perfectly flat.

4.3.3. Instrumented Micro and Nano Indentation

Whereas the high longitudinal strains developed within the wet compacts clearly illustrate the strong effect of water on the densification process, elucidating the origin of the observed internal displacements requires further systematic experiments. We address this question by measuring the deformation of the compact at two different length scales using instrumented indentation tools. Indentation tests at the nanoscale are carried out to quantify the deformation of the assembly of nanoparticles within a single agglomerate, whereas measurements at the microscale are conducted to assess the deformation of the assembly of agglomerates at a larger length scale. The experiments were performed under wet or dry conditions by first loading the specimen at a constant force rate, followed by a creep test at a target fixed force (Figure 4.6a, d). The evaluated specimen was prepared by cold sintering the nanovaterite powder with water at 500 MPa to obtain an 11 mm diameter disc with a final relative density of 87%. Scanning electron microscopy images of imprints generated upon indentation confirm that the selected micro or nano-indenters could be appropriately positioned to probe either the assembly of agglomerates or the assembly of nanoparticles, respectively (Figure 4.6c, f). The micro-imprints were typically 100 µm wide and 10 µm deep, whereas the nano-imprints exhibited width of 1 µm and depth of 100 nm. These dimensions are at least 10-fold larger than the average size of a single agglomerate (10 µm) and an individual nanoparticle (50 nm), which validates our experimental protocol as a means to probe the deformation of assemblies of agglomerates and particles at two different length scales.

The creep data obtained from the indentation experiments confirm the crucial effect of water in promoting the densification of the compact under constant mechanical stress (Figure 4.6b, e). Samples containing water displayed 4-fold and 2-fold higher displacements compared to the dry counterparts at the end of the nano- and micro-indentation tests, respectively. Comparison of the creep behavior of wet specimens probed at the nano- and microscales allows us to identify the deformation mechanism controlling the densification of the vaterite compacts. Because of the difference in indented volume at the two different length scales, we compare these two samples in terms of the rate at which the specimen changes its creep compliance (L) over time. Following a previously reported analytical model [20], the creep compliance of the sample can be measured from indentation experiments using the equation:
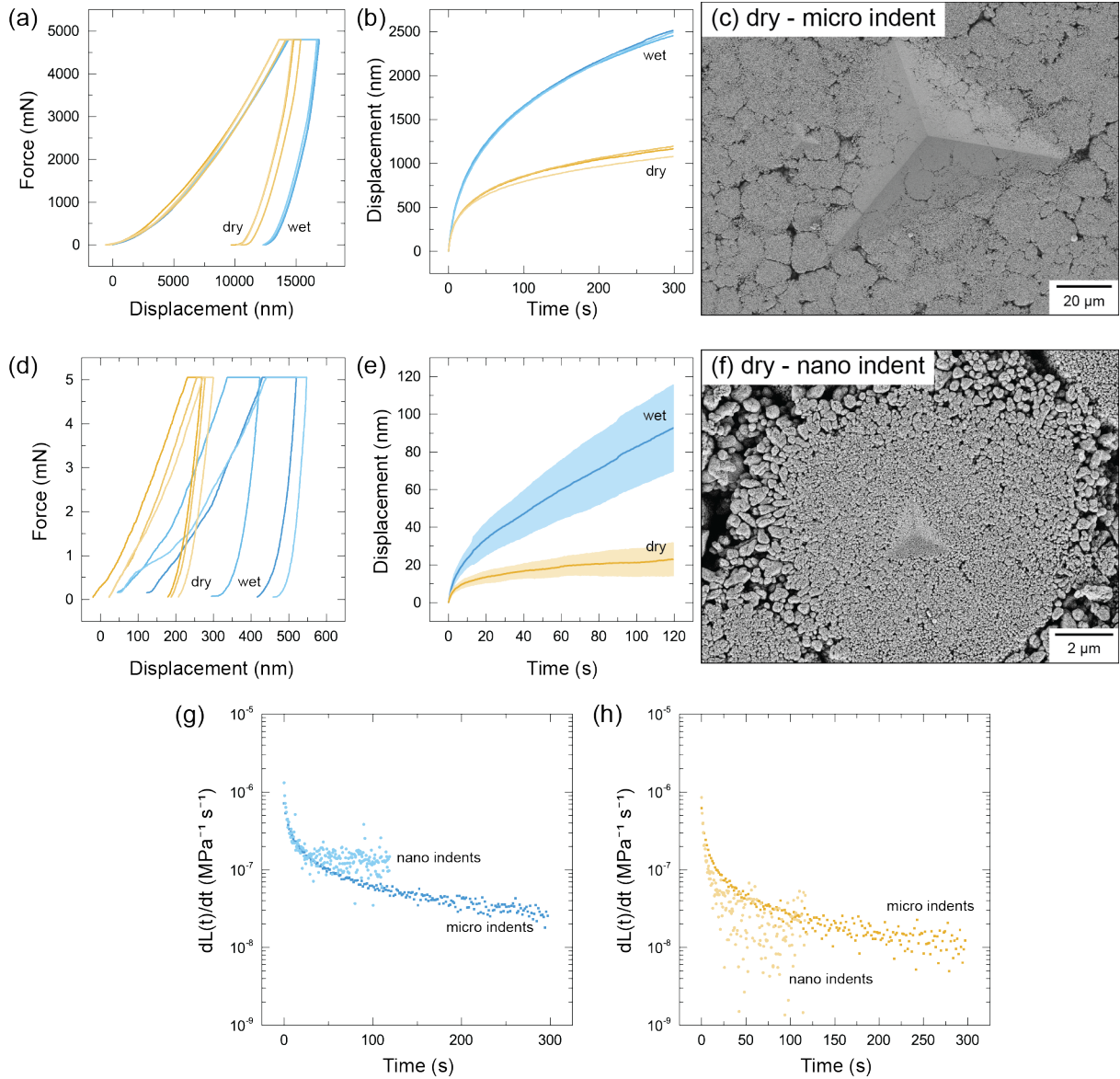
Figure 4.6: Multiscale creep of vaterite compacts measured by mechanical indentation at the nano- and microscales.
(a,d) Force-displacement curves obtained from (a) micro- and (d) nano-indentation experiments performed on a vaterite sample that was previously cold sintered to reach 87% relative density. (b,e) Displacement of the indenter as a function of time obtained from creep tests under constant load at (b) the micro- and (e) the nano-scales. The curves in (e) indicate the average displacement, whereas the shaded areas represent the standard deviation. (c,f) Scanning electron microscopy images depicting the imprints generated on the surface of vaterite specimens after (c) micro- and (f) nano-indentation experiments in dry conditions. (g,h) Evolution of the creep compliance rate (dL(t)/dt) over time for vaterite compacts tested by micro- and nano-indentation in (g) wet or (h) dry conditions.

$$L(t) = \frac{2 \cdot tan(\theta)}{\pi \cdot P_{max}} \cdot h^2(t)$$

<div align="right">*Equation 4.1*</div>

where θ is the half cone angle of the Berkovich indenter used in the experiments (65.3°), P_{max} is the maximum load, and $h(t)$ is the actual indentation depth at a given time t. After calculating the time-dependent compliance of the sample from the indentation depth data,

the resulting creep compliance curves were differentiated with respect to time to determine the creep compliance rate ($dL(t)/dt$) of specimens at the micro- and nano-scales (Figure 4.6g, h) [20].

Our analysis reveals that the creep compliance rate of the wet vaterite compact is approximately twice larger than that of the dry specimen over the entire time window of the experiments. Importantly, we found that the creep compliance rate of samples tested with a nano-indenter display similar or even slightly higher levels compared to the rate measured with the micro-indenter. This indicates that the creep response of the compact is predominantly controlled by the deformation of the assembly of nanoparticles inside an individual agglomerate. Indeed, if the relative displacement between the agglomerates were to play a role in the creep process, this would be reflected in a higher creep compliance rate of samples tested by micro-indentation.

4.4. Conclusions

The cold sintering of nanovaterite powder via uniaxial pressing with water involves deformation processes that operate at multiple length scales. Tomography imaging performed at scales much larger than individual agglomerates show that high uniaxial compressive strains develop within compacts containing water. This enables strong densification along the loading direction for powders subjected to stress relaxation under wet conditions. By contrast, dry pressing leads to predominantly lateral motion of the agglomerates and therefore weak densification along the pressing direction. Because lower compressive strains are achieved closer to the walls of the pressing die, a small difference in relative density between the center and the edges of compact is observed. Snapshots taken during stress relaxation experiments suggest that the vaterite agglomerates form a percolating network that quickly transmits the applied external stresses throughout the powder compact. This indicates that densification under constant mechanical load likely initiates at the contact points between the vaterite agglomerates. The high stresses developed at such contact points irreversibly deforms the network of interconnected nanoparticles inside individual agglomerates, which become truncated and more closely packed within the compact. The irreversible deformation of the nanoparticle network within each agglomerate ultimately controls the densification rate of the entire compact. This implies that possible agglomerate rearrangement events occur predominantly in the initial loading stage of the pressing operation, leaving further gains in densification to the deformation of the nanoparticles inside agglomerates. Our experimental study provides important insights onto the effect of water and powder morphology on the room-temperature cold sintering of nanovaterite and may help identify novel powders amenable to this environmental-friendly manufacturing technology.

Acknowledgements

References

[1]   P. De Silva, L. Bucea, V. Sirivivatnanon, D.R. Moorehead, Carbonate binders by "cold sintering" of calcium carbonate, J. Mater. Sci. 42(16) (2007) 6792-6797.

[2]   J.-P. Gratier, D.K. Dyshe, F. Renard, Chapter 2 - The Role of Pressure Solution Creep in the Ductility of the Earth's Upper Crust, Adv Geophys 54 (2013) 47-179.

[3]   F. Bouville, A.R. Studart, Geologically-inspired strong bulk ceramics made with water at room temperature, Nat. Commun. 8 (2017) 14655.

[4]   B. Dargatz, J. Gonzalez-Julian, O. Guillon, Improved compaction of ZnO nano-powder triggered by the presence of acetate and its effect on sintering, Sci. Technol. Adv. Mater. 16(2) (2015) 025008.

[5]   H. Kähäri, M. Teirikangas, J. Juuti, H. Jantunen, Dielectric Properties of Lithium Molybdate Ceramic Fabricated at Room Temperature, J. Am. Ceram. Soc. 97(11) (2014) 3378-3379.

[6]   J. Guo, H. Guo, A.L. Baker, M.T. Lanagan, E.R. Kupp, G.L. Messing, C.A. Randall, Cold Sintering: A Paradigm Shift for Processing and Integration of Ceramics, Angew. Chem. Int. Ed. 55(38) (2016) 11457-11461.

[7]   X. Zhang, C.J. Spiers, Compaction of granular calcite by pressure solution at room temperature and effects of pore fluid chemistry, Int. J. Rock Mech. Min. Sci. 42(7-8) (2005) 950-960.

[8]   J. Gonzalez-Julian, K. Neuhaus, M. Bernemann, P.J. da Silva, A. Laptev, M. Bram, O. Guillon, Unveiling the mechanisms of cold sintering of ZnO at 250 °C by varying applied stress and characterizing grain boundaries by Kelvin Probe Force Microscopy, Acta Mater. 144 (2018) 116-128.

[9]   J. Guo, R. Floyd, S. Lowum, J.-P. Maria, T.H.d. Beauvoir, J.-H. Seo, C.A. Randall, Cold Sintering: Progress, Challenges, and Future Opportunities, Annu. Rev. Mater. Res. 49(1) (2019) 275-295.

[10]   P.K. Weyl, Pressure solution and the force of crystallization: a phenomenological theory, J. Geophys. Res. 64(11) (1959) 2001-2025.

[11]   D. Grossin, S. Rollin-Martinet, C. Estournès, F. Rossignol, E. Champion, C. Combes, C. Rey, C. Geoffroy, C. Drouet, Biomimetic apatite sintered at very low temperature by spark plasma sintering: Physico-chemistry and microstructure aspects, Acta Biomater. 6(2) (2010) 577-585.

[12]   E. Maire, P.J. Withers, Quantitative X-ray tomography, Int. Mater. Rev. 59(1) (2014) 1-43.

[13]   O. Lame, D. Bellet, M.D. Michiel, D. Bouvard, In situ microtomography investigation of metal powder compacts during sintering, Nucl. Instrum. Methods Phys. Res., Sect. B 200 (2003) 287-294.

[14]   O. Lame, D. Bellet, M. Di Michiel, D. Bouvard, Bulk observation of metal powder sintering by X-ray synchrotron microtomography, Acta Mater. 52(4) (2004) 977-984.

[15]   E. Maire, C. Le Bourlot, J. Adrien, A. Mortensen, R. Mokso, 20 Hz X-ray tomography during an in situ tensile test, Int. J. Fract. 200(1) (2016) 3-12.

[16]   A. Nommeots-Nomm, C. Ligorio, A.J. Bodey, B. Cai, J.R. Jones, P.D. Lee, G. Poologasundarampillai, Four-dimensional imaging and quantification of viscous flow sintering within a 3D printed bioactive glass scaffold using synchrotron X-ray tomography, Materials Today Advances 2 (2019) 100011.

[17]   Z. Yan, O. Guillon, C.L. Martin, S. Wang, C.-S. Lee, F. Charlot, D. Bouvard, Correlative Studies on Sintering of Ni/BaTiO3 Multilayers Using X-ray Computed Nanotomography and FIB-SEM Nanotomograhy, J. Am. Ceram. Soc. 98(4) (2015) 1338-1346.

[18]   F. Renard, D. Bernard, X. Thibault, E. Boller, Synchrotron 3D microtomography of halite aggregates during experimental pressure solution creep and evolution of the permeability, Geophys. Res. Lett. 31(7) (2004).

[19]   W.C. Oliver, G.M. Pharr, An improved technique for determining hardness and elastic modulus using load and displacement sensing indentation experiments, J. Mater. Res. 7(6) (1992) 1564-1583.

[20]   M. Vandamme, C.A. Tweedie, G. Constantinides, F.-J. Ulm, K.J. Van Vliet, Quantifying plasticity-independent creep compliance and relaxation of viscoelastoplastic materials under contact loading, J. Mater. Res. 27(1) (2011) 302-312.

[21] B.V. Parakhonskiy, A. Haase, R. Antolini, Sub-Micrometer Vaterite Containers: Synthesis, Substance Loading, and Release, Angew. Chem. Int. Ed. 51(5) (2012) 1195-1197.

[22] J. Schindelin, I. Arganda-Carreras, E. Frise, V. Kaynig, M. Longair, T. Pietzsch, S. Preibisch, C. Rueden, S. Saalfeld, B. Schmid, J.-Y. Tinevez, D.J. White, V. Hartenstein, K. Eliceiri, P. Tomancak, A. Cardona, Fiji: an open-source platform for biological-image analysis, Nat. Methods 9(7) (2012) 676-682.

[23] E. Bar-Kochba, J. Toyjanova, E. Andrews, K.-S. Kim, C. Franck, A Fast Iterative Digital Volume Correlation Algorithm for Large Deformations, Experimental Mechanics 55(1) (2015) 261-274.

[24] J. Ahrens, B. Geveci, C. Law, ParaView: An End-User Tool for Large Data Visualization, Visualization Handbook (2005).

[25] M.N. Rahaman, Ceramic Processing and Sintering, 2 ed., CRC Press2003.

Chapter 5: Conclusions

Cold sintering is a newly developed method to densify ceramic materials at temperatures significantly lower than those applied in traditional sintering. Many different materials have been reported to undergo cold sintering, including molybdates, oxides, phosphates, chlorides or carbonates. Vaterite, one polymorph of calcium carbonate, shows an astonishing densification behavior with water at room temperature and under pressure between 100 and 800 MPa. Additionally, the solubility of this carbonate in water is orders of magnitude lower than that of other compounds that can be densified at room temperature, such as sodium chloride or lithium molybdate. This thesis provides new insights into the fundamental mechanisms controlling the water-assisted densification of vaterite powders under pressure.

The densification behavior of calcium carbonate particles was first investigated at a global scale under the influence of several processing parameters such as crystallinity and phase, pH of the aqueous medium, temperature, and pressure. Only samples with vaterite particles consisting of 500 nm agglomerates made of 50 nm nanoparticles led to cohesive and dense samples. Amorphous calcium carbonate and calcite particles showed some densification but could not produce cohesive samples. The pH of the aqueous phase did not affect the densification kinetics nor the final density of vaterite compacts even at pH 1, where the solubility of calcium carbonate is 6 orders of magnitude higher than that at pH 7. These results strongly suggest that dissolution-precipitation mechanisms do not control the cold sintering of the investigated vaterite powder. By increasing the temperature from 10 to 90 °C, the kinetics of the process was changed but did not influence the final density. In stage 1 of the pressing protocol, when the mechanical loading is increased at a constant displacement rate, we observed a faster densification at higher temperatures. By contrast, an increase in temperature led to slower densification in stage 2, during which the displacement is adjusted to maintain a constant pressure. These conflicting observations may be attributed to the multiple parameters which are affected by temperature changes. Among all the parameters investigated, the applied pressure showed the strongest influence on the final relative density of the vaterite compacts.

A detailed investigation on the effect of applied pressure on the densification behavior of the vaterite compacts provided new mechanistic insights into the cold sintering process of this carbonate. The dependence of the relative density on the applied stress is found to be similar to that previously observed for a percolating network of interconnected attractive particles. Furthermore, analysis of the normalized densification rate as a function of the applied stress at constant relative density during stage 2 revealed a power-law dependence with a stress

exponent higher than 6. This suggests that the densification process could originate from dislocation movement or from water-facilitated subcritical crack growth.

In another series of the experiments, the cold sintering strategies and analytical methods used on nanovaterite were applied to zinc oxide (ZnO) with similar hierarchical microstructure and to hydroxyapatite (HA, $Ca_5(PO_4)_3(OH)$), which is able to crystallize in water at room temperature. Both materials did not densify as much as nanovaterite agglomerates under the same range of applied pressures. Therefore, the densification behavior at room temperature seems to be very specific to nanovaterite, at least among the compounds that are sparsely soluble in water. The analysis of stage 1 of the pressing procedure reveals that the ZnO agglomerates seem to form a stronger percolating network than nanovaterite, which makes it more difficult for the nanoparticles to rearrange into a denser structure. The HA particles seem to rearrange into a denser structure at pressures below 100 MPa, but do not densify further at higher applied pressure. Increasing the temperature to 150 °C leads to HA samples with higher relative density but without cohesion. This study confirms that room temperature cold sintering of sparsely soluble materials seems to be intimately linked with the crystal structure and the chemical composition of the powder.

Lastly, cold sintering was investigated at the particle scale using synchrotron *in situ* X-Ray tomography to analyze how the agglomerates collectively rearrange upon uniaxial stress in dry and wet conditions. Pressing the agglomerates with water led to high uniaxial compressive strains, which in turn enabled strong densification. Applying pressure to dry agglomerates however, results in predominantly lateral motions of the particles, which lead to a lower densification. The agglomerates under pressure quickly form a percolating network, which can efficiently transmit and re-distribute the externally applied stress within the entire compact. The applied stress is expected to be intensified at the local contact points between the agglomerates, leading to irreversible deformation in this region. This means that the deformation of the nanoparticle network within one agglomerate at the contact point ultimately controls the densification process. Creep experiments with instrumented indentation at the nano and the micro-scales confirmed this hypothesis. We found the same creep behavior regardless of the length scale probed, indicating that the creep behavior on the nanoscale determines the overall creep response of the sample.

The observation that nanoscale mechanisms control the cold sintering of vaterite powders through local dislocation motion or subcritical crack growth followed by neck formation is an important finding towards a better understanding of the water-assisted densification of this carbonate polymorph and the possible exploitation of this phenomenon in powders with other chemical compositions.

Chapter 6: Outlook

This thesis offers new insights to better understand the relatively new cold sintering process. However, there are still many open questions to be addressed, both for the room temperature densification of carbonates and for cold sintering in general.

First of all, the long-term behavior of cold-sintered nanovaterite compacts should be further investigated before this technology can be brought closer to an application. Since vaterite is a metastable phase, the kinetics of the phase transformation from vaterite to calcite in these dense structures need to be studied in more detail. The contact with water or even ambient humidity might trigger the transformation at the surface. Depending on the application in mind for this new technology, this should be investigated carefully. For example, for an application in the construction industry a fast phase transformation could be a major disadvantage. Moreover, the effect of this transformation on the mechanical performance of the final sample should be evaluated. These are critical pieces of information necessary to predict the long-term behavior of vaterite compacts in real structural applications.

Further investigations are also required to improve our understanding of the mechanisms underlying the room temperature cold sintering of nanovaterite. This thesis establishes the importance of the nanoparticles size and crystal structure along with their deformation response at the global and local scales. Other experimental tools could be explored to provide even clearer insights into the densification behavior of these powder compacts. As an example, the field would definitely benefit from more *in situ* mechanical testing in a scanning electron microscope (SEM) or even in a transmission electron microscope (TEM). New methods now allow water vapor or even liquid water to be present in the electron microscopy chamber. In a SEM, *in situ* compression tests on individual agglomerates would shed light on how their deformation proceeds under wet conditions. With such experiments, it should be possible to link the rearrangement of the nanoparticle network with the deformation of one agglomerate. A TEM equipped with an *in situ* mechanical tester would allow one to go one step further and even analyze how the individual nanoparticles behave under the compressive stress, finally revealing the mechanism controlling the densification process. Comparing the experimental results to simulations would further improve our understanding of this novel process. A rather straight forward approach would be to use finite element modelling to access local stress states and therefore better understand the local forces acting on the agglomerates, the primary nanoparticles and the necks between them during compaction. Molecular dynamics simulations would be of great benefit to understand the behavior of water in contact with the vaterite surface in more detail, but there are some limitations, which have to been kept in

mind. For example, the time scale of such simulations is not yet comparable to the timescale of typical experiments in the field. This means even simple processes, such as dissolution of a material are computationally expensive and not yet easily accessible.

Since one of the proposed mechanisms for cold sintering in nanovaterite is subcritical crack growth, there would be a need to investigate this phenomenon in more detail for this material as most data comes from experiment in calcite. It would thus be of great interest to measure the subcritical crack growth coefficient for vaterite and compare the results to the stress exponent coefficient reported in this thesis.

Additionally, there are many other open questions when it comes to cold sintering in general. One of the main challenges with this topic has been to establish an adequate definition of the cold sintering process. Defining scientifically-sound criteria for the cold sintering process would allow one to better distinguish and classify established and novel densification routes. One example here is cold sintering of sodium chloride (NaCl) or potassium bromide (KBr). Both of these materials are known to densify significantly under pressure, reaching relative densities up to 99% at room temperature. This method has already been used for decades for the preparation of samples for infrared spectroscopy. Therefore, the question can be raised if these processes involve cold sintering or not. To advance the field of cold sintering, it is very important to find common theories and mechanisms. It is also essential to start comparing different materials and find common properties that need to be fulfilled in order to ultimately promote cold sintering. This would allow one to more easily predict good processing parameters for a new material.

For me personally, it has been incredibly exciting to work on such a new method, where many questions are unanswered and interesting new ideas come up at a quick pace. With the current status, it is obvious that the literature is heavily dominated by the research group of Prof Dr. Clive Randall from The Pennsylvania State University in the United States. This team has published between 80 and 90% of all the publications available on cold sintering. On the basis of previous pioneer studies, the Randall group managed to ultimately define this new area of ceramic processing and they have done incredibly important novel work on many different materials. However, to further improve and expand this research field, more results from groups around the world should be gathered on this topic to both validate and update current theories on cold sintering.

Appendix A

Table A.1: Data for the graph in Figure 1.11.

Category	Material	liquid	Temperature (°C)	Pressure (MPa)	Solubility (g L^{-1})	Reference
Carbonate	$CaCO_3$	water	20	500	0.015	[1]
Chloride	NaCl	water	20	300	360	[2]
Molybdate	$K_2Mo_2O_7$	water	120	77	650	[3]
Molybdate	$K_2Mo_2O_7$	water	120	500	650	[3]
Molybdate	Li_2MoO_4	water	20	130	440	[4]
Molybdate	Li_2MoO_4	water	120	100	440	[5]
Oxide	ZnO	zinc acetate solution	85	50	0.0016	[6]
Oxide	ZnO	acetic acid	238	77	0.0016	[7]
Oxide	$Ca_3Co_4O_9$	water	135	350		[8]
Oxide	SiO_2 amorphous	water	300	190	0.001	[9]
Oxide	ZrO_2 (3Y TZP)	water	180	350		[10]

_____

Phosphate	KH_2PO_4	water	120	350	250	[11]
Phosphate	$Ca_5(PO_4)_3(OH)$	water	150	100		[12]
Phosphate	$Ca_5(PO_4)_3(OH)$	water	150	500	0.000031	[13]
Phosphate	CsH_2PO_4	water	140	300		[14]
Phosphate	$Li_{1.5}Al_{0.5}Ge_{1.5}(PO_4)_3$	water	120	400		[15]
Phosphate	$LiFePO_4$	2M LiOH	240	750		[16]
Titanate	$BaTiO_3$	$Ba(OH)_2$ / TiO_2 suspension	180	430		[17]
Titanate	$Pb(Zr,Ti)O_3$	$Pb(NO_3)_2$ solution	300	500		[18]
Titanate	$SrTiO_3$	1.5 M salt solution	180	750		[19]

References

[1]   F. Bouville, A.R. Studart, Geologically-inspired strong bulk ceramics made with water at room temperature, Nat. Commun. 8 (2017) 14655.

[2]   W.B. Hong, L. Li, M. Cao, X.M. Chen, Plastic deformation and effects of water in room-temperature cold sintering of NaCl microwave dielectric ceramics, J. Am. Ceram. Soc. 101(9) (2018) 4038-4043.

[3]   J. Guo, H. Guo, A.L. Baker, M.T. Lanagan, E.R. Kupp, G.L. Messing, C.A. Randall, Cold Sintering: A Paradigm Shift for Processing and Integration of Ceramics, Angew. Chem. Int. Ed. 55(38) (2016) 11457-11461.

_____

[4]   H. Kähäri, M. Teirikangas, J. Juuti, H. Jantunen, Dielectric Properties of Lithium Molybdate Ceramic Fabricated at Room Temperature, J. Am. Ceram. Soc. 97(11) (2014) 3378-3379.

[5]   A. Baker, H. Guo, J. Guo, C. Randall, Utilizing the Cold Sintering Process for Flexible–Printable Electroceramic Device Fabrication, J. Am. Ceram. Soc. 99(10) (2016) 3202-3204.

[6]   B. Dargatz, J. Gonzalez-Julian, O. Guillon, Improved compaction of ZnO nano-powder triggered by the presence of acetate and its effect on sintering, Sci. Technol. Adv. Mater. 16(2) (2015) 025008.

[7]   S. Funahashi, J. Guo, H. Guo, K. Wang, A.L. Baker, K. Shiratsuyu, C.A. Randall, Demonstration of the cold sintering process study for the densification and grain growth of ZnO ceramics, J. Am. Ceram. Soc. 100(2) (2017) 546-553.

[8]   S. Funahashi, H. Guo, J. Guo, A.L. Baker, K. Wang, K. Shiratsuyu, C.A. Randall, Cold sintering and co-firing of a multilayer device with thermoelectric materials, J. Am. Ceram. Soc. 100(8) (2017) 3488-3496.

[9]   A. Ndayishimiye, A. Largeteau, S. Mornet, M. Duttine, M.-A. Dourges, D. Denux, M. Verdier, M. Gouné, T. Hérisson de Beauvoir, C. Elissalde, G. Goglio, Hydrothermal Sintering for Densification of Silica. Evidence for the Role of Water, J. Eur. Ceram. Soc. 38(4) (2018) 1860-1870.

[10]   H. Guo, J. Guo, A. Baker, C.A. Randall, Cold sintering process for ZrO2-based ceramics: significantly enhanced densification evolution in yttria-doped ZrO2, J. Am. Ceram. Soc. 100(2) (2017) 491-495.

[11]   H. Guo, A. Baker, J. Guo, C.A. Randall, Cold Sintering Process: A Novel Technique for Low-Temperature Ceramic Processing of Ferroelectrics, J. Am. Ceram. Soc. 99(11) (2016) 3489-3507.

[12]   D. Grossin, S. Rollin-Martinet, C. Estournès, F. Rossignol, E. Champion, C. Combes, C. Rey, C. Geoffroy, C. Drouet, Biomimetic apatite sintered at very low temperature by spark plasma sintering: Physico-chemistry and microstructure aspects, Acta Biomater. 6(2) (2010) 577-585.

_____

[13] H.-Z. Shen, N. Guo, L. Zhao, P. Shen, Role of ion substitution and lattice water in the densification of cold-sintered hydroxyapatite, Scr. Mater. 177 (2020) 141-145.

[14] H. Nakaya, M. Iwasaki, T.H. de Beauvoir, C.A. Randall, Applying cold sintering process to a proton electrolyte material: CsH2PO4, J. Eur. Ceram. Soc. 39(2) (2019) 396-401.

[15] S.S. Berbano, J. Guo, H. Guo, M.T. Lanagan, C.A. Randall, Cold sintering process of Li1.5Al0.5Ge1.5(PO4)3 solid electrolyte, J. Am. Ceram. Soc. 100(5) (2017) 2123-2135.

[16] J.-H. Seo, J. Guo, H. Guo, K. Verlinde, D.S.B. Heidary, R. Rajagopalan, C.A. Randall, Cold sintering of a Li-ion cathode: LiFePO4-composite with high volumetric capacity, Ceram. Int. 43(17) (2017) 15370-15374.

[17] H. Guo, J. Guo, A. Baker, C.A. Randall, Hydrothermal-Assisted Cold Sintering Process: A New Guidance for Low-Temperature Ceramic Sintering, ACS Appl. Mater. Interfaces 8(32) (2016) 20909-20915.

[18] D. Wang, H. Guo, C.S. Morandi, C.A. Randall, S. Trolier-McKinstry, Cold sintering and electrical characterization of lead zirconate titanate piezoelectric ceramics, APL Materials 6(1) (2018) 016101.

[19] R. Boston, J. Guo, S. Funahashi, A.L. Baker, I.M. Reaney, C.A. Randall, Reactive intermediate phase cold sintering in strontium titanate, RSC Adv. 8(36) (2018) 20372-20378.

Appendix B

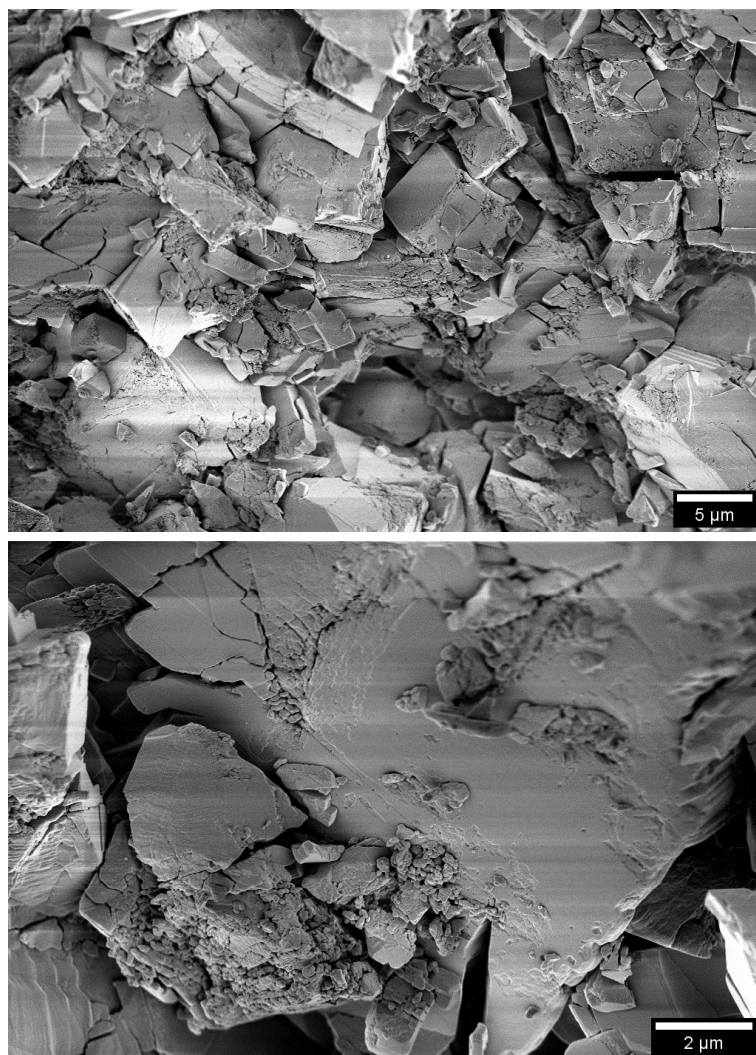*This Appendix has been published as supporting information in:*

Figure B.1: *Scanning Electron Microscopy (SEM) micrographs of calcite particles pressed with water at 500 MPa. The calcite particles used in this compaction experiment were used without prior milling. The pressing conditions and the liquid (L) to powder (P) weight ratio (L/P=0.3) were equivalent to those used for the vaterite particles described in the main text. The images suggest that the densification of calcite during compaction occurs via particle fracture, consistent with the literature data on geological calcite [1].*
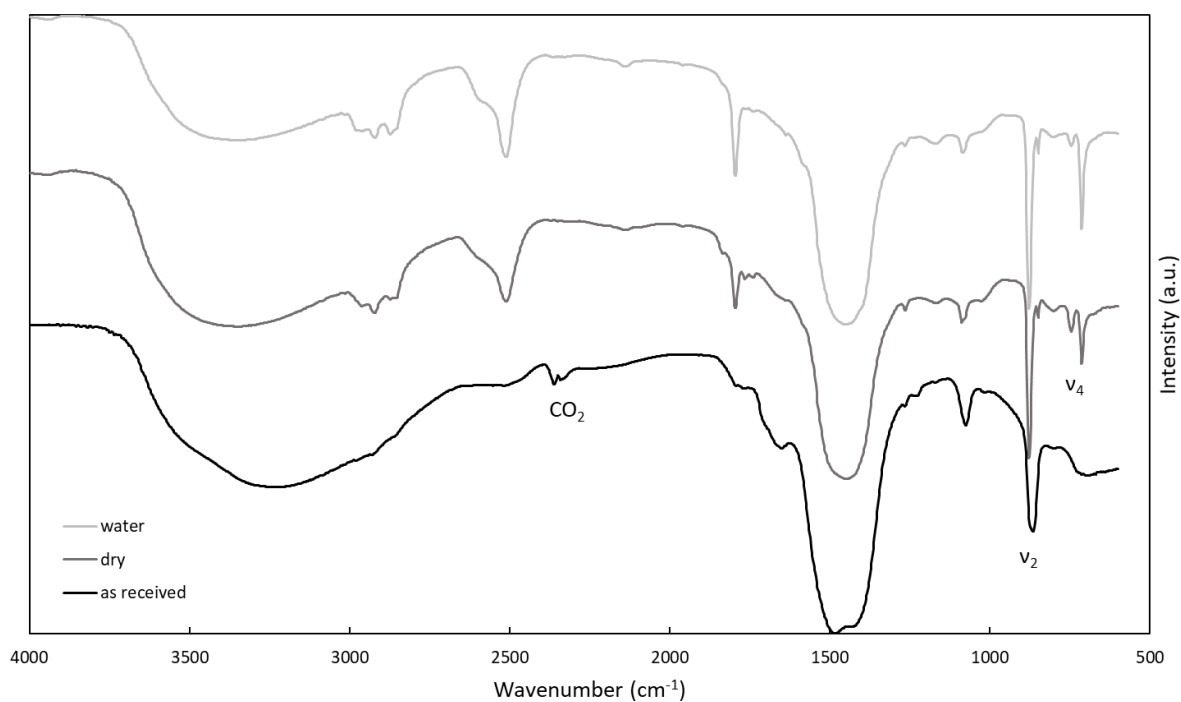
_____

Figure B.2: Fourier Transformed Infrared (FTIR) Spectroscopy of the amorphous calcium carbonate (ACC) particles.
All measurements were conducted using potassium bromide as background material. For sample preparation, the ACC particles were ground together with KBr and filled into the measuring cavity. The reported spectrum was acquired in reflection. The black curve was obtained from the as-synthesized powder. The dark grey curve corresponds to the samples pressed in air, whereas samples pressed with water at a L/P weight ratio of 2.5 are shown in light grey. The peak v_2 at wavenumber 863 cm^{-1} is shifted to 873 cm^{-1} upon transformation from ACC into calcite. Additionally peaks at 750 and 715 cm^{-1} appear which are characteristic for v_4 for vaterite and calcite respectively [2, 3].
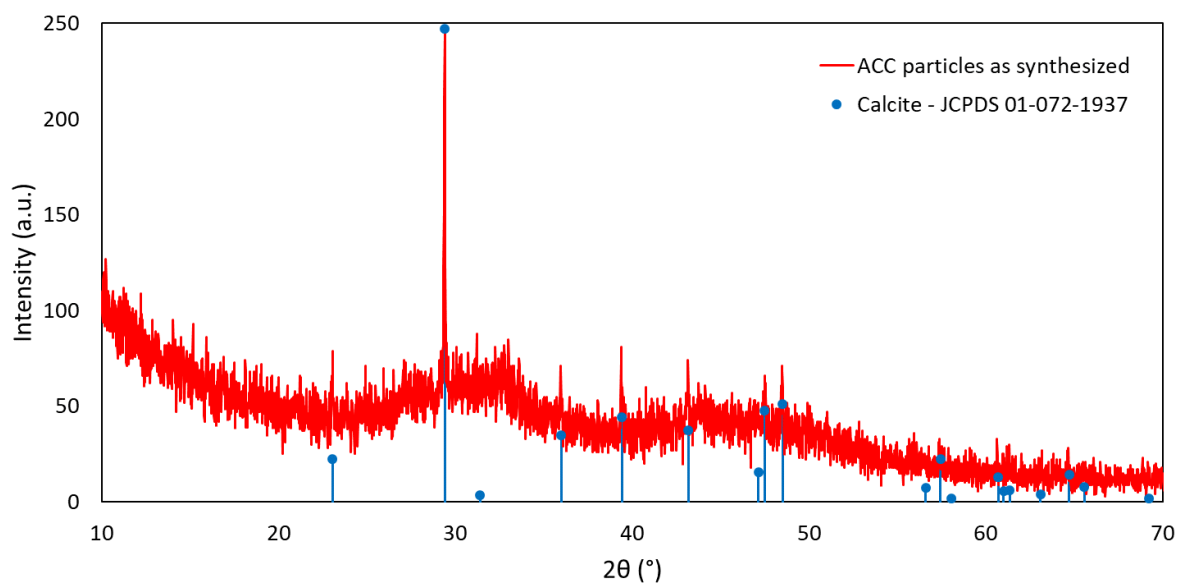
Figure B.3: X-ray diffraction pattern of the as-synthesized amorphous calcium carbonate particles (red). For comparison, the X-ray diffraction peaks for calcite are shown in blue.
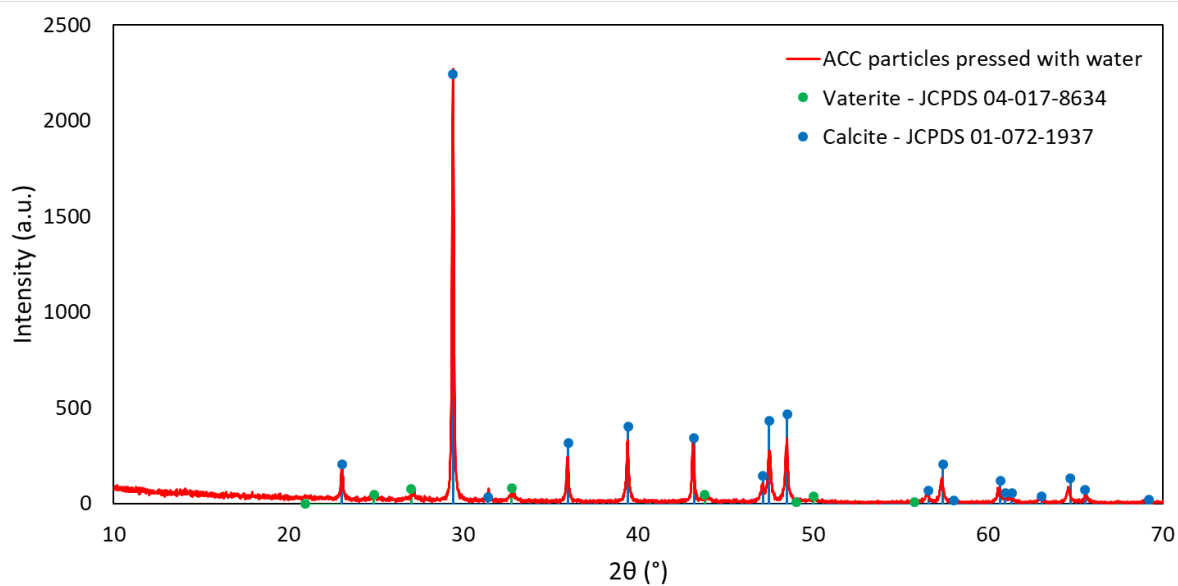

Figure B.4: X-ray diffraction pattern of the amorphous calcium carbonate particles after pressing with water (red). The blue and green spectra show reference data for calcite and vaterite, respectively.
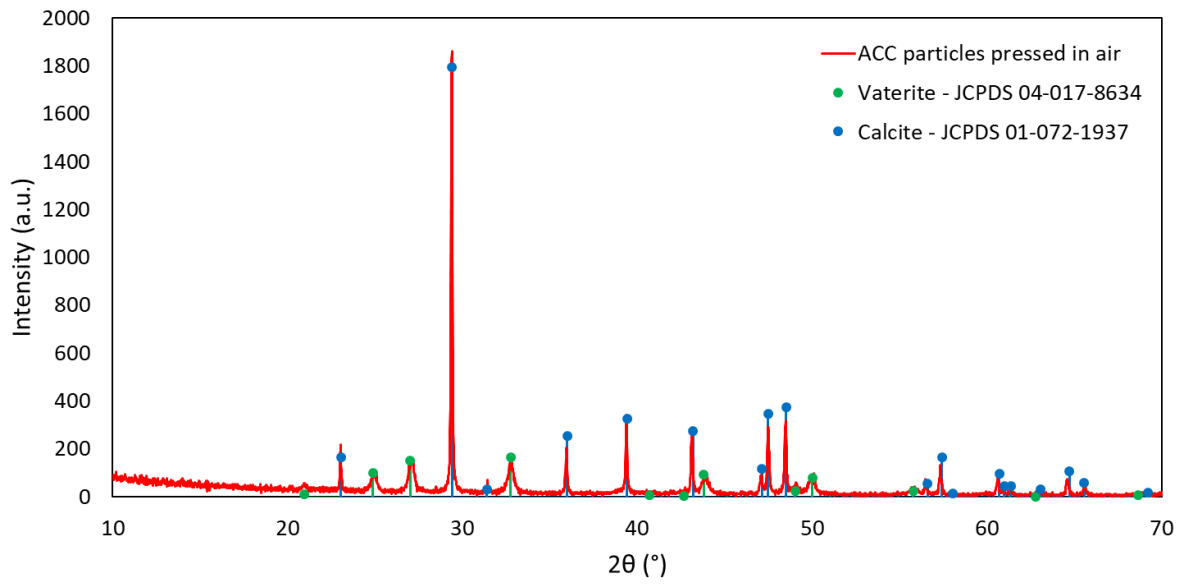
_____

Figure B.5: X-ray diffraction pattern of the amorphous calcium carbonate particles after pressing in air. *The blue and green spectra show reference data for calcite and vaterite, respectively.*
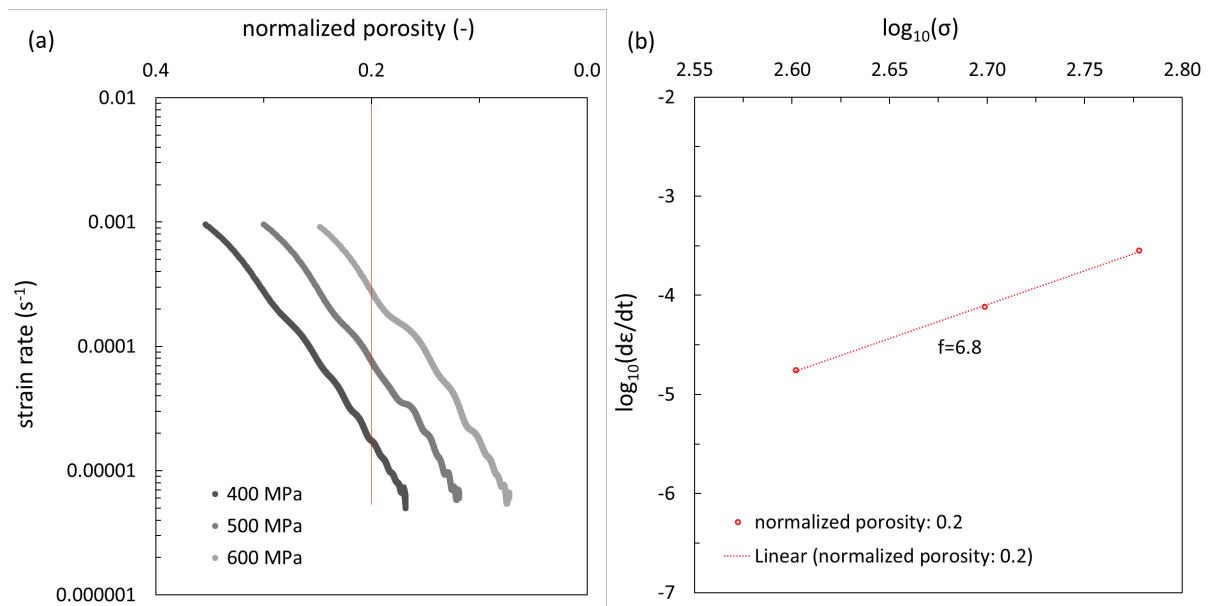

Figure B.6: Stress exponent calculations based on normalized porosity. *(a) Strain rate as a function of normalized porosity for compaction pressures of 400, 500 and 600 MPa. The normalized porosity is given by $\frac{\Phi}{\Phi_0}$, where φ is the actual porosity and φ0 is the porosity at the starting point of the compaction experiment (beginning of stage 1). (b) Calculation of the stress exponent, f, for a normalized porosity of 0.2.*

_____

References

[1]   A. Nicolas, J. Fortin, J.B. Regnet, B.A. Verberne, O. Plümper, A. Dimanov, C.J. Spiers, G. Y., Brittle and semibrittle creep of Tavel limestone deformed at room temperature, J. Geophys. Res. Solid Earth 122(6) (2017) 4436-4459.

[2]   M. Khouzani, D.M. Chevrier, P. Güttlein, K. Hauser, P. Zhang, N. Hedin, D. Gebauer, Disordered amorphous calcium carbonate from direct precipitation, CrystEngComm 17(26) (2015) 4842-4849.

[3]   M. Sato, S. Matsuda, Structure of vaterite and infrared spectra, Z. Kristallogr. 129(5-6) (1969) 405-410.

Appendix C

Figure C.1: SEM images displaying the primary particle sizes of ZnO agglomerates, nanovaterite agglomerates and hydroxyapatite platelets.
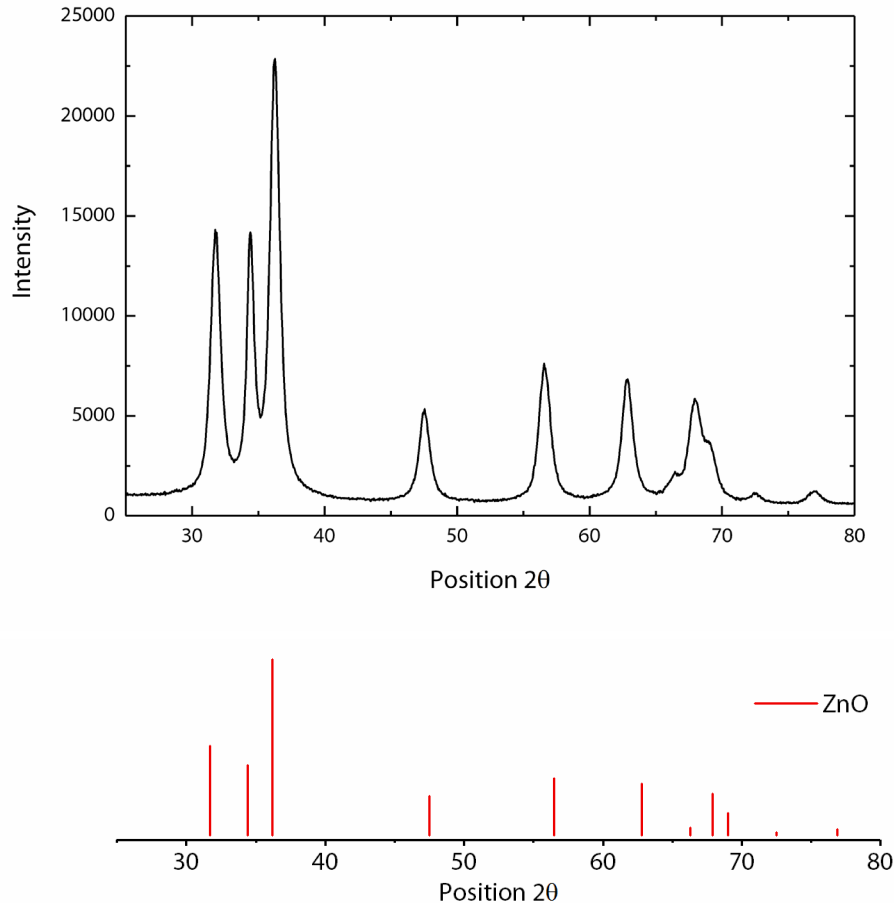
Figure C.2: X-Ray diffraction of the ZnO particles investigated in this study.
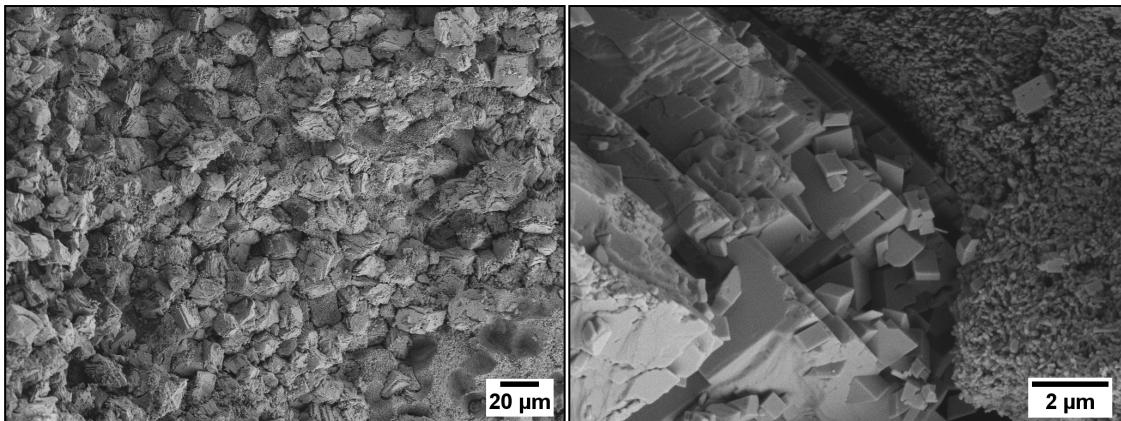

Figure C.3: SEM images of nanovaterite compacts pressed at 100 MPa and 90 °C. The cubic morphology observed in the micrographs is typical for the calcite phase of calcium carbonate.

Declaration

I would like to express my deepest gratitude to Prof. Dr. André R. Studart and Dr. Florian Bouville for structuring and organizing this thesis with me. Further, I am thankful to Julia Carpenter, Ahmad Rafsanjani and Fergal Coulter for proof-reading. There have been many more people involved in the experimental part of this thesis. Their contributions are listed in this chapter.

Chapter 2 and Appendix B

This project was a collaboration between the Complex Materials Group at ETH Zurich in Switzerland and the Group of Prof. Dr. Denis Gebauer affiliated at the University of Konstanz and Hannover. The project idea was originally developed by the author, Florian Bouville and André R. Studart. The amorphous calcium carbonate particles were prepared by Cristina Ruiz-Agudo and Jonathan Avaro, both working with Denis Gebauer. All other experiments were conducted by the author, results were discussed with Florian Bouville and André R. Studart. The author, Florian Bouville and André R. Studart prepared the figures and the manuscript. Before submission, it was reviewed by all the authors.

Chapter 3 and Appendix C

Fabio Bargardi prepared the ZnO particles and Vanessa Barreiro Lomba conducted the experiments under the instruction of the author. Vanessa Barreiro Lomba prepared the HA platelets used for the experiments and made all the densification tests as well as the experiments at elevated temperature under the instruction of the author. Samuel Montibeller performed the first experimental validation of the temperature set up. All results were discussed regularly with Florian Bouville and André R. Studart. The author, Florian Bouville and André R. Studart prepared the figures and wrote the manuscript.

Chapter 4

This project was a collaboration between the Complex Materials Group at ETH Zurich, Switzerland, the MATEIS laboratory at INSA in Lyon, France, the Swiss Light Source (SLS) at Paul Scherrer Institut (PSI) in Villigen, Switzerland and the CASC at Imperial College in London,

United Kingdom. The experiments were designed by the author and Florian Bouville. At the SLS, Anne Bonnin helped us with the operation of the beamline. The mechanical testing set up for the beam line was provided by the MATEIS laboratory. Jérome Adrien, Eric Maire, Marta Gallo and Florian Bouville supported the author with the measurements at PSI. The data were analyzed by the author with the help of Florian Bouville. Sam Humphry-Baker and Florian Bouville supported the author with the indentation measurements at the Imperial College London. The author, Florian Bouville and André R. Studart prepared the figures and wrote the manuscript. Before submission, it was reviewed by all the authors.

Curriculum Vitae

MATTHIAS HAUG

Albisstrasse 122
8038 Zürich
Switzerland

+41 76 454 37 41

matthiashaug@bluewin.ch

22. January 1990

Nationality: Swiss

Education

Since 01/2016	**Doctorate, Complex Materials, ETH Zurich, Switzerland**
	Title: *«Room-Temperature Sintering of Nanovaterite with Water»*
09/2013 – 10/2015	**MSc in Material Science, ETH Zurich, Switzerland**
04/2015 – 09/2015	**Master Thesis, SEAS, Harvard University, Cambridge MA, USA**
	Title: *«Binary Inverse Opal Films: Fabrication, Characterization and Possible Applications»*
09/2009 – 09/2012	**BSc in Material Science, ETH Zurich, Switzerland**
	Bachelor Thesis: *«Improving the Mechanical Properties of Poly(Ethylene Oxide) Films Reinforced with Alumina Micro-Platelets»*
08/2004 – 09/2008	**Matura, Kantonsschule Enge, Zurich, Switzerland**
	Focus: Economy and Law

_____

Publications and Patent

2020   **M. Haug**, F. Bouville, J. Adrien, A. Bonnin, E. Maire, A.R. Studart, Multiscale-deformation processes during cold sintering of nanovaterite compacts, accepted in Acta Materialia (2020).

2020   **M. Haug**, F. Bouville, C. Ruiz-Agudo, J. Avaro, D. Gebauer, A.R. Studart, Cold densification and sintering of nanovaterite by pressing with water, J. Eur. Ceram. Soc. 40(3) (2020) 893-900.

2019   F. Bouville, **M. Haug**, A.R. Studart, High performance ceramics from cold sintered nanoscale powders, US 2019 / 0248707 A1

2018   P.A. Rühs, F. Storz, Y.A. López Gómez, **M. Haug**, P. Fischer, 3D bacterial cellulose biofilms formed by foam templating, npj Biofilms and Microbiomes 4(1) (2018) 21.

Conferences and Summer Schools

12/2019   Oral presentation at the MRS Fall Meeting & Exhibit, Boston, United States of America

10/2019   Poster presentation at the conference on Bioinspired Materials, Monte Verita, Switzerland

07/2019   Oral presentation at the MaP Graduate Symposium 2019, Zurich, Switzerland

01/2019   Oral presentation at the 43th International Conference and Exposition on Advanced Ceramics and Composites, Daytona Beach, United States of America

04/2018   Poster presentation at the 9th International Workshop on Interfaces, Santiago de Compostela, Spain

09/2017   Attendance at the Transdisciplinary Seminar "Cortona Week", Cortona, Italy

09/2017   Attendance at the 8th CASC Summer School on Ceramics, Imperial College London, United Kingdom

_____

07/2017	Attendance at the MaP Graduate Symposium 2017, Zurich, Switzerland
	Winner of the Image Award
06/2017	Attendance at the CCMX Advanced Course on Field and Pressure-Assisted Sintering, EPF Lausanne, Switzerland
06/2016	Co-Organizer of the MaP Graduate Symposium 2016, Zurich, Switzerland

Teaching Experience

| 2016-2018 | Praktium III for Bachelor Students
Versuch C1: Umesterung und Hydrolyse (PET Versuch)
Versuch C2: Herstellung von Polyacrylat durch radikalische Polymersation (PMMA Versuch) |
|---|---|
| 2017 | Forschungslabor for Bachelor Students |

Student Supervision

| 02/2019 – 09/2019 | Vanessa Barreiro Lomba – Master Thesis
Title: "Hydroxyapatite – Polymer Composite for Bone Replacement Applications" |
|---|---|
| 11/2018 – 01/2019 | Vanessa Barreiro Lomba – Master Project
Title: "Cold Sintering of Calcium Phosphate" |
| 03/2018 – 09/2018 | Samuel Montibeller – Bachelor Thesis
Title: "Cold Sintering behavior of Hydroxyapatite and Following Applications" |
| 12/2017 – 01/2018 | Sophia Ganzeboom – Master Project
Title: "Towards a Bone Substitute" |

Working Experience

05/2013 – 08/2013   **Internship, DOW Europe GmbH, Horgen, Switzerland**

- Set up new equipment for testing thermal conductivity
- Assessed the optimal measuring parameters

01/2013 – 03/2013   **Internship, Carbo-Link AG, Fehraltorf, Switzerland**

- Established guidelines for the use of adhesives for carbon-fiber reinforced polymers
- Evaluated the best adhesive by performing tests in the laboratory

Extracurricular Activities

Since 2014   **Project manager, Focus Vennes – Das Projekt Neubau Pfadiheim**
Budget: 1.7 million CHF, 13 people

- Building a new house for my boy scout group
- Leading the entire project and the team
- Contacting and negotiating with the government administration
- Responsible for fundraising

2007 – 2017   **Tennis Coach for children, Tennis Club Adliswil, Switzerland**

- Organized and planed regular training units
- Completed advanced training by the government (Jugend+Sport)

2004 – 2013   **Head Scout for boy scouts, Pfadi Vennes Zurich, Switzerland**

- Lead the association
- Sharped skills for of team management and leadership in advanced training by J+S (Jugend+Sport)

10/2012 – 12/2012   Language studies, San Francisco CA, USA

Certificate of Advanced English

Languages

German   Native language

English   Business fluent

French   Basic knowledge

Italian   Basic knowledge

Interests

Tennis, cooking, hiking, photography, golf